Professorship of Healthcare and Rehabilitation Robotics
Chair of Applied Mechanics
TUM School of Engineering and Design

TECHNICAL UNIVERSITY OF MUNICH

in collaboration with

DEUTSCHES ZENTRUM FÜR LUFT- UND RAUMFAHRT (DLR)

Master Thesis in Aerospace Engineering

Design and Validation of a 3D Structurally-Elastic Bioinspired Humanoid Robot Foot for Elastic and Rigid Contact Behaviors

Fabien Naiser Rahmad

Professorship of Healthcare and Rehabilitation Robotics
Chair of Applied Mechanics
TUM School of Engineering and Design

TECHNICAL UNIVERSITY OF MUNICH

in collaboration with

DEUTSCHES ZENTRUM FÜR LUFT- UND RAUMFAHRT (DLR)

Master Thesis in Aerospace Engineering

Design and Validation of a 3D Structurally-Elastic Bioinspired Humanoid Robot Foot for Elastic and Rigid Contact Behaviors

Author:	Fabien Naiser Rahmad
1. Examiner:	*Prof. Dr. Daniel J. Rixen*
2. Examiner:	*Prof. Dr. Cristina Piazza*
Supervisor:	Konrad Fründ, M.Sc.
Submission Date:	01.09.2025

Acknowledgments

I acknowledge the use of AI tools, including Perplexity, to refine the style and clarity of writing in this thesis. The substantive content, analysis, and conclusions remain my own work.

I confirm that this master thesis is my own work and I have documented all sources and material used.

Munich, 01.09.2025 Fabien Naiser Rahmad

Abstract

Most current humanoid robot foot designs are limited to the incorporation of 2D properties and do not replicate the full 3D biomechanics of the human foot, especially the crucial differences in medial and lateral arch stiffness. As a result, existing designs are not capable of storing different amounts of energy according to different center of pressure trajectories over the foot the way a human foot does. Furthermore, they do not utilize the energy naturally stored in the human foot-ankle complex during the mid-stance phase. This results in suboptimal energy storage in favor of stability. This thesis addresses this gap by designing and validating a 3D structurally-elastic bioinspired humanoid robot foot with differentiated stiffness in the medial, center, and lateral regions. Carbon fiber beams of varying bending stiffness are used to enable both elastic and rigid contact depending on the center of pressure trajectory during mid-stance. Validation through finite element simulations, material testing, and dynamic experiments demonstrates significant variation (p=0.01) of stiffness and strain energy, consistent with human biomechanics. Dynamic mid-stance testing shows a strong correlation (ρ=0.84, p=0) between the center of pressure trajectory and longitudinal ground reaction force slope, confirming the achievement of elastic and rigid contact behaviors. The design better reproduces mid-stance energy storage mechanisms compared to a state-of-the-art energy-storage-and-return prosthetic foot, contributing a novel approach to energy-efficient humanoid robot locomotion.

Contents

List of Figures

List of Tables

1. Introduction

The locomotive performance of a humanoid robot is greatly influenced by the design of its lower limbs [1]. This particularly applies to the foot, which is the end-effector of the locomotive kinematic chain. The stability and efficiency of bipedal locomotion depend on the ability of the foot to effectively interact with the ground and support the complex dynamics of gait. Consequently, the development of an effective robot foot is not only a mechanical challenge, but also a central determinant of a humanoid robot's performance.

Since humanoid robots are fundamentally inspired by human physiology, a comprehensive understanding of human biomechanics is a necessary foundation for design. The human foot provides a natural point of reference as a highly evolved and multifunctional structure. Its anatomy and mechanics support not only weight bearing and balance, but also energy-efficient locomotion [2]. This is enabled by mechanisms such as the Windlass effect and the center of pressure trajectory in mid-stance. These principles represent more than biological phenomena - they constitute design strategies that have been refined over millions of years of evolution and can offer vital insights for engineering solutions.

However, despite extensive research into the foot biomechanics, these energy-storing mechanisms have seen limited implementation in humanoid robot foot designs [3][4]. Current approaches tend to prioritize stability and predictability over energy efficiency. This results in designs with rigid structures and flat contact surfaces that simplify balance control. As a result, the Windlass effect and energy storage mechanisms during mid-stance remain largely absent. While this ensures reliable locomotion, it also constrains the potential for a more energy-efficient gait. This highlights a clear need for further investigation into integrating bioinspired principles into humanoid robot feet.

Against this backdrop, this thesis focuses on the design and validation of a 3D structurally-elastic bioinspired humanoid robot foot that can achieve elastic and rigid contact behavior. By leveraging three-dimensional structural elasticity, the foot aims to reproduce key biomechanical features during mid-stance to allow both energy storage and stability through different center of pressure trajectories. Through systematic design iterations and experimental validation, the thesis aims to fill a critical gap in the field of humanoid robots, advancing beyond conventional designs that prioritize stability at the expense of energy efficiency.

2. Theoretical Background

2.1. Anatomy of the Foot

The human foot is a complex structure with several key components (Figure 2.1). Among the most important are the arches. These include one transverse arch and two longitudinal arches. The transverse arch runs across the foot between the first and fifth metatarsals. It stabilizes the foot on uneven ground. The longitudinal arches are divided into medial and lateral. The medial longitudinal arch lies along the inner foot, closer to the body's midline. It is the main structure for absorbing and releasing energy [5]. This arch is formed by the calcaneus, talus, navicular, and the first three metatarsals [6]. The lateral longitudinal arch runs along the outer foot. Its role is to provide stability and support [7]. It is formed by the calcaneus, cuboid, and the fourth and fifth metatarsals [6]. Together, the arches ensure both flexibility and stability of the foot, and they are central to its ability to store and release energy [2].

Muscles and tendons reinforce the function of the longitudinal arches. The plantar fascia is a strong connective band spanning the medial arch [8]. It stretches and recoils during movement. Intrinsic muscles in the sole, such as the flexor digitorum brevis (FDB) and abductor hallucis, strengthen the arch and add flexibility [9]. The Achilles tendon connects the calf muscles to the heel [10]. It stores energy when the foot presses down and releases it during push-off. These tissues act together to make walking more efficient [2].

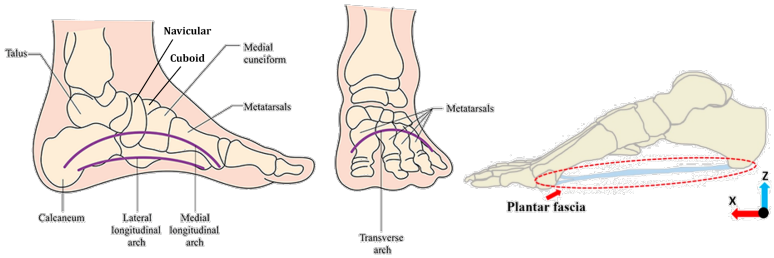

Figure 2.1.: Anatomy of the human foot [11][12].

2.2. Energy Storage in the Foot

Studies show that the foot's arches and plantar fascia are central to its energy storage. They work like springs, passively storing and returning energy as the foot compresses and recoils [7]. Ker et al. estimated that the foot–ankle complex can store up to 52% of the mechanical work during running, with 17% stored in the arch alone [8]. More recent research highlights the role of the plantar fascia and the flexor digitorum brevis (FDB) muscle in enhancing energy storage during compression [9] (see Figure 2.2). These findings validate the spring-like behavior of arch-related structures and their contribution to efficient energy use.

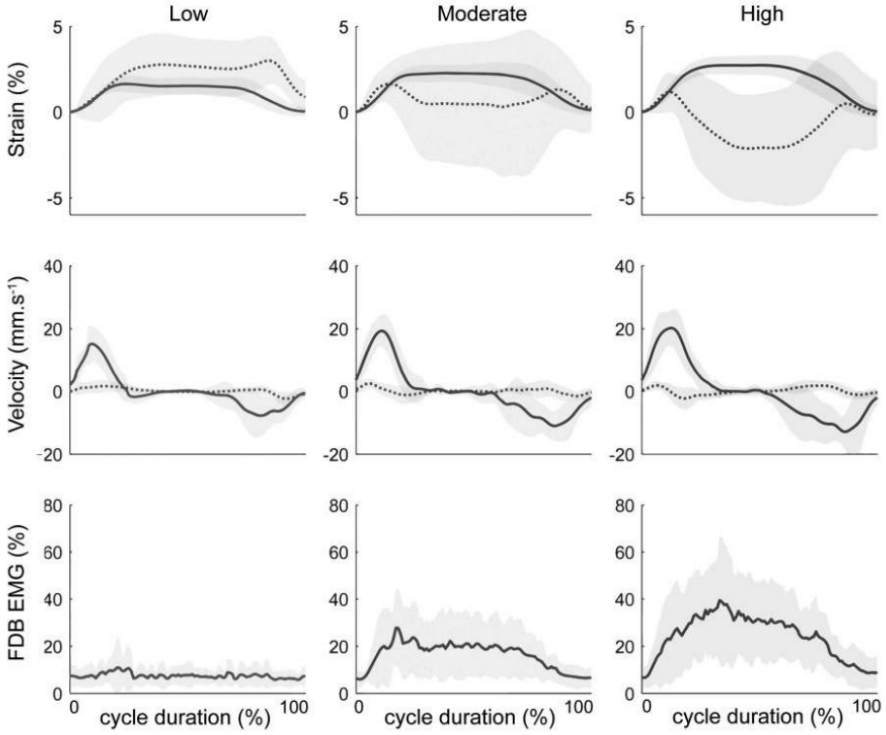

Figure 2.2.: Mean ensemble data of FDB muscle-tendon unit (lines) and fascicle (dots) for strain (top), velocity (middle), and muscle activation (bottom) during foot compression cycles at low(left), medium (middle), and high (right) loading conditions [9]. The findings provide further validation of the results from [8] regarding energy storage in the foot, particularly in the FDB muscle-tendon unit.

2.3. Gait Cycle and the Mid-Stance Phase

The gait cycle of a foot consists of two phases: stance and swing [13]. The stance phase is the phase during which some part of the foot is in contact with the ground. It occupies 60% of the total gait cycle. It is divided into four sub-phases [14] as shown in Figure 2.3:

1. Initial contact (heel strike)
2. Loading response (foot flat)
3. Mid-stance
4. Terminal stance (push-off)

During mid-stance, the shank transfers upper-body forces to the foot [15] as it bears full body weight and reaches maximum compression [16]. The arch flattens slightly, stretching the plantar fascia, while the Achilles tendon and calf muscles absorb energy as they control forward leg rotation. These actions create tension in both the plantar fascia and Achilles tendon, storing elastic energy like a spring [17]. This stored energy is released during push-off, assisting forward propulsion [5].

In this phase, the shank supports upright posture and stabilizes the leg while the foot contacts the ground.

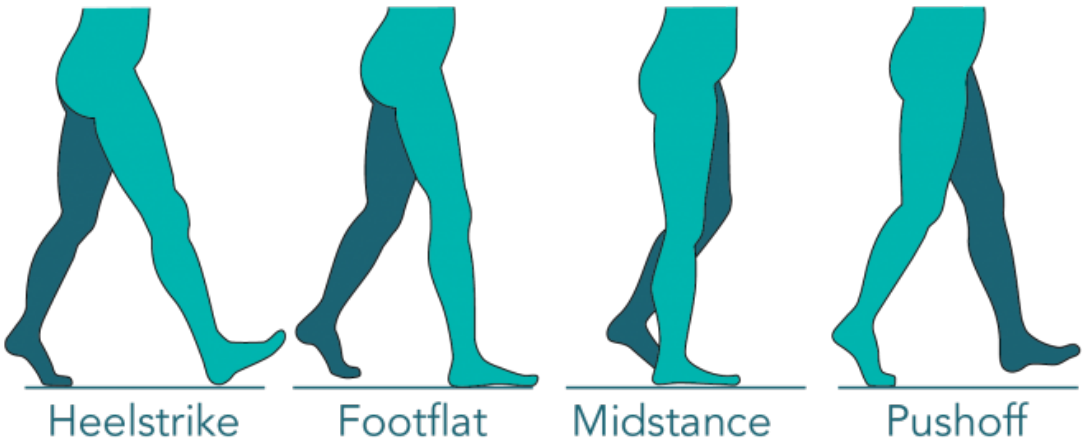

Figure 2.3.: The four stance phases of the gait cycle [14].

2.4. Center of Pressure Trajectory

The center of pressure trajectory is the path of the pressure point beneath the foot during stance [18]. It shows how body weight shifts from heel strike, through mid-stance, to push-off, and serves as a measure of stability and gait efficiency. During loading response, the center of pressure moves forward by about 100–120 mm until it reaches the metatarsal heads [19].

Studies show that this trajectory changes with locomotion speed [20] (see Figure 2.4). The path also shifts slightly toward the medial side of the foot and aligns with its longitudinal axis [21][22]. This medial shift reflects the foot's adaptation to higher propulsive demands during toe-off in running, which occurs at the cost of reduced stability [23].

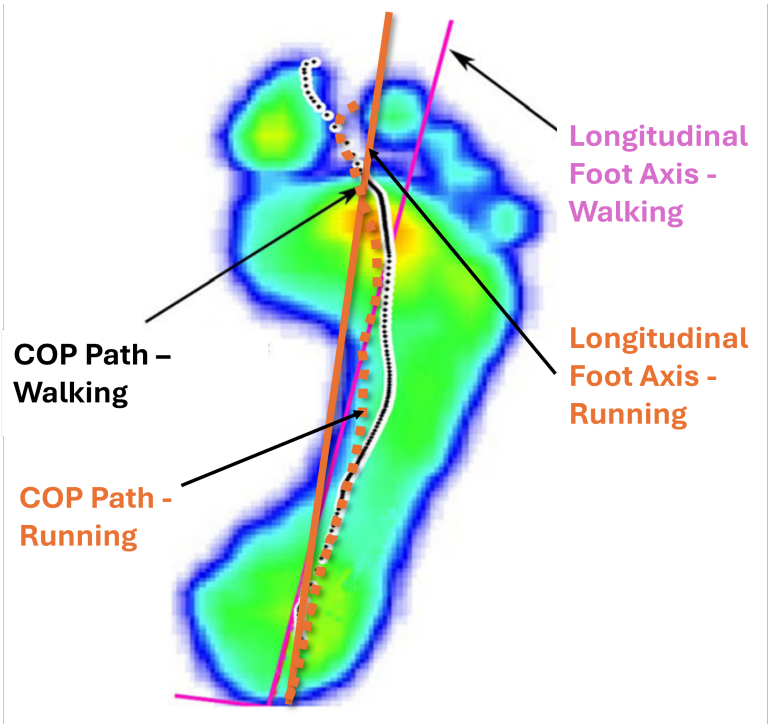

Figure 2.4.: Center of pressure trajectories and longitudinal foot axes for walking and running. Overlayed sketches based on findings from [21] and [22].

2.5. Oblique Axis in the Subtalar Joint

The subtalar joint, or lower ankle joint, functions as a mitered hinge rotating around an oblique axis [24] (see Figure 2.5). This axis couples movements across the frontal, transverse, and sagittal planes as body weight shifts forward. Through this coupling, the subtalar joint influences the center of pressure trajectory by guiding it along the longitudinal arches.

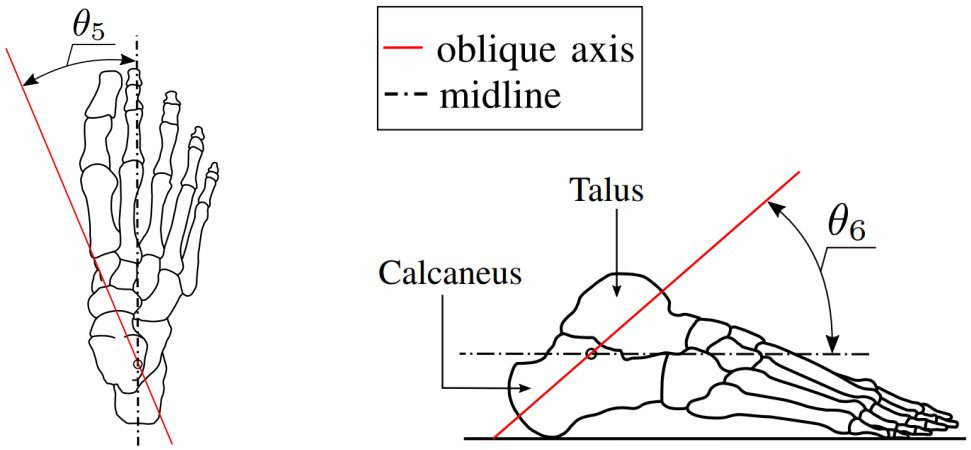

(a) Transversal plane.

(b) Sagittal plane.

Figure 2.5.: Oblique subtalar axis in the different planes. $\theta_5 = 16°$ and $\theta_6 = 42°$ are the inclination angles with respect to the foot longitudinal line in the transversal and sagittal planes respectively [24].

2.6. Windlass Mechanism

The Windlass mechanism is a key process that enables the foot to store and release energy during locomotion. It describes how the foot absorbs impact energy and later releases it to propel the body forward (Figure 2.6). When the toes dorsiflex, the plantar fascia tightens [25], winding around the metatarsal heads and increasing the medial arch height [26]. During toe push-off, the plantar fascia recoils and releases this stored energy in a spring-like response. The Windlass mechanism is essential for preserving arch stability and supporting efficient propulsion [27].

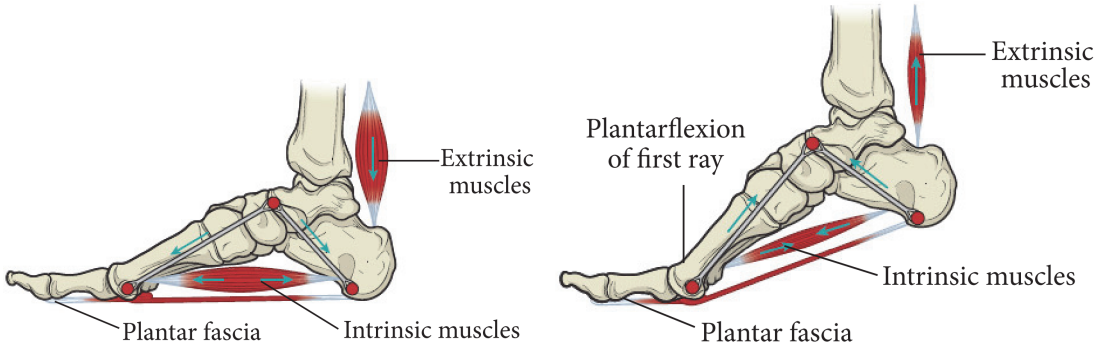

(a) Toe neutral. (b) Toe extended.

Figure 2.6.: The mobilization of the Windlass mechanism due to toe extension [6].

2.7. Ankle Catapult

The ankle catapult is a biomechanical mechanism in which the Achilles tendon and surrounding structures rapidly release stored energy during push-off [28] (see Figure 2.7). The tendon stores this energy as it is tensioned by forward leg rotation in mid-stance [17]. Its sudden release produces a powerful and efficient forward thrust, similar to a catapult [29].

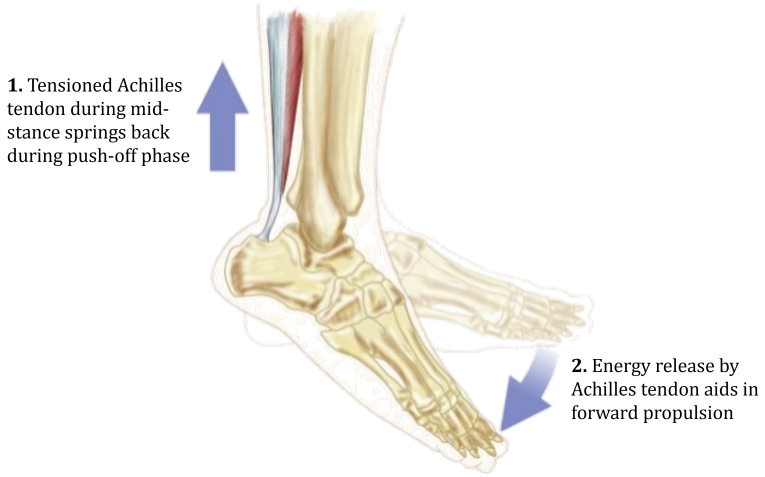

Figure 2.7.: Ankle catapult mechanism [30].

3. State of the Art

3.1. Humanoid Robot Foot Designs

3.1.1. TORO

TORO [31] is a torque-controlled humanoid robot developed by the German Aerospace Center (DLR). Its aluminium feet are flat and rigid with no elastic components. This design ensures stable and precise ground contact, simplifying balance control. The absence of elasticity prevents the bioinspired mechanisms of energy storage and return found in the human foot.

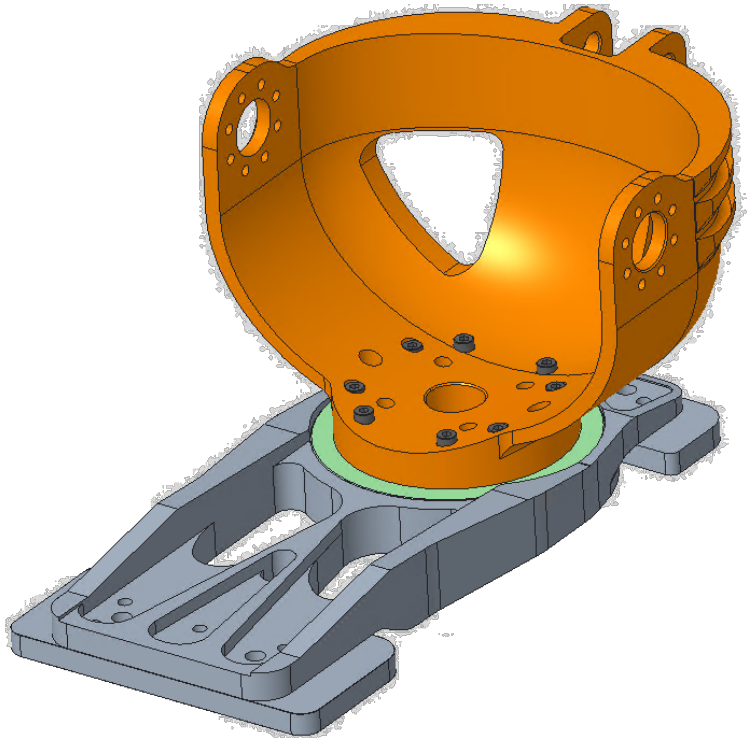

Figure 3.1.: Flat aluminium foot design of TORO.

3.1.2. Honda ASIMO

Honda ASIMO (Figure 3.2) is among the first humanoid robots that incorporates elastic and damping elements in its foot design. Its feet include rubber soles and rubber bushes mounted within guides [32]. These components deform elastically under vertical loads, allowing the foot to absorb impact forces during walking and running. Additionally, they serve as mechanical low-pass filters to reduce vibrations in the leg compliance control system.

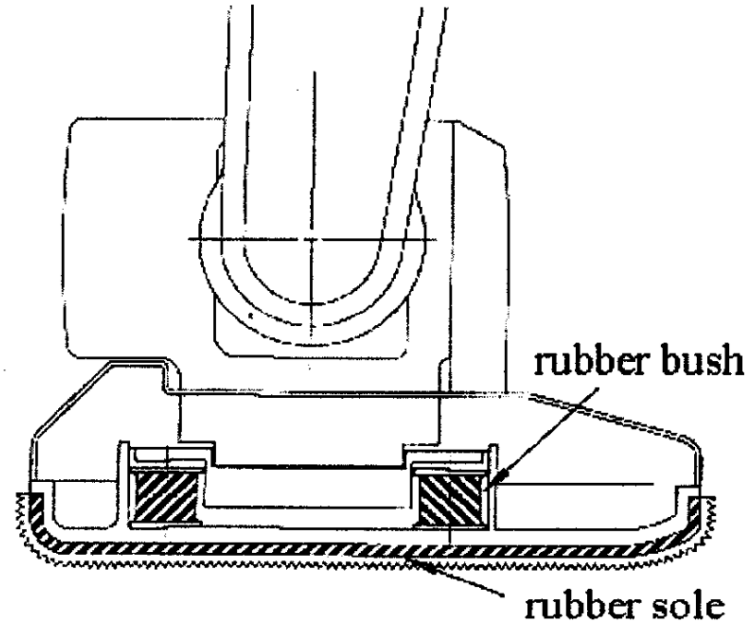

Figure 3.2.: Damping elements in the foot design of Honda ASIMO [32].

3.1.3. Lola

Lola is a humanoid robot developed by the Technical University of Munich (TUM). It features a foot design that incorporates elastic and damping elements for shock attenuation as well as forward propulsion [33]. This is shown in Figure 3.3. The passive compliant components on the foot-ground interface absorbs impact forces during ground contact. The active toe joint helps propel the foot forward during the push-off phase.

Lola [33] is a humanoid robot developed by the Technical University of Munich (TUM). Its foot design combines elastic and damping elements for shock absorption

and forward propulsion (Figure 3.3). Passive compliant components at the foot-ground interface absorb impact forces during contact. An active toe joint aids in propelling the foot forward during push-off.

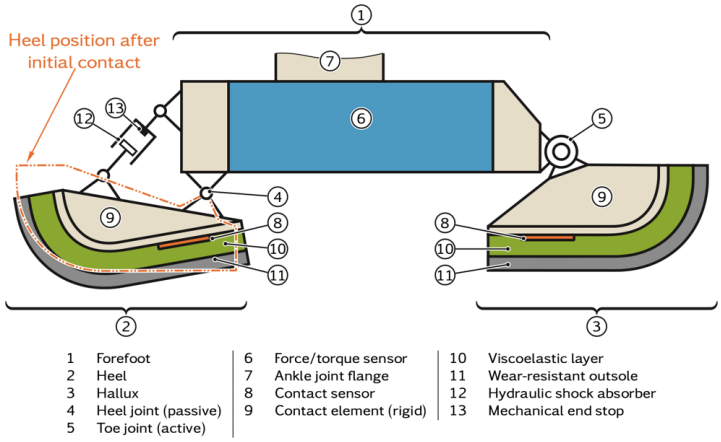

Figure 3.3.: Foot design of Lola. It features viscoelastic layers and hydraulic shock absorbers for impact force attenuation. It also features an active toe joint to aid forward propulsion [33].

3.2. Prosthetic Foot Designs

3.2.1. Adaptive Foot

Adaptive foot designs help restore mobility to people with lower-limb amputations by replicating the human foot's ability to adapt to uneven surfaces [3]. They use biomechanical features to transfer this adaptability to users and are classified into passive and active types.

Passive feet rely on the foot's structural properties to adjust to terrain [3]. For example, SoftFoot [34] increases stiffness under compression through elastic bands connecting its parts (see Figure 3.4a). The HEELfoot [35] uses steel springs under the sole to mimic the plantar fascia and allow plantar flexion (see Figure 3.4b). The midtarsal joint locking foot [36] features a clutch that keeps the foot elastic in early stance but locks it rigid after sufficient compression (see Figure 3.4c).

Active foot designs use actuators to adjust foot properties actively for better terrain adaptation [3]. They can mimic human leg motions more closely than passive designs. The PANTOE 1 [37] foot uses series-elastic actuators to control toe and ankle joint

stiffness and propulsion, providing enhanced stability and energy during walking (see Figure 3.4d).

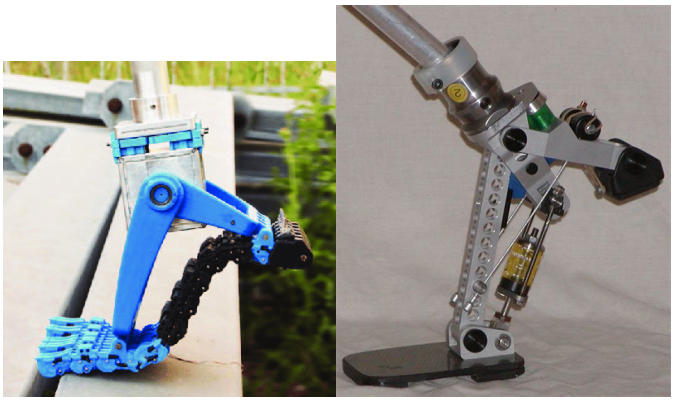

(a) SoftFoot [34]. (b) HEELfoot [35].

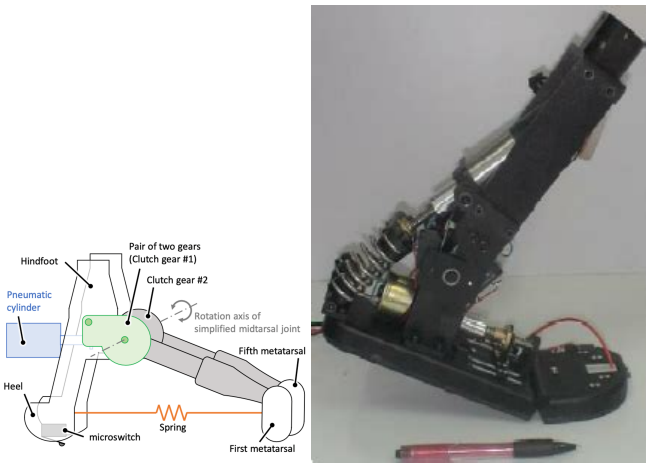

(c) MTJ locking foot [36]. (d) PANTOE 1 [37].

Figure 3.4.: Adaptive foot designs.

3.2.2. Energy-Storage-and-Return (ESR) Foot

Energy-storage-and-return (ESR) feet store energy using a spring loaded by body weight [4]. The Ottobock 1C63 Triton Low Profile [38] is an advanced ESR prosthesis designed for fast walking (see Figure 3.5). Its carbon fiber leaf spring stores elastic energy when loaded, supporting agile and high-impact movements. The forefoot features a curved sole that enables dynamic rollover during push-off.

Figure 3.5.: Ottobock 163C Triton Low Profile ESR prosthetic foot [38].

3.3. Potential Contribution to the Field

Current state-of-the-art foot designs rarely implement 3D structural properties that utilize energy stored during mid-stance. Humanoid robot feet prioritize stability and control predictability, using elastic and damping elements mainly for impact absorption and active propulsion. Passive designs adjust stiffness to adapt to uneven terrain, while active designs rely on external actuators to control properties. Energy-storage-and-return (ESR) prosthetic feet use only 2D structural features.

These designs do not fully capture the human foot's biomechanics, especially the stiffness differences between the medial and lateral arches. The lack of 3D elastic behavior means they do not harness the foot's stored energy effectively [8][9]. This gap opens opportunities for bioinspired foot designs featuring 3D structural elasticity that enable both elastic and rigid contact behaviors.

Recognizing this gap, the research aims to contribute significantly to humanoid robot foot design with the statement: "Design and Validation of a 3D Structurally-Elastic Bioinspired Humanoid Robot Foot for Elastic and Rigid Contact Behaviors".

4. Design and Validation Approach

4.1. V-Model

The V-model guides the design and validation phases of this thesis (see Figure 4.1). It defines each design stage alongside its corresponding validation method. This approach ensures every design iteration is assessed against specific validation criteria, steering progress toward the final objective. The tools used for design and validation in this thesis are detailed in the following sections.

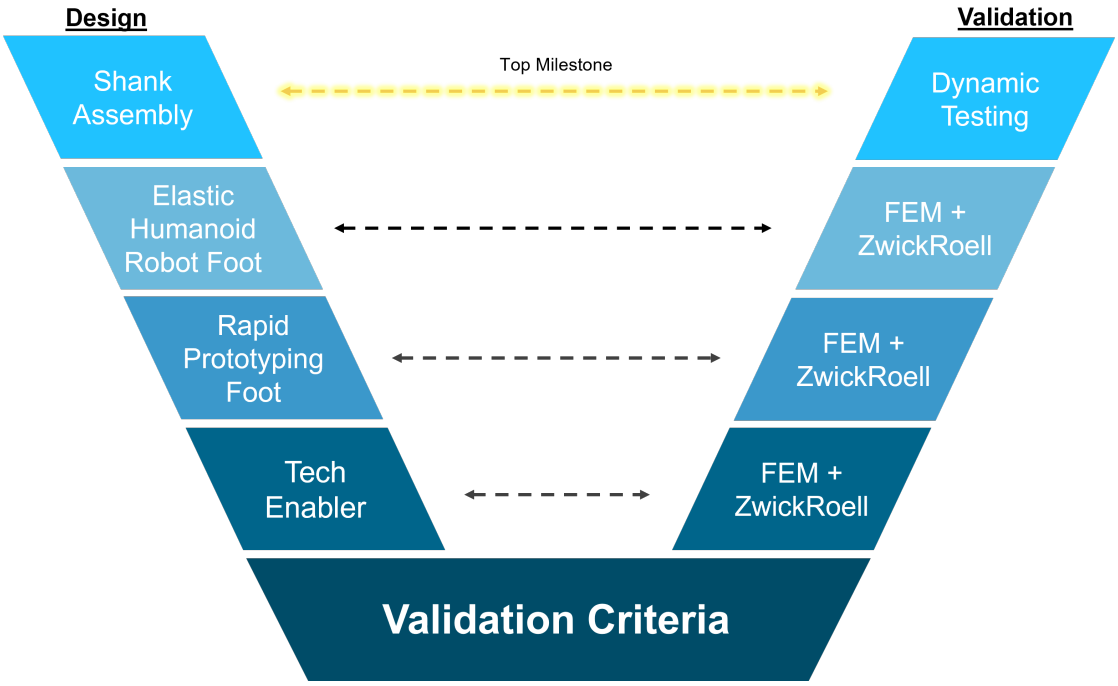

Figure 4.1.: V-Model summarizing the design and validation approach.

4.2. Validation Criteria

Each design phase follows specific criteria derived from requirements that the design must meet. This ensures every milestone contributes towards the thesis goal. Validation methods associated with each phase evaluate relevant parameters. A summary of these methods and their criteria is provided in Table 4.1.

Validation Method	**FEM**	**ZwickRoell Machine**	**Dynamic Testing**
Vertical Displacement	**X**	**X**	
Rebound Direction	**X**		
Strain Energy	**X**		
Stiffness		**X**	
Ground Reaction Force Slope			**X**

Table 4.1.: Validation methods and their corresponding validation criteria.

4.3. Computer-Aided Design

Computer-Aided Design (CAD) supports the development of concepts, prototypes, and the final product throughout this research. Design iterations incorporate progressive improvements aligned with requirements. CAD software and with suitable design tools are utilized.

4.4. Finite Element Method

Finite Element Method (FEM) analyzes and predicts design behavior under various conditions. It validates CAD models virtually by simulating expected loads and boundary conditions without physical prototypes. This virtual validation supports iterative design, improving workflow efficiency.

4.5. ZwickRoell Material Testing

The ZwickRoell universal testing machine is used to evaluate the mechanical properties of manufactured parts. It validates the results predicted by FEM simulations. Compression and bending tests reproduce the load conditions experienced by the designed components.

4.6. Dynamic Testing

Dynamic testing validates the elastic foot design by simulating the mid-stance phase of gait. It applies varying center of pressure trajectories to the foot, aiming to produce different ground reaction forces depending on the applied trajectory. This approach reflects the foot's varying energy storage capacity across softer and stiffer regions, demonstrating both elastic and rigid contact behaviors.

5. Tech Enabler

5.1. Motivation

The first design phase, the tech enabler, tests the research foundation by defining a foot design that integrates 3D elastic properties for both elastic and rigid contact. Due to limited studies on human foot arch geometry and its role in stiffness and energy storage, this phase explores basic foot designs and their key parameters. This approach fills a research gap and guides the development of robotic feet that incorporates human biomechanical properties.

5.2. Straight Beam

The thesis studies the bending of a straight rectangular beam to analyze elastic properties. This is a valid starting because analytical solutions exist for various load cases, deflection curves, and bending stiffness. The bending stiffness K for a cantilever beam is given by Equation 5.1 [39]. F is the vertical force applied at the free end, δ_{max} is the maximum allowable vertical displacement, E is Young's modulus, I is the second moment of area, and L is the beam length.

$$K = \frac{F}{\delta_{max}} = \frac{3EI}{L^3} \tag{5.1}$$

For rectangular cross-sections, the second moment of area I is shown in Equation 5.2. b and h are the width and height of the cross-section respectively.

$$I = \frac{bh^3}{12} \tag{5.2}$$

Assuming fixed material, foot length, perpendicular force, beam width, and maximum beam deflection, the equation can dimension the beam thickness for desired bending stiffness. However, the straight beam does not accurately represent human foot stiffness caused by the arch. Human foot stiffness varies from softer medial to stiffer lateral sides due to the arch's influence [5]. The straight beam can only produce

one bending stiffness for the entire length, lacking this variation. Additionally, the analytical solution assumes fully 2D bending, vertical force application, and a straight beam [40], conditions not fully met in the human foot. Thus, despite its simplicity, this model poorly represents the actual problem.

5.3. Arched Beam

The arched beam geometry better represents the human foot by incorporating its arch shape while maintaining simple beam geometry (see Figure 5.1). Measurements from the author's foot define the arch height, location, and horizontal length.

However, due to unfulfilled assumptions in the bending stiffness equation [40], it is not fully valid for this shape. Thus, FEM simulations under cantilever bending conditions analyze the physical behavior of this arched beam (see Figure 5.1). This approach enables a closer examination of arch-induced stiffness effects, which are crucial in human foot mechanics.

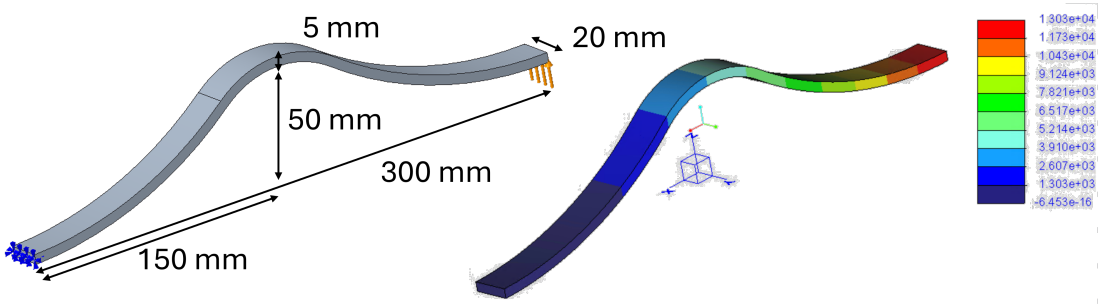

Figure 5.1.: Vertical displacement result for a cantilever bending FEM simulation on the arched beam.

Though more accurate than the straight beam, the arched beam still does not fully capture foot stiffness and boundary conditions. During walking, the lateral foot side is stiffer and more stable due its ground contact between the heel and toe joint, caused by its lower arch height [41][5]. Conversely, the medial side has the highest arch height and less ground contact [42], as visible in the foot pressure print (Figure 2.4). This exhibits the foot adapting to different locomotion demands via varied arch stiffness [23].

The medial and lateral sides interact structurally [43], with the overall foot shape governed by longitudinal and transverse arches. They form a triangular support with the lateral arch across the toe joints, heel, and lateral side (Figure 5.2). This explains the

human foot's complex 3D stiffness from three vertical ground supports, underscoring the limitation of beam-like models to represent this behavior.

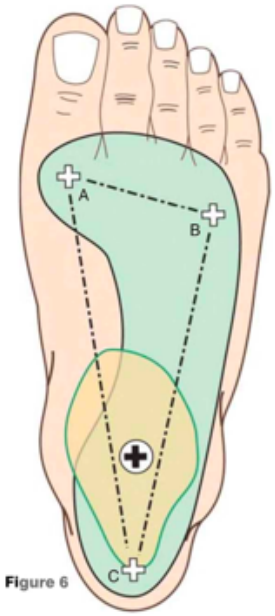

Figure 5.2.: The structural coupling of the medial and lateral arch on the foot. AC represents the medial arch. It is significantly more arched than the lateral arch BC. This results in the green foot pressure print [43].

5.4. Arched Plate

The arched plate geometry represents the human foot arch by having an elevated arch on the medial side that gradually decreases in height towards the flat lateral side. This captures the natural variation of arch height across the foot, providing a bioinspired structural form to study foot arch behavior and stiffness distribution.

5.4.1. Design Approach

The bioinspired arched plate design is a single structure that models the geometry of the foot arch. It better represents the foot's boundary conditions than the previous straight and arched beams, with vertical ground support on three sides: the two shorter sides (representing the toe joint and heel surfaces) and the lateral side, which remains

flat with no arch. Various arched plate designs are created to explore how different arch geometries affect displacement, rebound direction, strain energy, and stiffness. Due to limited literature, this phase observes how these geometric variations influence the foot's mechanical behavior.

Symmetric Arch

The symmetric arched plate geometry, resembling the shape of an arched sole, features an arch peak located at the longitudinal center (see Figure 5.3a). Due to the absence of dimensional references in literature, measurements from the author's own foot were used. The arch shows zero slope at both the peak and the longitudinal ends. The plate length is based on TORO's current foot length, while the width is increased beyond average foot width to allow clearer visualization of FEM results on the arch surface.

Asymmetric Arch

The asymmetric arched plate is studied to analyze how the arch peak location affects the plate's properties (see Figure 5.3b). It features an arch peak positioned away from the longitudinal centerline. The plate length, width, and peak height remain unchanged. The slopes at the arch peak and longitudinal ends remain zero.

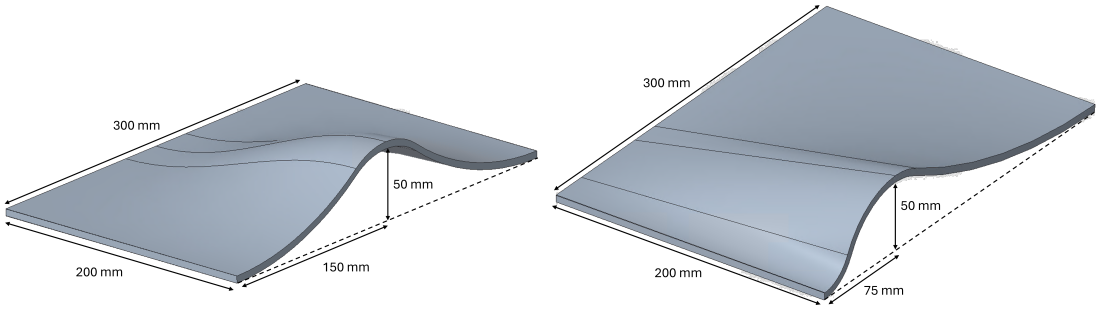

(a) Symmetric arch. (b) Asymmetric arch.

Figure 5.3.: CAD model of the arched plates.

5.4.2. FEM Simulation

The complex 3D geometry of the arched plate renders the use of analytical bending equations unsuitable, which suit simpler structures like straight beams. Therefore, Finite Element Method (FEM) simulations are performed to study three main properties:

vertical displacement, rebound direction, and strain energy. This approach captures the plate's physical behavior more accurately.

Methods

Point Compression Point compression simulations are the first tests performed. Each involves applying a compressive load at a specific point on the arch surface to study overall property distribution. Vertical point loads of 1000 N applied, which is intentionally higher than TORO's body weight (745.56 N) to amplify these distributions for clearer analysis.

Load cases apply loads at various longitudinal points on the medial, center, and lateral regions (see Figure 5.4). The lateral side and longitudinal ends are fixed to simulate the stable ground contact of the human foot. Studying vertical displacement and strain energy results for each load case reveals the arch surface's response to vertical loading.

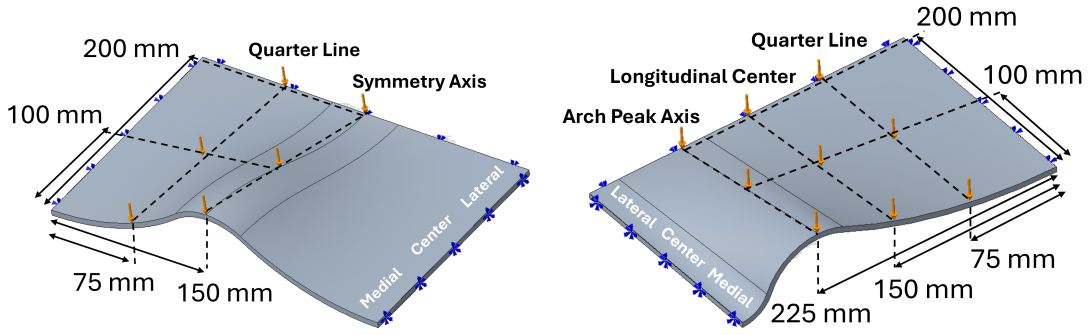

(a) Symmetric arched plate.

(b) Asymmetric arched plate.

Figure 5.4.: Load and boundary conditions for the point compression FEM simulation on the arched plates.

Mid-Stance Mid-stance simulations study the effect of ankle rotation on the arched plate. The load cases, apply a 1000-N vertical upward force at one longitudinal end to reproduce the forward shift of plantar pressure during mid-stance (see Figure 5.5). The opposite longitudinal end is fixed to simulate stable toe contact. The higher load amplifies property distributions, making the plate's behavior clearer for analysis.

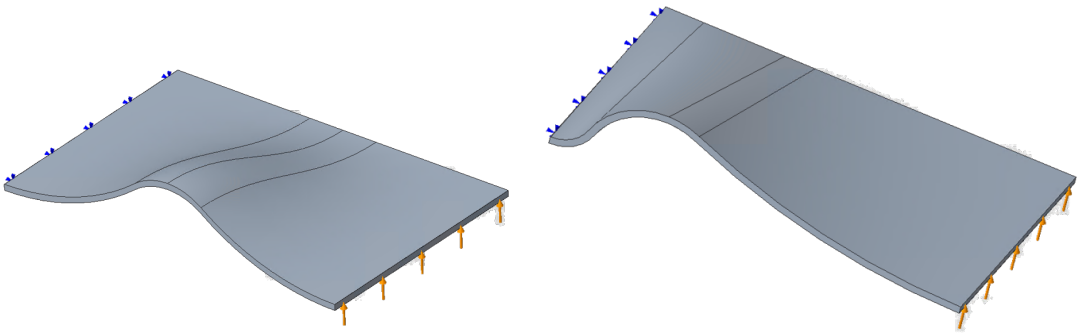

(a) Symmetric arched plate. (b) Asymmetric arched plate.

Figure 5.5.: Load and boundary conditions for the mid-stance FEM simulation on the arched plates.

Vertical Displacement

Symmetric Arched Plate, Symmetry Axis Point compression simulations on the symmetric axis of the symmetric arched plate are conducted. The vertical displacement distributions are shown in Figure 5.6.

Results Medial-region loading generates maximum vertical displacement at the arch peak and its adjacent inflection points. Displacement decreases parabolically toward the lateral side along the plate length, symmetrically about the centerline. Displacement on the lateral region is less than 1% of the maximum.

Center-region loading produces maximum displacement near the inflection points, with magnitude about 20% of that under medial loading. A similar parabolic and symmetrical displacement pattern is observed, with the lateral region also experiencing under 1% of the maximum displacement.

Lateral-region loading results in vertical displacement values roughly three orders of magnitude smaller than those seen in medial or central loading cases, with similarly low lateral displacements.

Discussion The prominent inflection points align with beam theory, which predicts that areas of high curvature concentrate bending strains. These regions with high curvatures and deflection changes, or contraflexures, are zones with zero bending moment [44]. They act as geometric "hinges", focusing vertical displacement under point loads at the arched plate's inflection points.

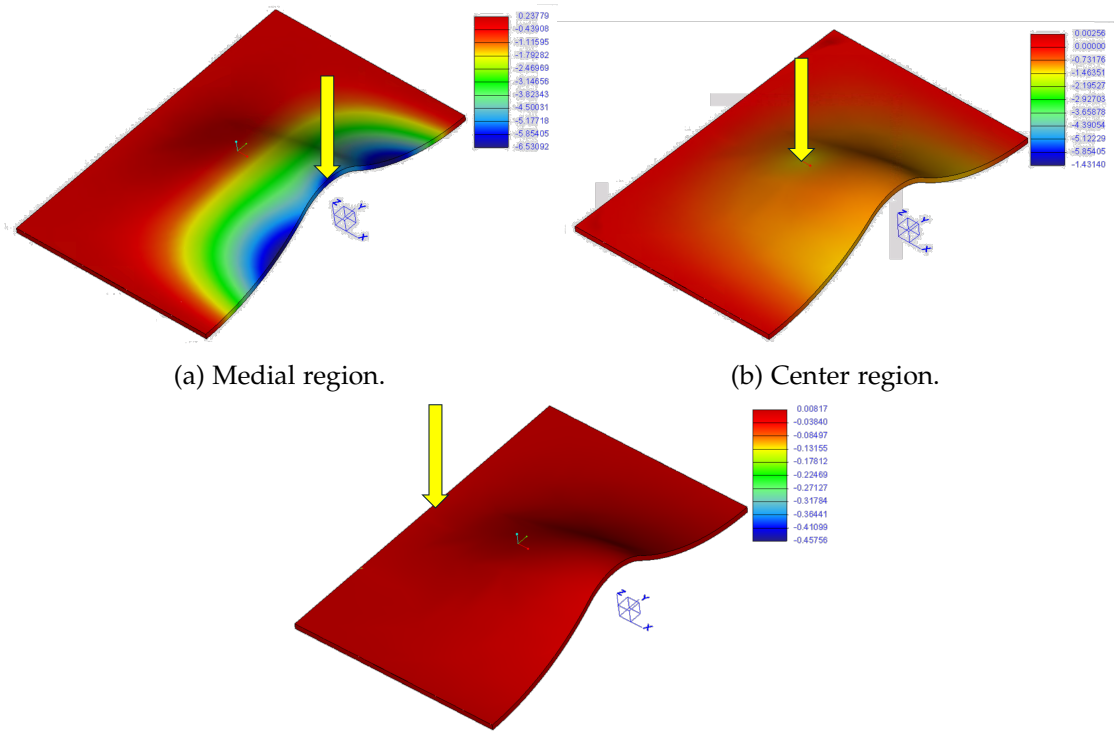

(a) Medial region.

(b) Center region.

(c) Lateral region.

Figure 5.6.: Vertical displacement distributions from the point compression FEM simulations on the three regions along the symmetric axis on the symmetric arched plate.

Curvatures decrease toward the lateral region, causing reduced vertical displacements there. The less pronounced contraflexures and shorter lever arm to the lateral support increased bending stiffness in this region, resulting in the observed low stiffness laterally and high stiffness medially.

Symmetric Arched Plate, Quarter Line Point compression simulations are also carried out on the quarter line of the symmetric arched plate. The displacement distributions are shown in Figure 5.7.

Results Medial-region loading causes the largest vertical displacement at the loaded inflection point. Displacement decreases in a slanted parabolic pattern toward the lateral side, peaking on the loaded side. The distribution is asymmetric about the central axis. The lateral region displacement stays below 1% of the maximum.

Center-region loading creates a large maximum displacement near the arch inflection points in the medial and central regions. This maximum displacement reaches about 16% of the medial loading case. Overall displacement magnitudes are lower than in the medial loading case, with insignificant displacement on the unloaded side. The lateral region also experiences less than 1% of the maximum displacement.

Lateral-region loading results in vertical displacements roughly three orders of magnitude smaller than the other cases, with similarly low values throughout the arch surface.

Discussion The larger displacement along the quarter line matches beam theory predictions. Loads applied near the inflection point, which is a contraflexure zone. This zone experiences lower effective bending stiffness, enabling displacements more than double those at the symmetry axis [44].

Displacement concentrates on the loaded side of the symmetry axis, increasing magnitudes due to a longer lever arm from the load location to the opposite longitudinal end. This longer lever arm reduces resistance to bending, lowering the effective bending stiffness of that region [45].

Asymmetric Arched Plate, Arch Peak Axis Point compression simulations are performed on the asymmetrical arched plate. The vertical displacement results from loads applied on the arch peak axis are shown in Figure 5.8.

Results Medial-region loading produces maximum vertical displacement at the inflection point on the longer side. Displacement decreases in a parabolic pattern

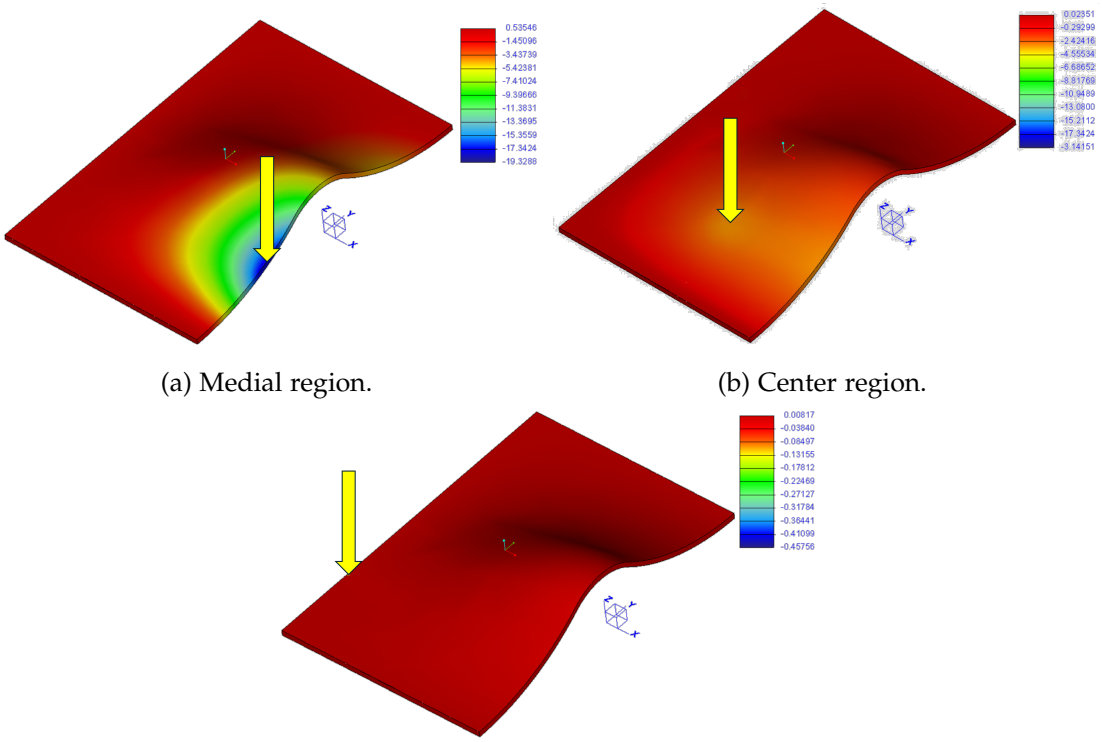

(a) Medial region.

(b) Center region.

(c) Lateral region.

Figure 5.7.: Vertical displacement distributions from the point compression FEM simulations on the three regions along the quarter line on the symmetric arched plate.

toward the lateral side, concentrating mainly on the longer side. The lateral side shows less than 1% of the maximum displacement.

Center-region loading results in maximum displacement near the inflection point of the longer side. This displacement reaches 23% of the medial loading case's magnitude and spreads over a wider area. The lateral side and the shorter arch peak side experience less than 1% of the maximum displacement.

Lateral-region loading causes vertical displacement about two orders of magnitude smaller across the arch surface, with similarly low values on the lateral side.

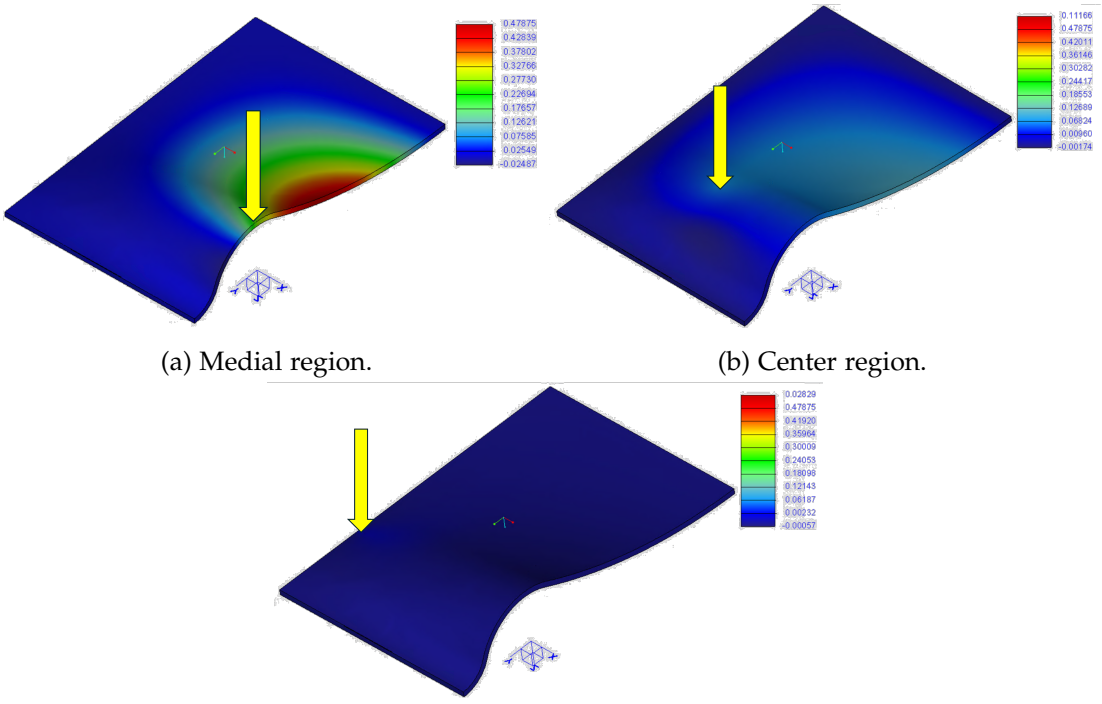

(a) Medial region.

(b) Center region.

(c) Lateral region.

Figure 5.8.: Vertical displacement distributions from the point compression FEM simulations on the three regions along the arch peak axis on the asymmetric arched plate.

Discussion The asymmetric arched geometry shifts the inflection point location, altering behavior consistent with beam theory [44]. The contraflexure moves with the inflection point, shown by increased displacement and reduced bending stiffness in that region.

Additionally, the high-displacement area is larger than in the symmetric arch. This results from the longer lever arm between the loaded region and the longitudinal end on the loaded side, which lowers the bending stiffness. The influence of the shorter, unloaded side is reduced, further decreasing stiffness [45].

Point Compression on Longitudinal Center Point compression tests are applied along the longitudinal center line of the asymmetric arched plate. The vertical displacement contour plots for the loads applied are shown in Figure 5.9.

Results Medial-region loading generates maximum vertical displacement at the inflection point on the longer side. Displacement decreases parabolically toward the lateral side, concentrating on the longer side while spreading wider laterally. Displacements on the lateral side and shorter arch peak are less than 1% of the maximum.

Center-region loading also maximizes displacement near the longer side's inflection point. The magnitude reaches about 22% of the medial loading case and the displacement spreads wider than in the medial loading. The lateral side and shorter arch peak side again exhibit less than 1% of the maximum displacement.

Lateral-region loading induces vertical displacements roughly two orders of magnitude smaller throughout the arch surface, with similarly low lateral values.

Discussion The larger displacement observed aligns with beam theory. Loads applied near the contraflexure, marked by the inflection point where bending moment changes sign, experience lower effective bending stiffness [44]. This location allows maximum displacement more than three times greater than at the arch peak axis. The behavior is similarly exhibited by the quarter-line load cases on the symmetric axis.

Point Compression on Quarter Line Point compression simulations are applied along the quarter line on the longer side adjacent to the arch peak. The vertical displacement contour plots for the loads applied are shown in Figure 5.10.

Results Medial-region loading causes maximum vertical displacement at the inflection point on the longer side. Displacement decreases in a parabolic profile toward the lateral side. The displacement concentrates on the longer side and spreads wider laterally. The lateral region and shorter arch peak side show less than 1% of the maximum displacement.

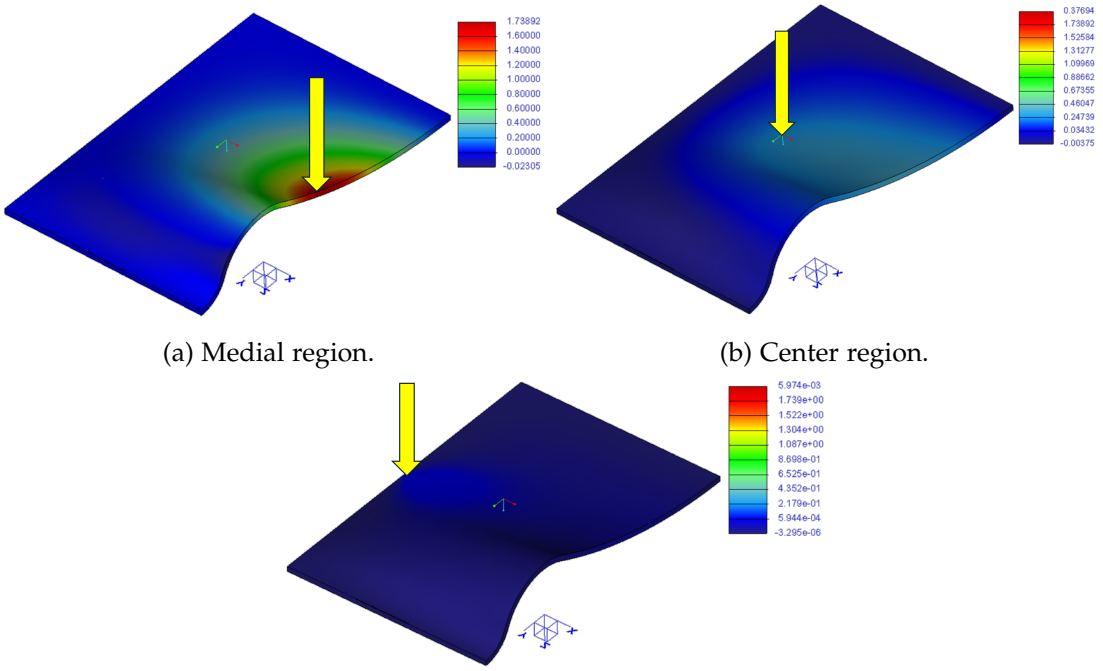

(a) Medial region.

(b) Center region.

(c) Lateral region.

Figure 5.9.: Vertical displacement distributions from the point compression FEM simulations on the three regions along the longitudinal center on the asymmetric arched plate.

Loading on the center region also causes maximum displacement near the longer side's inflection point, with a magnitude about 22% of the medial loading case. Displacements are lower than in the medial loading case and spread over a wider area. The lateral and shorter sides again have less than 1% of the maximum displacement.

Lateral-region loading induces vertical displacement about three orders of magnitude smaller across the arch surface. The lateral side displacement remains similarly low.

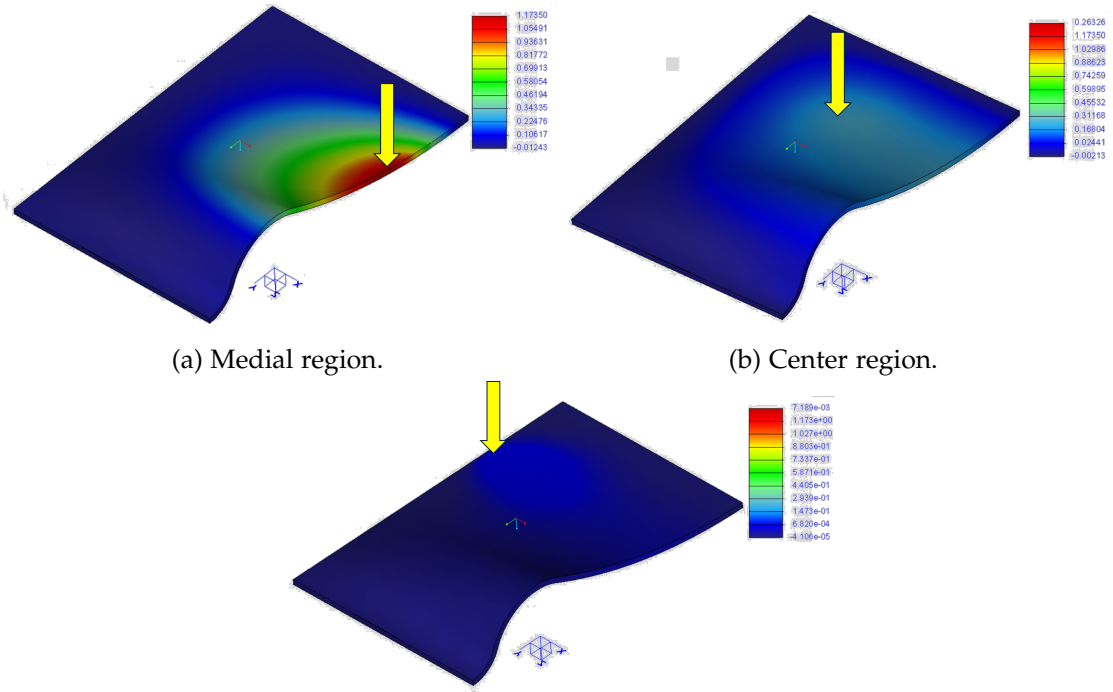

(a) Medial region.

(b) Center region.

(c) Lateral region.

Figure 5.10.: Vertical displacement distributions from the point compression FEM simulations on the three regions along the quarter line on the asymmetric arched plate.

Discussion The larger displacement observed aligns with beam theory predictions. These cases apply load near the contraflexure marked by the inflection point, which exhibits lower effective bending stiffness. This results in a maximum displacement more than three times greater than that at the arch peak axis [44].

However, the maximum displacement here is lower than in the longitudinal center load cases. This difference arises because the longitudinal end support plays a larger role. The lever arm between the quarter line load and the longitudinal end is shorter,

which increases bending stiffness [45]. At the same time, the load position deviates further from the contraflexure than the longitudinal center, demonstrating how the interplay between inflection point location and support lever arm affects bending stiffness.

Vertical Displacement Conclusion One-way ANOVA is conducted on the maximum vertical displacement results from the three regions to assess their statistical significance Table 5.1. This analysis tests whether the mean vertical displacements differ significantly between the regions.

One-Way ANOVA Analysis of Maximum Vertical Displacement		
Arched Plate	**F-Statistic**	**p-Value**
Symmetric	10.22	0.01
Asymmetric	7.44	0.02

Table 5.1.: One-way ANOVA variance analysis on the vertical displacements for the three regions. Assumed lateral rigidity yields 0 mm vertical displacement.

The p-values below or equal to 0.05 and the high F-statistics indicate significant differences in maximum vertical displacements among the three foot regions. This confirms that stiffness varies significantly across the medial, center, and lateral regions under all load cases and geometries. The result supports the conclusion that stiffness increases from the medial to the lateral side.

Rebound Direction

The rebound direction defines the path the foot follows after unloading. This parameter evaluates how the arched geometry influences the release of strain energy after mid-stance.

The calculation focuses on the load application points. Using the 3D Pythagorean theorem, the 3D displacement vector components α, β, and γ along the x-, y-, and z-axes, respectively, are computed using Equations 5.3-5.5 [46]. Here, x, y, and z are the displacement magnitudes at the point after loading.

$$\alpha = \frac{x}{\sqrt{x^2 + y^2 + z^2}}, \tag{5.3}$$

$$\beta = \frac{y}{\sqrt{x^2 + y^2 + z^2}}, \tag{5.4}$$

$$\gamma = \frac{z}{\sqrt{x^2 + y^2 + z^2}}. \tag{5.5}$$

Simulations focus on the medial and center regions along the quarter lines because these align with the arch's inflection point, which is a contraflexure. This contraflexure promotes large displacements due to its low effective bending stiffness [44]. Medial and center regions are chosen since they bear the highest average load and energy return in the human foot [47].

Displacement vector components calculated from these simulations directly determine the displacement direction at the load points. Consequently, the rebound direction components are the negative of these displacement components, indicating the direction the foot moves after unloading.

Results The rebound direction vector components are summarized in Table 5.2. Visual representations of rebound directions for each simulation appear in Figure 5.11. One-way ANOVA results assessing the significance of rebound direction differences are shown in Table 5.3.

Discussion The high F-statistics and p-values below 0.05 indicate strong significance in the rebound direction vector projections across the three foot regions. This confirms that these regions exhibit distinctly different rebound directions. The particularly high F-statistic for the vertical displacement component γ aligns with simulation results, signaling significant variation in vertical movement. Meanwhile, the relatively lower significance for the longitudinal component β suggests more similar displacement along the length of the foot, likely due to uniform arch slope in that axis.

Vector Components of Rebound Direction of Load Application Point			
Load Case	α	β	γ
Symmetric Plate, Medial	-0.094	-0.054	0.994
Symmetric Plate, Center	-0.089	-0.113	0.990
Symmetric Plate, Lateral	0.000	0.000	0.000
Asymmetric Plate, Medial	-0.100	-0.067	0.993
Asymmetric Plate, Center	-0.080	-0.076	0.995
Asymmetric Plate, Lateral	0.000	0.000	0.000

Table 5.2.: Vector components of rebound direction of the load application point for different load cases on the arched plates. α, β, and γ refer to the vector projections on the x-, y-, and z-axes respectively.

One-Way ANOVA Analysis of Rebound Direction		
Vector Projection	**F-Statistic**	**p-Value**
α	358.49	0.00
β	17.04	0.02
γ	207599.10	0.00

Table 5.3.: One-way ANOVA variance analysis on the rebound vector projections for the three regions. Assumed lateral rigidity yields 0 displacements.

Rebound tends to direct toward the lateral hindfoot area, consistent with displacement patterns. Under load, displacement occurs toward the medial side due to its lower stiffness. The arched geometry introduces a longitudinal load component along the quarter line, pushing the point forward, so rebound upon unloading moves oppo-

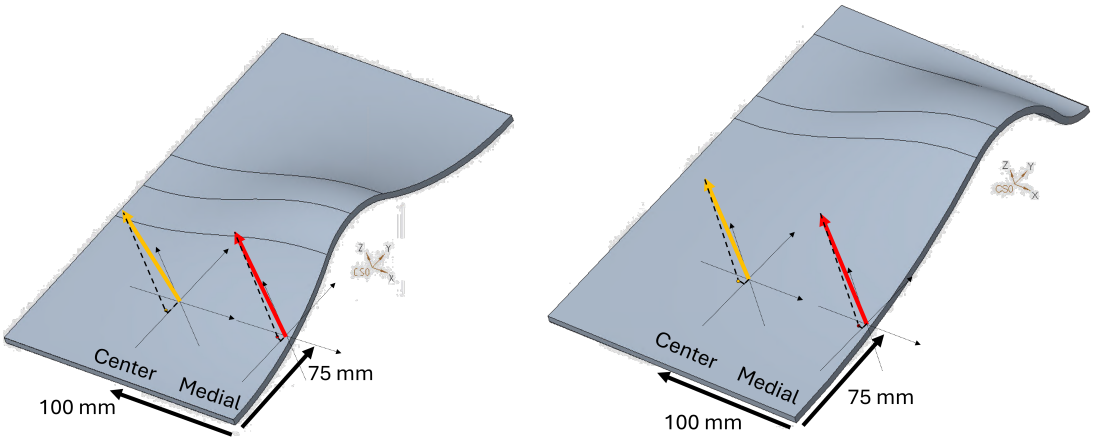

(a) Symmetric arched plate.

(b) Asymmetric arched plate.

Figure 5.11.: Rebound direction of the arched plates. The red and orange arrows represent the rebound direction of the load application points on the medial and center regions respectively. Local coordinate systems are displayed on the load application point for visualization.

sitely—away from the medial region and toward the foot's rear lateral side.

These findings match biomechanical literature, showing that energy stored during mid-stance releases during push-off [17] with slight foot inversion [48] and adduction [49]. Foot inversion indicates that energy release is directed towards the lateral side of the foot. Foot eversion in the early stance phases also verifies the energy absorption by the medial region [50]. Thus, inversion during push-off realizes energy release in the opposite direction. Forefoot adduction further confirms energy is released laterally towards the hindfoot.

The process also relates to midtarsal joint locking [51]. The mechanism stiffens the foot for efficient forward propulsion [52]. Despite lacking extensive quantitative foot rebound studies, results strongly align with biomechanical principles.

However, complex gait dynamics involving bones, muscles, and tendons limit direct simulation applicability [53]. Foot behavior at push-off is therefore not necessarily aimed towards optimizing energy release. The midtarsal locking, for instance, also serves stability and not just energy release [52]. The model also does not capture all load and boundary conditions of energy storage/release. Simplified point compression is used instead of continuous center of pressure trajectories. The model also only represents the arch and not the full foot structure. These factors temper direct extrapolation but do not negate the core findings.

Strain Energy

Strain energy is defined as the elastic energy stored due to elastic deformation under loading [54]. The different arch geometries are studied to observe how they impact strain energy storage. Point compression and mid-stance simulations are conducted on the arched plates to evaluate strain energy.

Point Compression on Symmetric Arch Point compression simulations on the symmetric arched plate are conducted on the medial, center, and lateral regions across the symmetric axis. The strain energy distributions are shown in Figure 5.12.

Results Medial- and center-region loading concentrates the strain energy in the two inflection points and longitudinal ends. Center-region loading generates 20% lower maximum strain energy and less concentration in the inflection points. The induced strain energy upon lateral-region loading is less than 1% of the maximum.

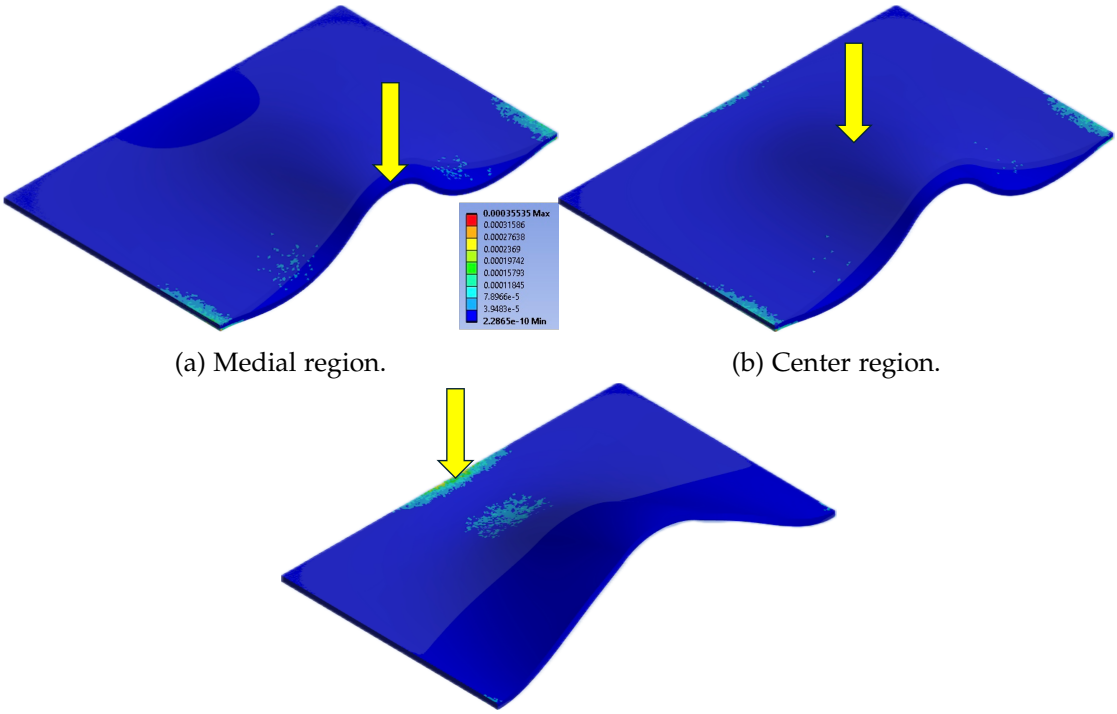

(a) Medial region.

(b) Center region.

(c) Lateral region.

Figure 5.12.: Strain energy distributions from the point compression FEM simulations along the symmetry axis on the symmetric arched plate.

Discussion The similarity between strain energy and vertical displacement distributions indicates their proportionality, consistent with structural mechanics. Strain energy calculation depends on displacement values [55], so both share regions of high concentration. The 20% decrease in maximum values from medial to center loading in both quantities supports this proportionality. This behavior aligns with beam theory and low stiffness in contraflexure zones [44].

Unpredicted strain energy concentration in the lateral region and longitudinal ends results from boundary conditions in the FEM, where the lateral side is fixed. A more accurate boundary condition would constrain motion to a plane without vertical displacement but still allow some movement. However, this constraint does not fully constrain the model. Despite this limitation, the results remain valid.

Point Compression on Asymmetric Arch Point compression simulations on the asymmetric arched plate are also carried out across the arch peak axis. The strain energy contour plots over the asymmetric arched plate are shown in Figure 5.13.

Results Medial- and center-region loading concentrates the strain energy in the inflection point of the longer side and longitudinal ends. Center-region loading generates 23% lower maximum strain energy and less concentration in the inflection points. The induced strain energy upon lateral-region loading is less than 1% of the maximum.

Discussion Similarities between strain energy and vertical displacement distributions indicate their proportionality [55]. Because strain energy depends on deformation, both show high-concentration regions. The 23% decrease in maximum magnitude from medial to center loading supports this relationship. This confirms that beam theory and low contraflexure stiffness govern strain energy behavior [44].

The unpredicted high strain energy on the lateral region during lateral loading is due to unrepresentative FEM boundary conditions. Despite this, the plate's property behaviors remain valid.

Mid-Stance Simulation on Symmetric Arch A mid-stance simulation is conducted on a symmetric arched plate. One longitudinal end is fixed, while a 1000-N vertical force is applied at the opposite end. This setup induces amplified strain energy distributions across the plate.

Results The strain energy distribution is shown in Figure 5.14a. Maximum strain energy localizes on the lateral region at the fixed longitudinal end. High concentrations extend along the lateral side from the fixed end to the symmetry axis. The medial and

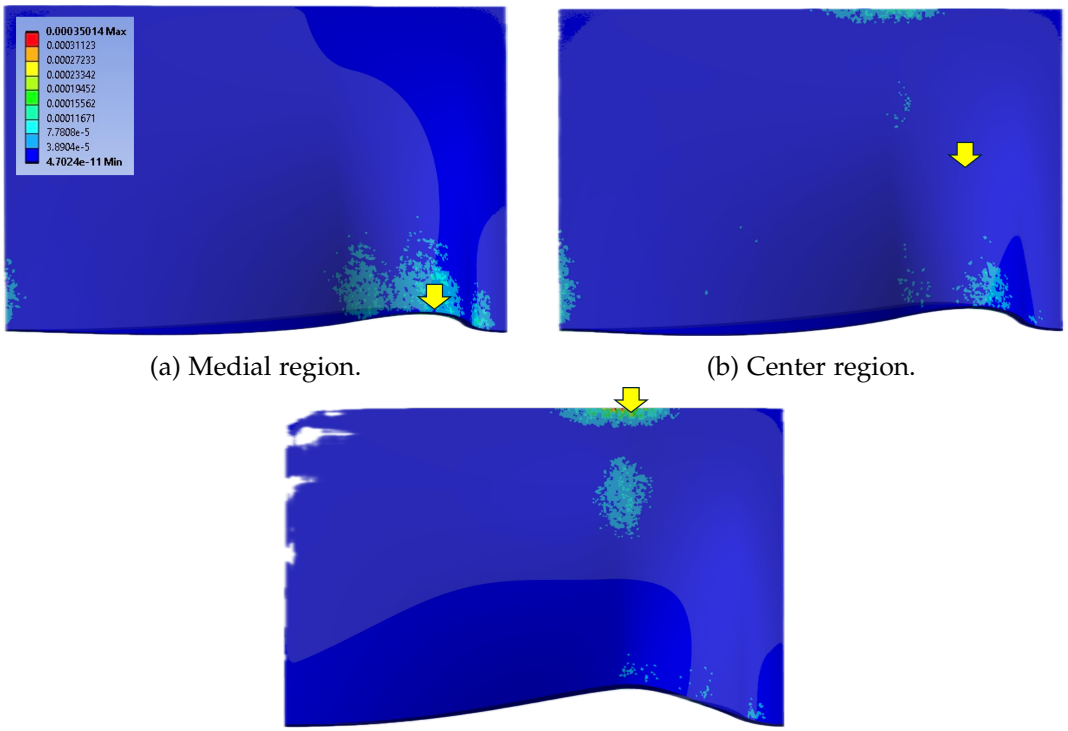

(a) Medial region.

(b) Center region.

(c) Lateral region.

Figure 5.13.: Strain energy distributions from the point compression FEM simulations along the arch peak axis on the asymmetric arched plate.

center regions near the loaded end quarter line also show elevated strain energy. The unloaded side exhibits less than 1% of the maximum strain energy.

The von Mises elastic strain distribution is studied to aid the strain energy analysis due to their relation [56]. The distribution is shown in Figure 5.14b. The region with maximum elastic strain is observed along the lateral side.

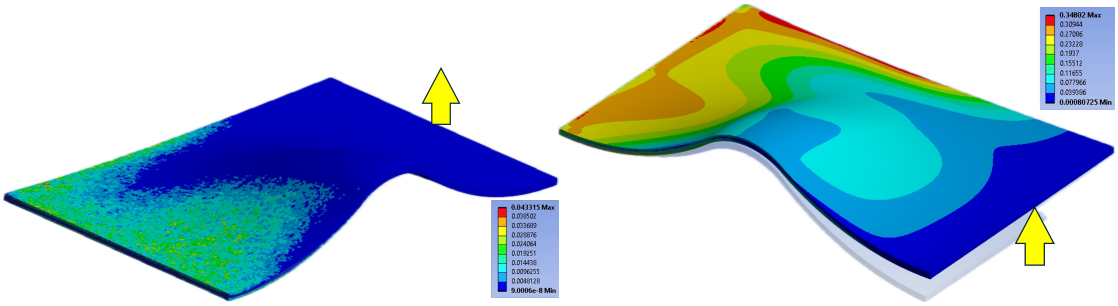

(a) Strain energy.

(b) Elastic strain.

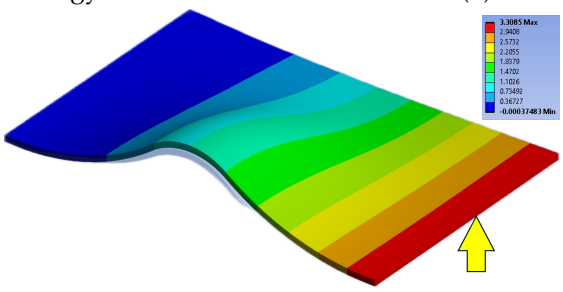

(c) Vertical displacement.

Figure 5.14.: FEM simulation results for mid-stance simulation on the symmetric arched plate.

Discussion The high lateral strain energy contradicts findings of greater medial energy storage due to the arch. This arises because the simulation applies vertical force over the entire longitudinal end surface, creating evenly distributed vertical displacement along the length (see Figure 5.14c).

This force effect overrides stiffness differences caused by the arch shape. A medial tilt to balance lateral strain is predicted. Still, the higher lateral strain compared to medial and center regions under equal vertical displacement shows its greater stiffness.

Mid-Stance Simulation on Asymmetric Arch Mid-stance simulation is also performed on the asymmetric arched plate. The fixed constraint is applied on one longitu-

dinal end of the arched plate. A vertical force is applied on the opposite longitudinal end.

Results The strain energy distribution in Figure 5.15a shows maximum values on the lateral and center regions near the fixed longitudinal end. High strain energy extends along the lateral side from the fixed end to near the arch peak. Elevated energy is also seen near the medial and center regions of the inflection point on the shorter side, while the longer side shows negligible values.

The von Mises elastic strain distribution in Figure 5.15b resembles that of the symmetric arch, peaking along the lateral side and the fixed side of the arch peak. The distribution is more concentrated due to the shorter distance between the arch peak and the fixed end. This similarity further supports the correlation between strain energy and elastic strain in the asymmetric arch.

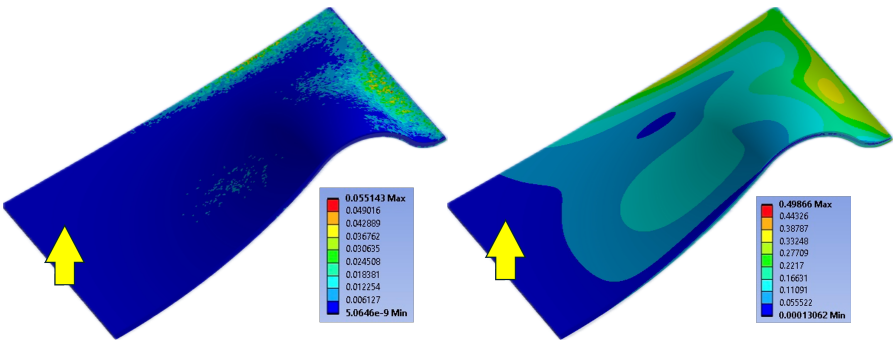

(a) Strain energy. (b) Elastic strain.

Figure 5.15.: FEM simulation results for mid-stance simulation on the symmetric arched plate.

Discussion The evenly distributed vertical displacement in the longitudinal direction affects the results. Similar to the symmetric arched plate, higher strain appears on the lateral region than the medial and center regions. Thus, the conclusion about the properties of these regions remains valid.

The higher maximum strain energy at the inflection point on the short side is due to the smaller space between the arch peak and the fixed end. Its increased bending stiffness allows it to resist mid-stance displacements more effectively [45]. From point compression tests, the inflection point, as a contraflexure, influences vertical displacement [44]. Hence, both the inflection point and the length between the fixed end and arch peak affect mid-stance behavior.

5.4.3. ZwickRoell Testing

Compression testing on the ZwickRoell universal testing machine (BZ1-MM14450.ZW04 10kN) validates the FEM-predicted vertical displacement of arched plates under load. The test measures component stiffness as the ratio of applied compressive force to the resulting displacement.

3D Printing

The designs are printed out of PLA via Fused Deposition Modeling (FDM) using Prusa MK4. The printed arched plates are shown in Figure 5.16. The selected infill setting is the gyroid pattern at 15% infill density, as it offers an optimal balance of strength, efficiency, and print speed [57]. The designs are printed at 50% scale due to printer size constraints. The property distributions scale down accordingly.

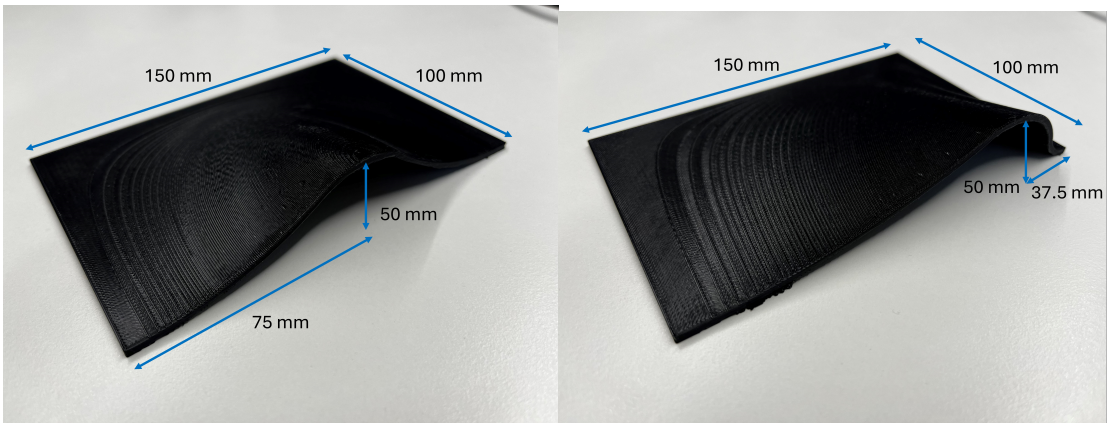

(a) Symmetric arched plate. (b) Asymmetric arched plate.

Figure 5.16.: 3D-printed arched plates at 50% scale.

Test Setup

The experimental setup is shown in Figure 5.17. The plate is fixed on its lateral side with duct tape, allowing deformation of the arched medial side while keeping the lateral side restrained. This replicates the boundary condition of a real human foot.

Point compression tests generate displacement distributions on the arch surface. The calculated stiffness from a singular force and displacement data fundamentally describes the quantity as spring stiffness k and calculated by Equation 5.6. $F_{compression}$

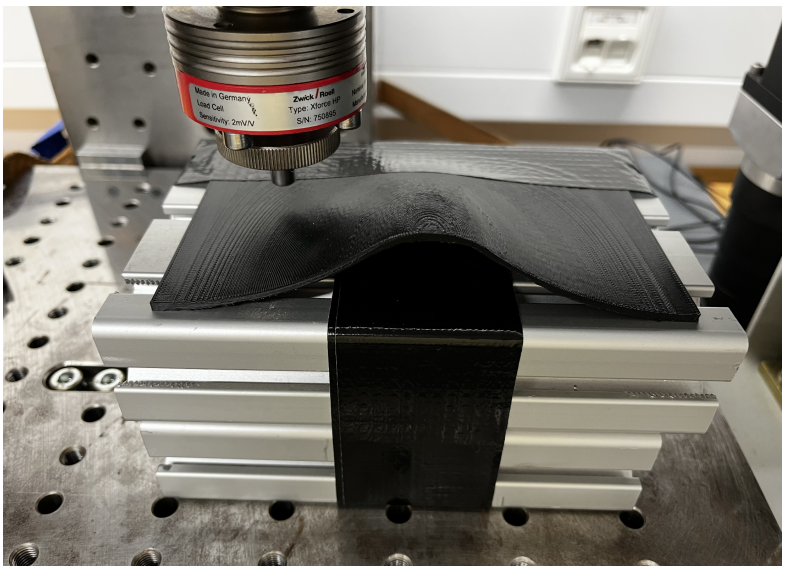

Figure 5.17.: ZwickRoell test setup for compression test on arched plate.

is the applied compression force and z is the vertical displacement recorded. This provides a fundamental measure of stiffness from singular force-displacement data.

$$k = \frac{F_{compression}}{z} \tag{5.6}$$

The tested points on the arch surface are divided into three regions: medial, center, and lateral (see Figure 5.18). Points are spaced 10 mm apart longitudinally. A compression force of 30 N is applied to induce sufficient deformation without platform collision. The resulting vertical displacement is recorded, and the spring stiffness for each point is calculated independently using this data.

Results

The calculated stiffness values appear in Table 5.4, with magnitudes visualized as colors on the arched surfaces in Figure 5.19. One-way ANOVA is performed to assess the significance of these stiffness differences. The results of this analysis are summarized in Table 5.5.

Discussion No vertical displacements are induced upon lateral loading. This is predicted, as the lateral side is designed to rest flat on the ground. Thus, it is considered rigid and not displayed in the displacement data.

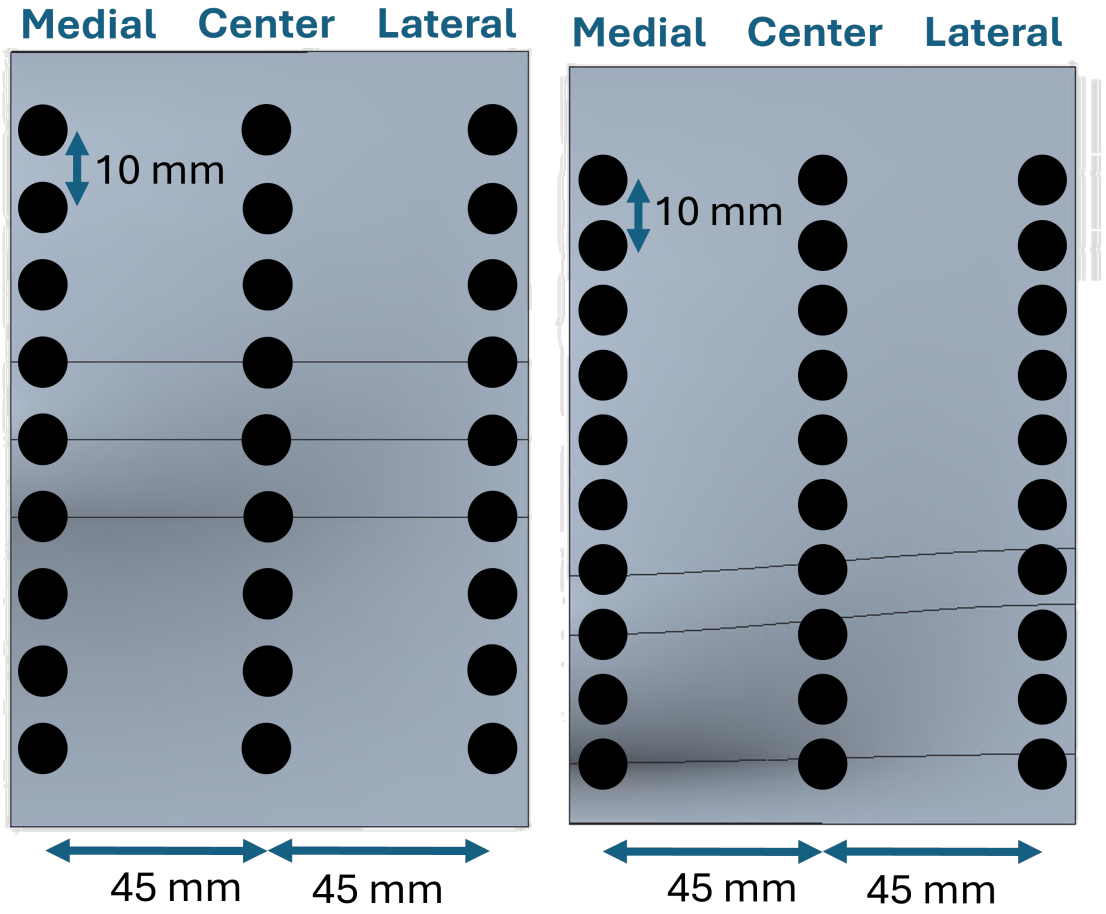

(a) Symmetric arched plate.

(b) Asymmetric arched plate.

Figure 5.18.: ZwickRoell compression testing points on the arched plates. 10 mm longitudinal offset applies between every point.

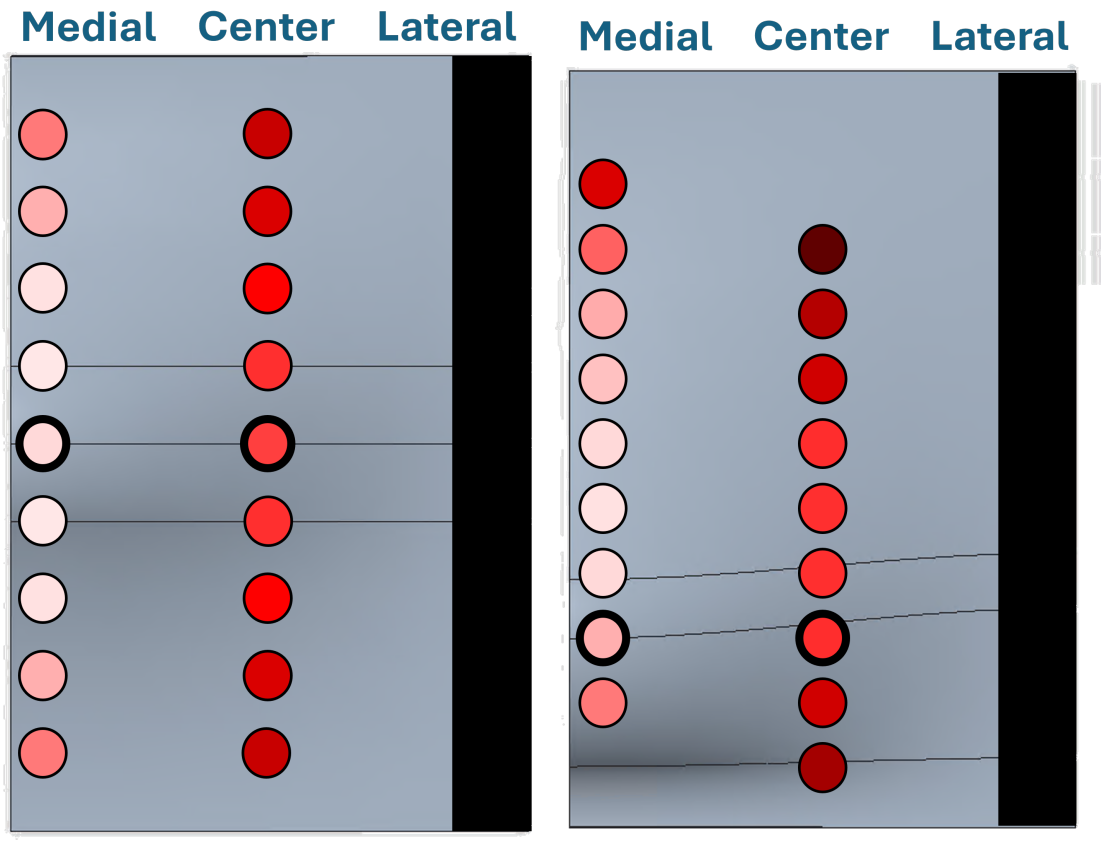

(a) Symmetric arched plate.

(b) Asymmetric arched plate.

Figure 5.19.: Spring stiffness distribution of the arched plates from ZwickRoell compression test. Darker shades of red signify higher stiffness magnitudes. Points on the lateral side are considered to be rigid due to lack of vertical displacement during testing. The points with dark outlines are located on the symmetric and arch peak axes. These points represent the zero reference for the longitudinal positions.

Stiffness Results (N/mm) from ZwickRoell Compression Test				
Longitudinal Position (mm)	**Symmetric**		**Asymmetric**	
	Medial	**Center**	**Medial**	**Center**
-20	-	-	-	54.55
-10	-	-	15.38	33.33
0	7.23	18.75	10.91	25.00
10	6.25	20.00	7.23	21.43
20	6.82	27.27	6.82	21.43
30	9.52	30.00	7.06	23.08
40	13.64	50.00	9.09	30.00
50	-	-	10.71	42.86
60	-	-	16.67	100.00
70	-	-	31.58	-

Table 5.4.: Calculated spring stiffness of points on arched plates. Darker shades represent high stiffness. The symmetric and arch peak axes are zero longitudinal position references for the symmetric and asymmetric arched plates respectively. Positions without values indicate omitted measurements due to symmetry (symmetric) and adverse testing positions with high arch slopes (asymmetric).

One-Way ANOVA Analysis of Stiffness		
Arched Plate	**F-Statistic**	**p-Value**
Symmetric	12.60	0.01
Asymmetric	8.77	0.01

Table 5.5.: One-way ANOVA analysis on the stiffness of the three regions.

For the symmetric arched plate, the medial region is less stiff than the center, consis-

tent with FEM results. Minimum stiffness appears 10 mm from the arch peak at the inflection point. This matches beam theory predictions for large medial displacements [44].

In the asymmetric arched plate, the medial region also shows lower stiffness than the center. Differences include increased stiffness on the shorter side away from the arch peak and a broad, similar-stiffness zone on the longer side (10–40 mm from the peak) in both regions, reflecting FEM results. This zone arises from the interplay of contraflexure and increased bending stiffness due to the shorter lever arm to the longitudinal end [45].

P-values less tan 0.05 and high F-statistics confirm significant differences in vertical displacement stiffness between medial and center regions across all points and geometries. This validates that stiffness rises from medial to lateral regions.

5.5. Intermediate Conclusion

The tech enabler phase aimed to validate the research foundation. Simple beams allow analytical study but fail to reflect human foot arch boundary conditions. An arched plate with a curved medial side and flat lateral side better models these conditions and serves as the bioinspired geometry.

FEM analysis of symmetric and asymmetric arched plates under vertical compression showed significant stiffness variation across the arch ($p=0.01$). The medial region had the greatest displacement and lowest stiffness. These regions influenced rebound direction, which pointed toward the lateral hindfoot, aligning with biomechanical data. Simulations also revealed strain energy differences, with the medial inflection points storing more energy.

Compression tests on a ZwickRoell machine confirmed these results. The medial region had the lowest stiffness, then center, then lateral, matching FEM predictions.

Overall, the findings demonstrate that arch geometry inherently causes 3D stiffness variations, with the medial side softer than center and lateral. This confirms the motivation to develop a 3D structurally-elastic bioinspired humanoid robot foot design that combines elastic and rigid contact behaviors.

6. Rapid Prototyping Foot

6.1. Motivation

The design phase aims to use learnings from the tech enabler to create a humanoid robot foot structure via rapid prototyping. PLA 3D printing enables quick production and testing of multiple design iterations, providing extensive data for further development. This approach allows evaluation and refinement of various designs efficiently for further development of the 3D structurally-elastic foot.

6.2. Rectangular Plate with Arched Sole and Heel and Toe Contacts

6.2.1. Design Approach

A rectangular flat plate foot with an arched sole and heel and toe contact surfaces is designed based on TORO's current flat aluminum foot. The design keeps the original toe and heel contact areas, with the primary change being the sole arch. This design isolates the arch's effect on an initially flat foot. TORO's foot dimensions serve as the main reference. Two designs are created: one with a symmetric arch and one with an asymmetric arch (Table 6.1, Figure 6.1).

TORO Foot Dimensions	Measurement
Foot Length	190 mm
Foot Width	95 mm
Foot Height	23 mm
Toe Length	30 mm
Heel Length	30 mm

Table 6.1.: Selected dimensions of TORO's current flat foot design.

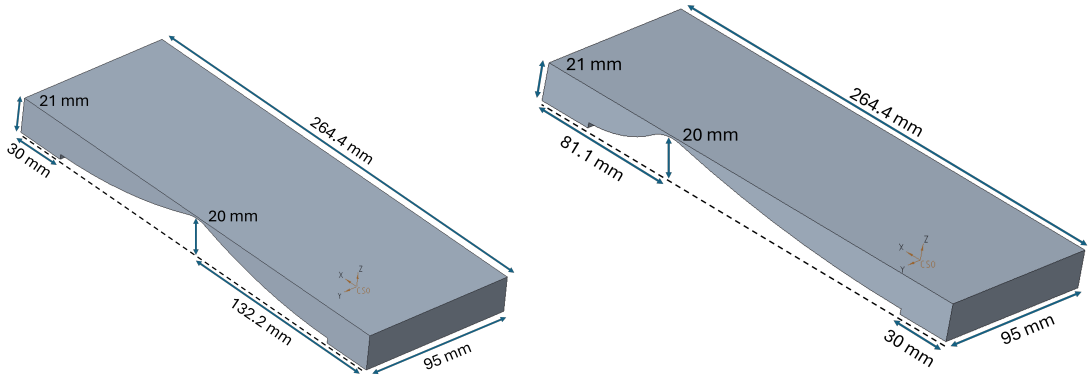

(a) Symmetric arched sole.

(b) Asymmetric arched sole.

Figure 6.1.: CAD models of the rectangular flat foot design with arched sole.

6.2.2. FEM Simulation

The foot design's vertical displacement is analyzed using FEM simulations with fixed supports on the heel and toe contact surfaces. Vertical point compression is applied at multiple points along the foot's symmetry axis to gather initial data on longitudinal properties. For the symmetric arch design, loads are placed on the symmetry axis and quarter line. For the asymmetric arch design, loads are applied on the arch peak axis, longitudinal center, and quarter line. The resulting vertical displacement patterns are shown in Figure 6.2.

Results

For the symmetric arch, loading on the symmetry axis causes a maximum vertical displacement of 0.034 mm in the medial and center regions, distributed symmetrically. Loading on the quarter line produces 29% of this maximum displacement, shifting the displacement peak toward the load point near the inflection point.

For the asymmetric arch, loading on the arch peak axis results in maximum displacement near the inflection point on the longer side, at 54% of the symmetric arch's maximum under symmetry axis loading. This loading also causes 90% greater displacement than loading on the longitudinal center, which is similar to the symmetric arch's symmetry axis loading. Quarter line loading creates 27% of the symmetric arch's max displacement, spreading farther longitudinally with a concentration near the inflection point.

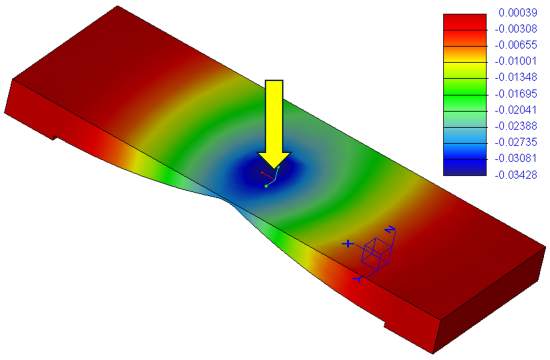

(a) Symmetry axis, symmetric arched sole.

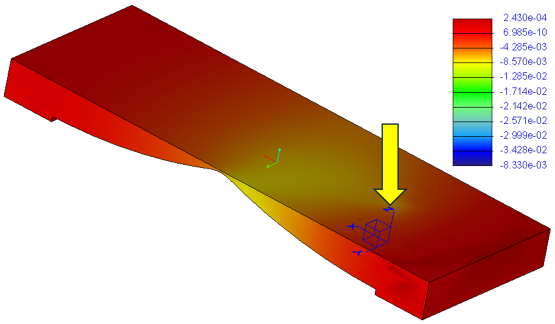

(b) Quarter line, symmetric arched sole.

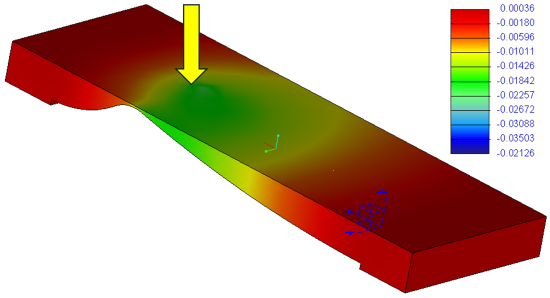

(c) Arch peak axis, asymmetric arched sole.

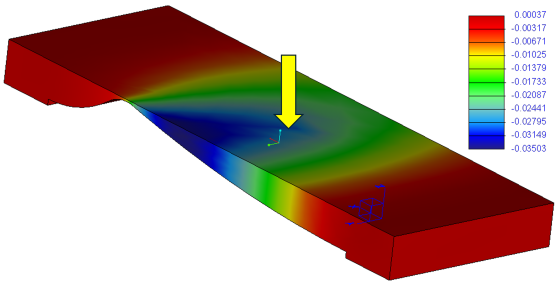

(d) Longitudinal center, asymmetric arched sole.

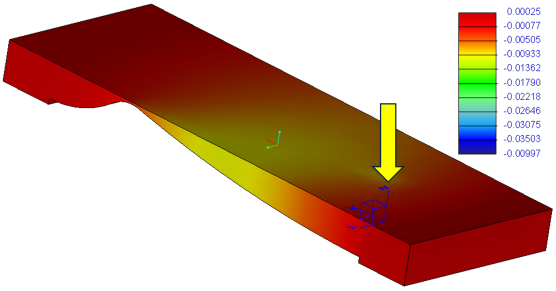

(e) Quarter line, asymmetric arched sole.

Figure 6.2.: Vertical displacement results from point compression FEM simulations on the rectangular flat plates with arched sole. Loads are applied on the center region for all the load cases.

Discussion

The low vertical displacements observed across all load cases indicate high foot stiffness. The arch's thickness varies substantially along its length, which affects stiffness. This shows stiffness distribution is influenced not only by arch geometry but also by thickness variation. Therefore, this design cannot fully isolate the arch's effect.

6.2.3. ZwickRoell Testing

The designs are 3D printed using PLA. Compression testing is carried out on the two designs to verify the FEM simulations. The test protocol is similar to the ZwickRoell test in the tech enabler phase to calculate the spring stiffness.

Results

100 N of vertical compression load is applied on center region points along their longitudinal length to generate amplified displacements for clear analysis. The resulting stiffnesses are displayed in Table 6.2.

Discussion

The ZwickRoell test confirms the high stiffness predicted by FEM simulations. Vertical displacements under a 100 N compression load range from 0.70 to 2.25 mm, indicating significant stiffness values. During testing, the longitudinal ends of the foot lifted, showing that displacement arises from heel and toe lifting rather than arch deformation. This suggests that boundary conditions are not properly met, and the foot's variable thickness adds complexity. These findings reveal that the design cannot isolate the arch's effects fully, and modifications are necessary to address these confounding factors.

6.3. Arched Plate with Heel and Toe Contacts

6.3.1. Design Approach

The arched plate foot with heel and toe contact surfaces is designed to overcome the limitations of the rectangular flat plate foot. This design uses the arched plate concept from the tech enabler phase while retaining the heel and toe contact areas from the flat foot. It maintains the two ground supports and ensures that the arch geometry influences the stiffness behavior. Two versions are created: one with a symmetric arch and one with an asymmetric arch (Figure 6.3).

ZwickRoell Testing on Rectangular Flat Foot		
Longitudinal Position (mm)	**Spring Stiffness (N/mm)**	
	Symmetric	**Asymmetric**
-20	-	142.86
-10	-	100.00
0	44.44	58.82
10	51.28	50.00
20	66.67	50.00
30	90.91	52.63
40	111.11	57.14
50	153.85	62.50
60	200.00	74.07
70	222.22	90.91
80	-	100.00
90	-	125.00
100	-	142.86

Table 6.2.: Calculated spring stiffness from ZwickRoell compression testing on the center region of the rectangular flat foot. Darker shades represent higher stiffness. The arch peak axis is the zero longitudinal position reference. Points without measurements are omitted due to symmetry or rigidity of the heel and toe contacts.

6.3.2. FEM Simulation

Point compression tests are performed in FEM simulations with fixed supports on the heel and toe surfaces. The simulations apply vertical compressive loads at points along the central length of the foot designs to collect initial longitudinal stiffness data. For the symmetric arch design, loads are placed on the symmetry axis and quarter line. For the asymmetric arch design, loads are applied on the arch peak axis, the longitudinal

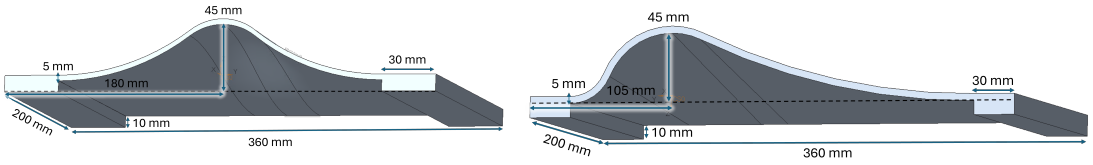

(a) Symmetric arched plate foot.

(b) Asymmetric arched plate foot.

Figure 6.3.: CAD models of the arched plate foot design with heel and toe contacts.

center, and the quarter line. The vertical displacement distributions resulting from these load cases are shown in Figure 6.4.

Results

On the symmetric arched plate foot, loading on the symmetry axis and quarter line causes maximum displacements in the lateral region. The displacement under quarter line loading is 58% lower than that on the symmetry axis. The maximum displacement location shifts longitudinally according to where the load is applied.

For the asymmetric arched plate foot, maximum displacement occurs near the inflection point on the longer side for all loads. The largest displacement is under longitudinal center loading, amounting to 120% and 63% of the displacement under arch peak axis and quarter line loadings, respectively. Lateral region displacements reach 76% of the maximum inflection point displacement across all loads.

Discussion

The integration of the tech enabler arch geometry addresses the previous design's limitations. The medial and center regions show similar displacement behavior, with high displacements near the inflection region following beam theory and contraflexure properties [44]. Thickness variation influence is reduced, enabling a more valid arch stiffness analysis.

The main difference is in the lateral region, where displacement differs by 24% from the medial and center regions. Contrary to previous high rigidity observations, this unexpected lateral displacement arises because the arch geometry is elevated by the heel and toe contact surfaces, leaving the lateral region without ground support. This absence of contact causes deviation from the tech enabler's behavior.

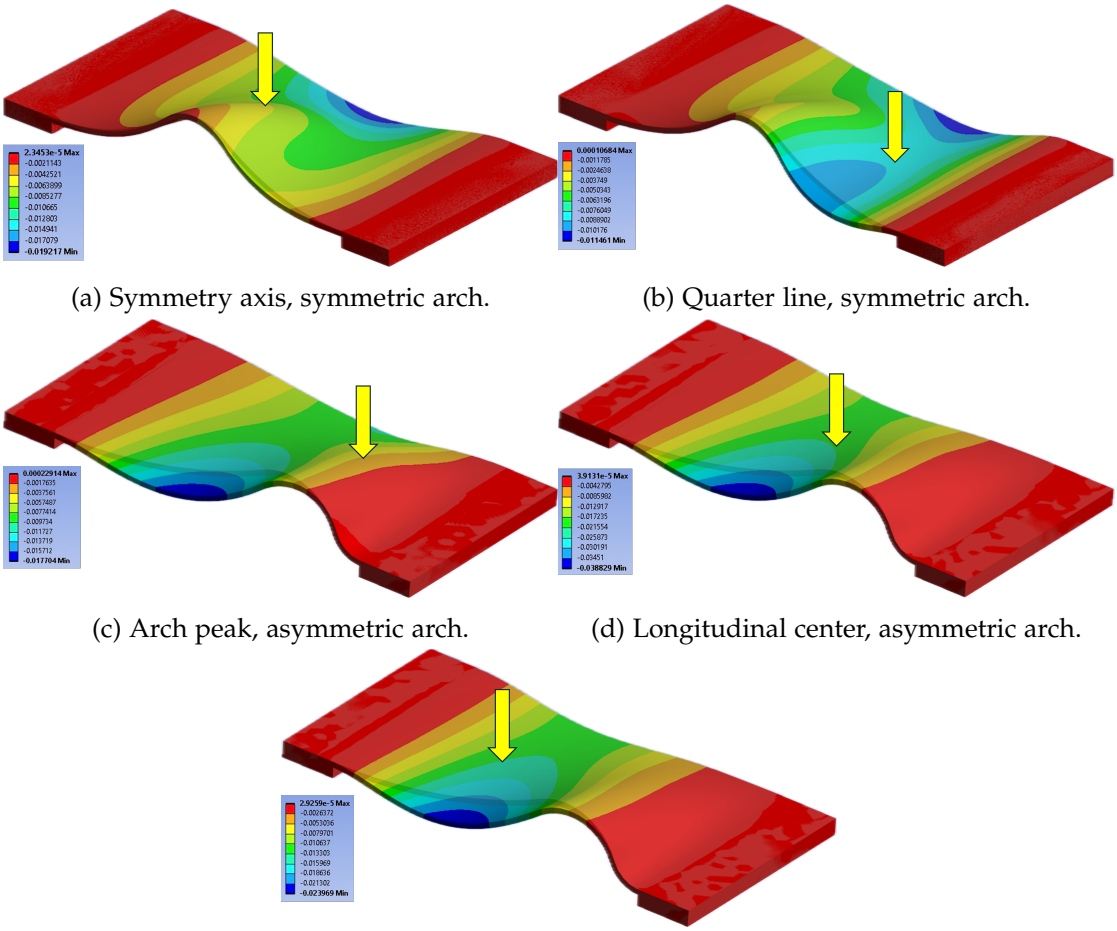

(a) Symmetry axis, symmetric arch.

(b) Quarter line, symmetric arch.

(c) Arch peak, asymmetric arch.

(d) Longitudinal center, asymmetric arch.

(e) Quarter line, asymmetric arch.

Figure 6.4.: Vertical displacement results from point compression FEM simulations on the arched plate foot design with heel and toe contacts. Loads are applied on the center region for all the load cases.

6.3.3. ZwickRoell Testing

The designs are 3D printed using PLA. Compression testing is carried out on the two designs to verify the FEM simulations. The test protocol is similar to the ZwickRoell test in the tech enabler phase to calculate the spring stiffness.

Results

Vertical compression loads of 20–30 N are applied at three points along the foot's length to induce deformation without causing collisions. These loads are similar to those used in the ZwickRoell tests on the tech enabler plate. The resulting stiffness values are shown in Table 6.3, and their magnitudes are color-coded over the arched surface in Figure 6.5.

ZwickRoell Testing on Symmetric Arched Plate Foot, Heel and Toe Contacts			
Longitudinal Position (mm)	**Spring Stiffness (N/mm)**		
	Medial	**Center**	**Lateral**
0	6.59	8.00	5.63
10	6.45	7.89	6.15
20	5.61	8.11	6.90
30	6.59	9.23	8.33
40	8.57	11.76	11.11
50	12.50	16.67	19.05
60	21.43	33.33	40.00

Table 6.3.: Calculated spring stiffness from the ZwickRoell compression testing of the symmetric arched plate foot with heel and toe contacts. Darker shades represent higher stiffness. The arch peak axis is the zero longitudinal position reference. Measurements are only taken on one half of the arch surface due to symmetry. No measurements are taken for surfaces on the heel and toe contacts.

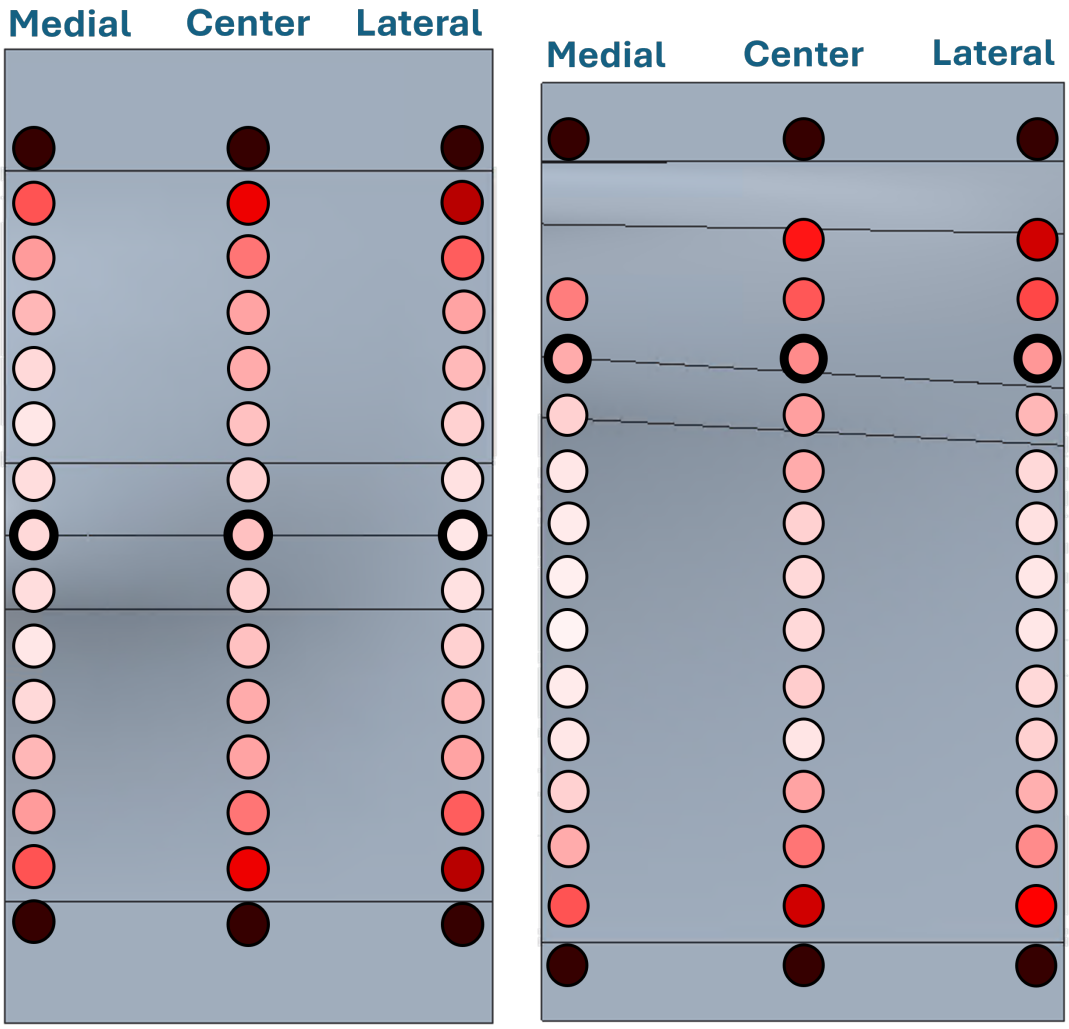

(a) Symmetric arched plate foot.

(b) Asymmetric arched plate foot.

Figure 6.5.: Spring stiffness distribution of arched plate foot designs based on Zwick-Roell compression test. Darker shades represent high stiffness. Points on the lateral side are considered to be rigid due to lack of vertical displacement during testing. The points with dark outlines are located on the arch peak. These points represent the zero reference for the longitudinal positions.

ZwickRoell Testing on Asymmetric Arched Plate Foot, Heel and Toe Contacts			
Longitudinal Position (mm)	**Spring Stiffness (N/mm)**		
	Medial	**Center**	**Lateral**
-20	-	28.57	37.50
-10	14.29	17.39	21.43
0	10.00	13.33	11.54
10	7.41	10.53	8.33
20	5.66	8.70	6.82
30	5.04	7.55	5.88
40	4.88	6.67	5.77
50	4.65	6.82	5.56
60	5.00	7.14	6.52
70	5.63	5.36	7.50
80	7.14	11.11	9.38
90	10.00	16.67	13.64
100	20.00	37.50	30.00

Table 6.4.: Calculated spring stiffness from ZwickRoell compression testing of the asymmetric arched plate foot with heel and toe contacts. Darker shades represent high stiffness. The arch peak axis is the zero longitudinal position reference. Measurements are only taken on one half of the arch surface due to symmetry. No measurements are taken for surfaces on the heel and toe contacts.

Discussion

The ZwickRoell test validates the FEM results, confirming the non-rigid lateral side behavior, which is against the requirement. This arises because the arch geometry is elevated by the heel and toe contact areas, leaving the lateral region unsupported by the ground, contrasting expected high lateral stiffness found in literature [5] and tech

enabler findings.

The Spearman rank correlation coefficient ρ quantifies the association between the foot's three regions (medial, center, lateral) and their spring stiffness [58], treating the foot region as an ordinal variable ranked 1 to 3 in order of their stiffness levels [59]. ρ and p-value are shown in Equations 6.1 and 6.2. $\sigma_{R_{\text{Stiffness}}}$ and $\sigma_{R_{\text{Region}}}$ are the standard deviations of the spring stiffness and foot region ranks respectively. $\text{cov}(R_{\text{Stiffness}}, R_{\text{Region}})$ is the covariance of the two variables.

$$\rho = \frac{\text{cov}(R_{\text{Stiffness}}, R_{\text{Region}})}{\sigma_{R_{\text{Stiffness}}} \sigma_{R_{\text{Region}}}} \approx 0.13 \tag{6.1}$$

$$p \approx 0.59 \tag{6.2}$$

The ρ value of 0.13 indicates a weak positive correlation [60], and the p-value above 0.05 shows insufficient evidence to confirm a statistically significant correlation [61]. This implies the design does not generate meaningful stiffness differences between the regions.

The observed excessive lateral displacement undermines the significance and correlation findings. The design must improve to reproduce the high lateral stiffness required, consistent with desired boundary conditions and prior observations.

6.4. Arched Plate with Heel, Toe, and Lateral Contact Surfaces

6.4.1. Design Approach

An additional lateral contact surface is incorporated into the previous designs to allow for ground contact support on the lateral region (see Figure 6.6). This increases its rigidity and better resembles the boundary condition of the real human foot. The heel, toe, and lateral contact surfaces are on the same level to mitigate lateral-region vertical displacement.

6.4.2. FEM Simulation

Point compression FEM simulations are conducted on the arched plate foot designs, applying fixed support constraints on the heel, toe, and lateral ground contact surfaces. Loads are applied medially and laterally at the symmetry axis and quarter line for the symmetric arch, and at the arch peak axis, longitudinal center, and quarter line for the asymmetric arch. The resulting vertical displacement distributions are shown in Figure 6.7 and Appendix A.

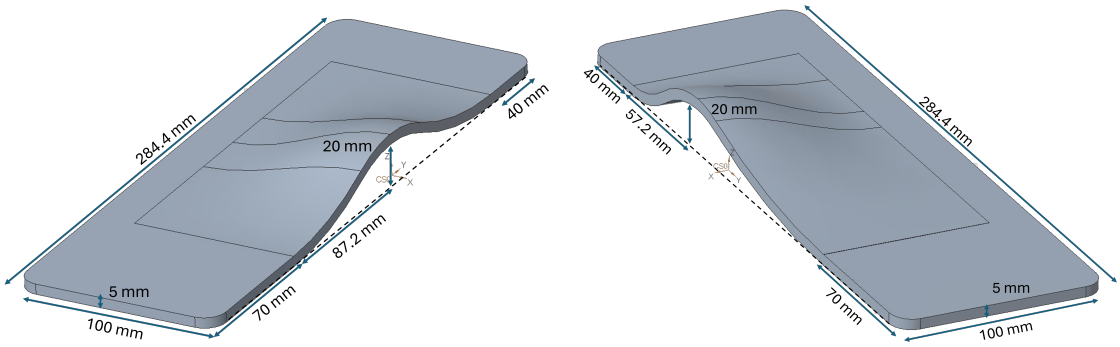

(a) Symmetric arch.

(b) Asymmetric arch.

Figure 6.6.: CAD models of the arched plate foot design with heel, toe, and lateral contact surfaces.

Results

The arch properties in the foot designs show behavior similar to the tech enabler observations. Displacement patterns correspond to applied load cases on both symmetric and asymmetric arch geometries. The heel, toe, and lateral regions exhibit expected rigidity, confirming the stiffness distribution follows previous findings.

Discussion

The vertical displacement distribution shows the required behavior due to the addition of the lateral contact surface. The point compression does not produce any vertical displacement on the lateral side, demonstrating the desired boundary condition of a stiff lateral region. This displacement distribution replicates the behavior observed in the tech enabler. The high displacements at the inflection points act as contraflexures, consistent with beam theory [44]. This confirms that the intended arched plate properties are preserved in this foot design.

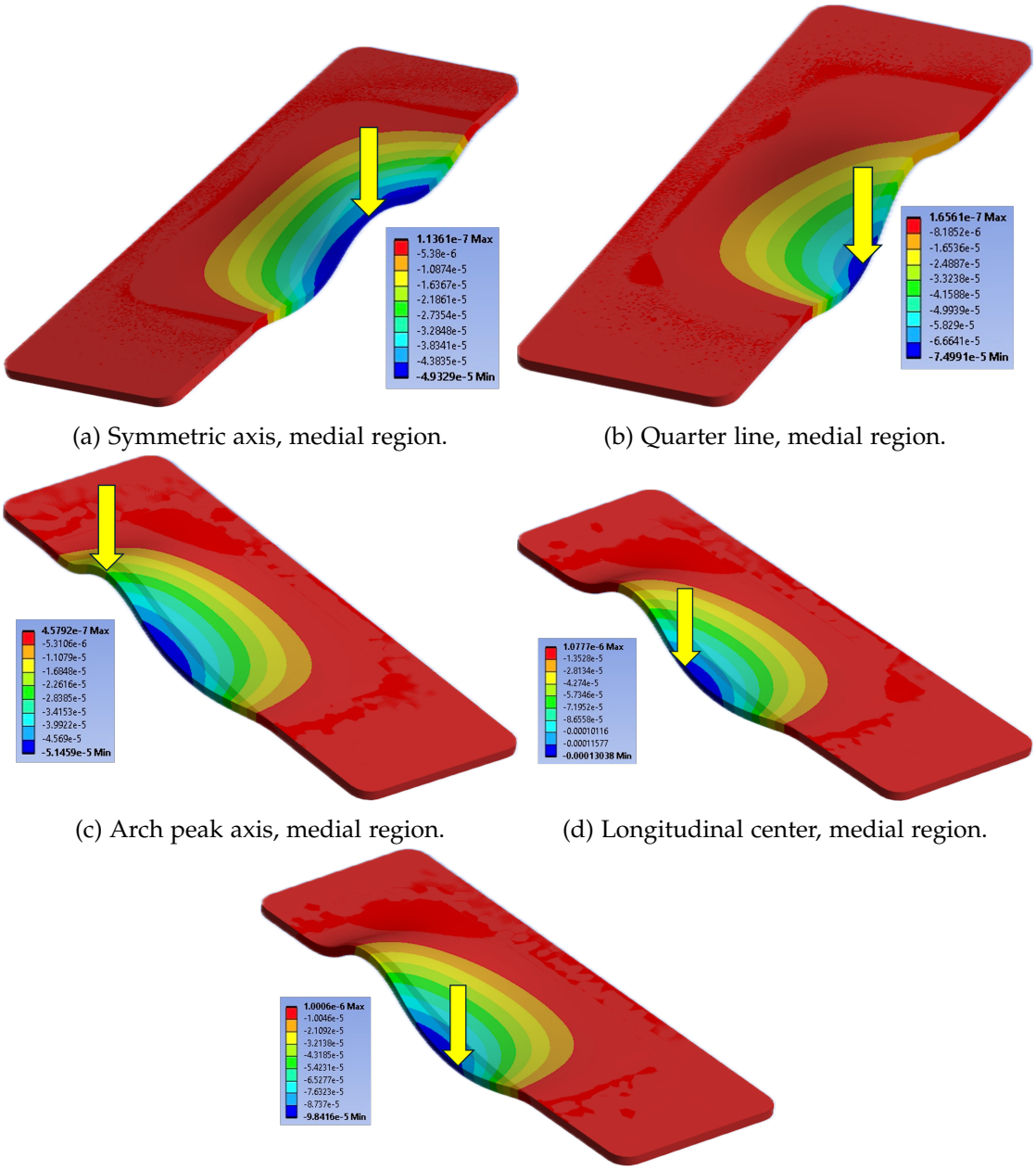

(a) Symmetric axis, medial region.

(b) Quarter line, medial region.

(c) Arch peak axis, medial region.

(d) Longitudinal center, medial region.

(e) Quarter line, medial region.

Figure 6.7.: Selected vertical displacement results from point compression FEM simulations on the arched plate foot designs with heel, toe, and lateral contacts.

6.4.3. ZwickRoell Testing

The main goal of this ZwickRoell test is to verify the lateral region's stiffness after the design modification. Compression tests are performed specifically along the lateral region of the 3D-printed foot designs. Comprehensive testing over the entire arch surface is unnecessary, as the medial and center regions remain unchanged and have already been tested during the tech enabler phase. This test uses a protocol similar to the previous phase to calculate the spring stiffness.

Results

The displacement results of the lateral region are displayed in Table 6.5. The measurements are combined with the data from the tech enabler for completion. The stiffness distribution are visualized in color over the arched surface in Figure 6.8.

Discussion

This phase shows the potential in developing a 3D structurally-elastic bioinspired humanoid foot design for elastic and rigid contact behaviors. The higher and lower stiffnesses in the lateral and medial regions respectively are exhibited. The boundary conditions between the foot and ground are influential in achieving this property. They must be fully considered in the next development phases. Stronger and stiffer materials must be utilized for the final design to make it suitable for humanoid robot applications.

The rapid prototyping foot phase aims to quickly iterate designs incorporating tech enabler learnings into a foot-like structure. These designs focus on analyzing arch geometry's influence on foot stiffness, isolating heel damping and toe joint rotation effects.

A rectangular flat plate foot with an arched sole, based on TORO's current foot dimensions, isolates heel damping and toe joint rotation but shows high stiffness throughout due to large thickness variation. The arched plate foot with heel and toe contacts addresses this but exhibits low lateral stiffness, failing desired boundary conditions. Adding lateral contact surfaces provides ground support, resembling boundary conditions better and exhibiting distinct stiffnesses observed in the tech enabler while isolating heel and toe effects, thus satisfying requirements.

This phase shows the potential in developing a 3D structurally-elastic bioinspired humanoid foot with differentiated medial and lateral stiffnesses. Proper boundary conditions between foot and ground are crucial and must be fully considered in future phases. Final designs require stronger, stiffer materials suitable for humanoid robot applications.

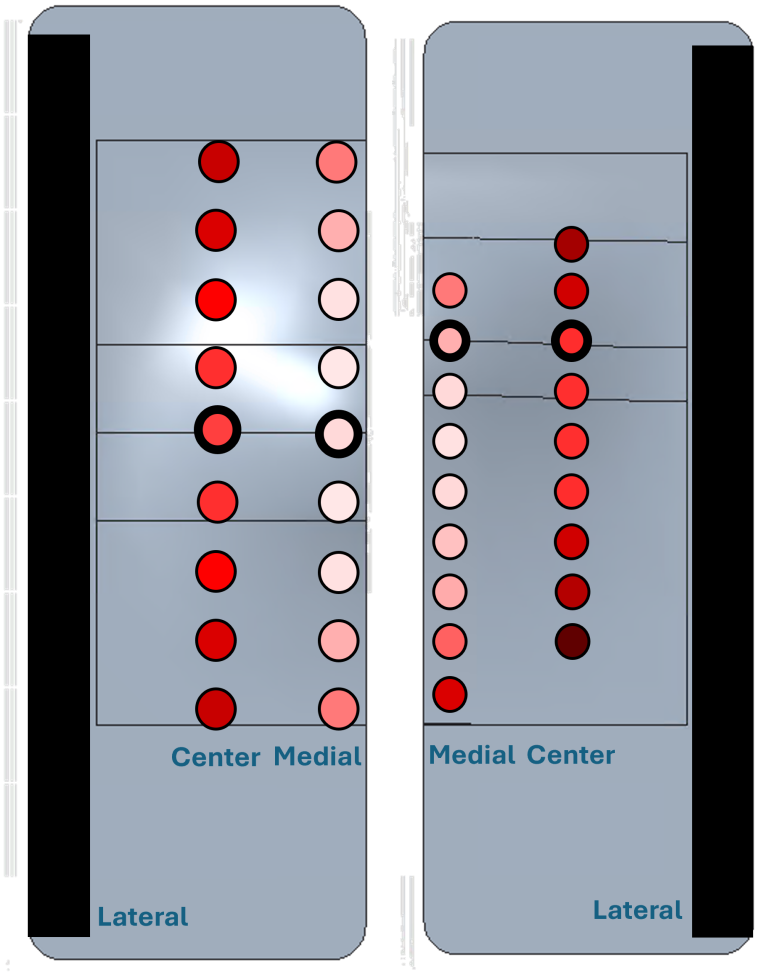

(a) Symmetric arch. (b) Asymmetric arch.

Figure 6.8.: Spring stiffness distribution of arched plate foot designs with heel, toe, and lateral contact surfaces based on ZwickRoell compression test. Darker shades of red signify higher stiffness magnitudes. Points on the lateral side are considered to be rigid due to lack of vertical displacement during testing. The points with dark outlines are located on the arch peak. These points will represent the zero reference for the longitudinal positions.

ZwickRoell Testing on the Lateral Region		
Longitudinal Position (mm)	**Spring Stiffness (N/mm)**	
	Symmetric	**Asymmetric**
-20	-	250.00
-10	-	200.00
0	166.67	166.67
10	200.00	166.67
20	200.00	200.00
30	250.00	200.00
40	250.00	250.00
50	-	250.00
60	-	250.00
70	-	250.00

Table 6.5.: Calculated spring stiffness from ZwickRoell compression testing of the lateral region of the arched plate foot with heel, toe, and lateral contact surfaces. Darker shades represent high stiffness. The arch peak axis is the zero longitudinal position reference. Positions without values indicate omission due to symmetry (symmetric arch) or adverse testing positions (asymmetric arch).

7. Elastic Humanoid Robot Foot

7.1. Motivation

This phase focuses on designing a 3D structurally-elastic bioinspired humanoid robot foot by applying insights from previous technology and prototyping phases. The design must meet the dimensional and load requirements specific to humanoid robot feet.

7.2. Design Approach

7.2.1. Overall Design

Design Requirements

Before designing the elastic foot for the humanoid robot TORO, key requirements must be defined. The foot must bear TORO's 76 kg weight under compression and bending during walking. It should have a modular joint attachment compatible with TORO. The design must allow modularity of the implemented stiffnesses in three foot regions to enable elastic and rigid contact behaviors. Heel damping and toe joints must be excluded to prevent confounding effects and ensure energy storage in the structure. The design should allow quick, accessible manufacturing. It must also incorporate relevant human foot biomechanical characteristics.

Foot Dimensions

The humanoid robot TORO's height (1740 mm) and weight (76 kg) guide the foot's bioinspired design. Correlation studies relating human body height to foot length are used here as a basis [62]. Equation 7.1 correlates these two parameters for TORO.

$$\text{Foot Length (mm)} = \frac{\text{Height (mm)} - 1285\ \text{mm}}{1.6} = \frac{1740\ \text{mm} - 1285\ \text{mm}}{1.6} = 284.4\ \text{mm} \tag{7.1}$$

The foot length dimensioned according to TORO's height is 284.4 mm. Further sources are also used as reference to obtain a general range of values for foot width [63],

toe length [64], heel length [65], and ankle height [66] to guide the design choices. After consulting a variety of literature around physiology and biomechanics, the guiding dimensions for the elastic foot design are outlined in Table 7.1.

Elastic Foot Dimensions	Measurement
Foot Length	284.4 mm
Foot Width	90 mm
Foot Height	50 mm
Toe Length	30 mm
Heel Length	60 mm

Table 7.1.: Guiding dimensions for the elastic foot design. Selected values are within the measurement ranges of each individual dimension of the average human male foot from studies published in literature [62][63][64][65][66].

Design and Material Selection

Key factors for the foot's design and material selection include supporting TORO's weight, energy storage, and ease of manufacturing. Options to examine include steel springs and dampers, polymer injection molding, and composite designs.

Steel springs and dampers provide known stiffness and damping but lack novelty since many humanoid feet use them [35][67][68]. They also fail to deliver inherent structural elasticity because stiffness comes from external parts, not the foot itself. An example is shown in Figure 7.1.

Polymer injection molding concept involves creating a foot-like mold geometry. Polymers with varying stiffness (low for thermoplastics and high for thermosets) are injected into specific mold regions. This method allows different stiffness levels to be built directly into the foot design (see Figure 7.2). However, it is unsuitable for low-volume production due to the custom mold and specialized machinery needed [69]. Additionally, the interaction of the two polymers complicates stiffness prediction for validation of differentiated properties.

The composite design approach holds strong potential for achieving the foot's 3D structural elasticity. Carbon-fiber-reinforced polymers (CFRP) offer high strength and stiffness while remaining lightweight [70]. Their properties can be tailored by adjusting material choice and laminate thickness [71]. This method supports the goal of storing energy inherently within the foot structure and is therefore selected.

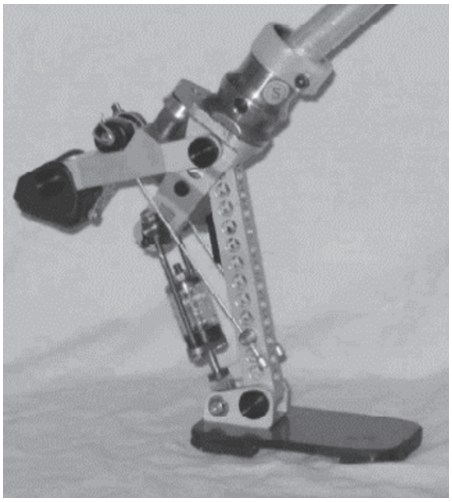

Figure 7.1.: The HEELfoot. Passive prosthetic foot that incorporates steel springs to imitate the plantar fascia to allow for plantar flexion [35].

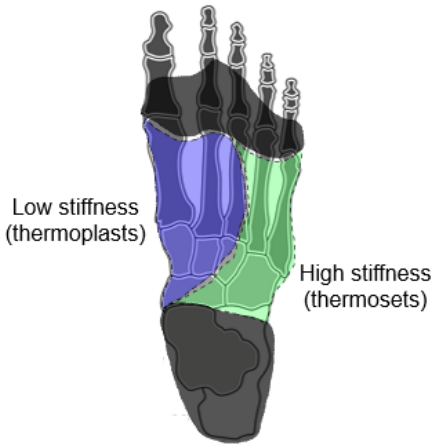

(a) Multi-step injection molding.

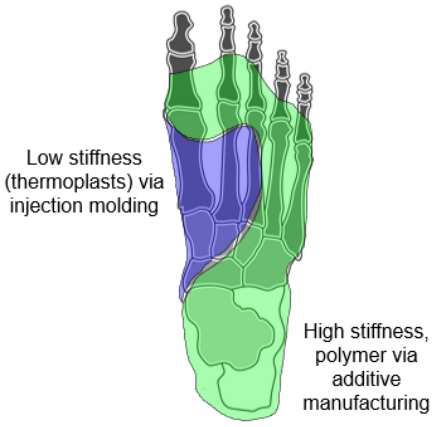

(b) Additive manufacturing + injection molding.

Figure 7.2.: Elastic foot concepts with polymer injection molding overlayed on human foot sketches. Black regions indicate non-polymer areas at the ball and heel. Figure 7.2a illustrates a multi-step injection molding process with two separate injections of low-stiffness polymer on the medial side and high-stiffness polymer on the lateral side. Figure 7.2b depicts using additive manufacturing to make a high-stiffness polymer mold on the lateral side and injection molding low-stiffness polymer on the medial side.

Composite Design Approach

Classical laminate theory is used to design composite laminates, enabling the prediction of their mechanical behavior [72]. Tools like eLamX^2 [73] simulate various fiber-matrix combinations and fiber orientations to test stiffness and strength. However, classical laminate theory is not refined for 3D non-linear, non-laminate structures [73], and bending stiffness simulations rely on strict assumptions that the foot structure does not fully meet [74].

Integrated composite design tools such as Creo Composite Part Design allow draping simulations to predict shear deformation and fiber orientation changes in 3D laminates [75], improving upon eLamX^2. Yet, these complex shapes cause nonlinear bending stiffness distribution influenced by variables like curvature, laminate thickness, and fiber orientation [44][71]. This complexity hinders analytical stiffness definition and modularity of regional stiffnesses with it being determined by a singular structure.

Designing bespoke composite beams shows promise for achieving the foot's 3D structural elasticity with modularity. Beam thickness can adjust bending stiffness [39], overcoming multivariable property issues. A three-beam assembly enables modular stiffness variation across foot regions, integrating the forefoot toe surface and housed in a solid heel complex (see Figure 7.3). This approach is therefore selected.

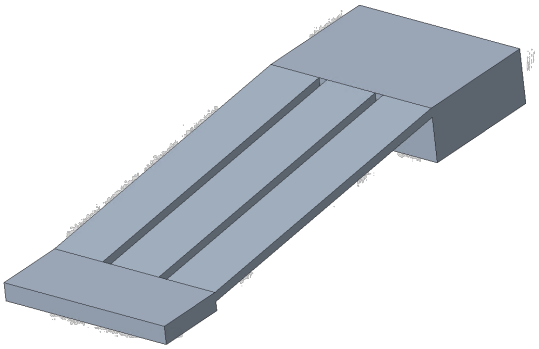

Figure 7.3.: Chosen elastic foot design concept with three carbon fiber beams of different stiffnesses. The beams are attached to a heel structure in the hindfoot region.

Carbon-fiber-reinforced polymer (CFRP) is selected for the composite beams due to its high strength and stiffness while remaining lightweight [70], meeting the design requirements. It is also compatible with many manufacturing processes, making it a versatile material choice.

7.2.2. Carbon Fiber Beams

Beam Geometry

Returning to a discrete geometry has key advantages over the continuous design. Beam structures allow use of the analytical bending equation for simple composite laminates under cantilever bending [39], which is difficult for arched plates. Since composites are orthotropic, fibers can be aligned with expected loads [76]. This ensures predictable, controllable behavior—unlike the complexity of an arched plate.

While a straight beam does not fully replicate the rigid lateral ground contact of a human foot, its stiffness can be adjusted by changing cross-section thickness [39]. This permits designing a softer medial beam and a notably stiffer lateral bar, reflecting human foot lateral rigidity.

Beam Design Concept

Three design concepts with three beams to represent the main foot regions are examined. The first concept (Figure 7.4) features arched beams with the same cross-section but different arch heights, clamped beneath the heel complex. This design resembles the human foot's geometry and controls stiffness via arch shape, reflecting the core concept studied in the tech enabler phase. However, carbon fiber induces anisotropic behavior due to fiber orientation changes along the arched beam, complicating stiffness predictions under variable loading during mid-stance [77].

The second concept (Figure 7.5) uses straight beams with different stiffnesses clamped below the heel complex. This approach allows defining beam stiffnesses during design to match desired levels. However, since all three beams contact the ground, the design does not fully reproduce the real human foot's boundary conditions. This causes similar stability across all foot regions, preventing evaluation of elastic versus rigid ground contact behavior.

The third concept (Figure 7.6) uses beams with different stiffnesses and a slope in the middle. The sloped region separates two horizontal beam surfaces: the lower serves as the toe-ground contact, and the upper mounts to the heel complex at a set height. This geometry allows the beam to bend as the center of pressure moves forward during mid-stance, producing larger expected deformation than previous concepts that only deflect during heel-off. Though the lateral side lacks ground contact, the lateral beam can be made much stiffer than the medial beam to reflect lateral rigidity. This concept is selected for its functional advantages.

The carbon fiber beam for the selected concept (Figure 7.7) consists of three main regions: the toe, heel, and sloped region. The toe region contacts the ground, while the heel region clamps to the foot's heel structure for mounting. The sloped region connects

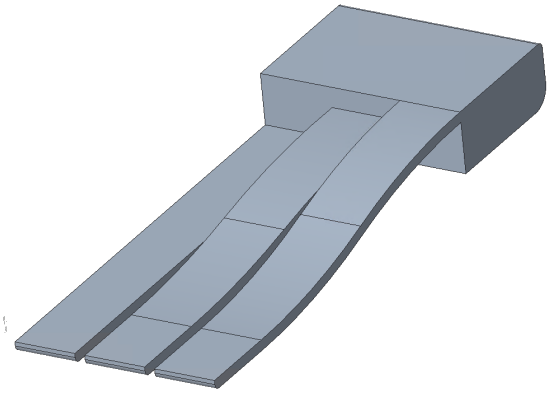

Figure 7.4.: Elastic foot design concept with one straight and two arched carbon fiber beams. The straight beam lay flat on the ground along its length to represent the lateral region. The two arched beams have different arch heights. The beam with the higher arch represents the medial region. They are to attached to the heel structure at different heights.

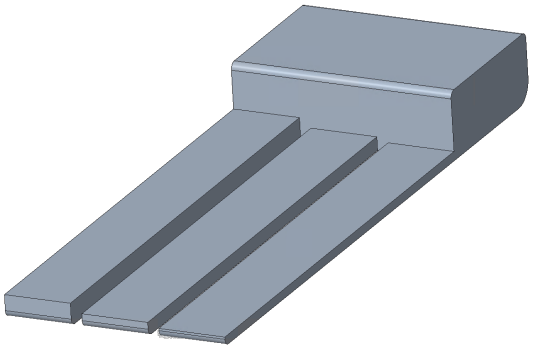

Figure 7.5.: Elastic foot design concept with three straight carbon fiber beams of different stiffnesses. The beams lay flat on the ground along its length. The thickest and thinnest beams represent the lateral and medial sides respectively. They are attached to the bottom side of the heel structure.

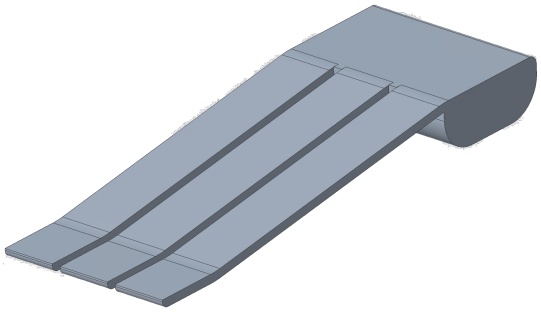

Figure 7.6.: Concept of elastic foot design with three carbon fiber beams of different stiffnesses. The beams are to be attached on the top side of the heel structure in the hindfoot region.

the toe and heel. The beam's thickness h is determined during the dimensioning process to determine the xy-plane stiffness.

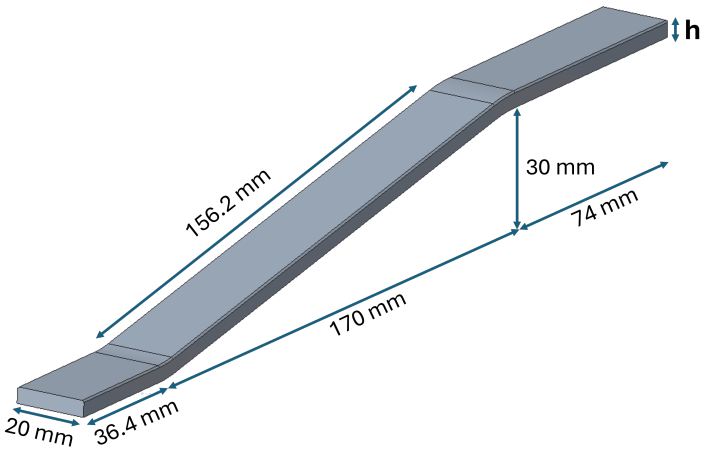

Figure 7.7.: Carbon fiber beam design.

Carbon Fiber Manufacturing

The carbon fiber beam manufacturing method impacts the choice of material properties for dimensioning. Thus, selecting the manufacturing process before production is essential. Two methods examined are hand layup and 3D printing.

Hand layup is performed by manually layering reinforcement materials with its

matrix material in an open mold [78]. The advantages of this method are that it is cost-efficient and can be carried out manually [79]. However, the quality of the final product relies heavily on the skill of the worker. A trial was carried out to manufacture a 4-mm thick beam by mixing glass fiber and epoxy resin and compressing it between the top and bottom molds distanced at 4 mm. The finished part had a thickness of approximately 4.3 mm. This displays the difficulty to achieve the desired thickness with hand layup, which is significant in determining the stiffness of the part.

Hand layup involves manually layering reinforcement and matrix materials in an open mold [78]. Its advantages include low cost and manual operation [79]. However, the final product quality depends heavily on worker skill. A trial to manufacture a 4-mm thick beam using glass fiber and epoxy resin (1276 N/m bending stiffness [80]) showed a finished thickness of about 4.3 mm (see Figure 7.8). This results in a 24.2% deviation from the dimensioned bending stiffness [39], highlighting the critical influence of thickness inaccuracies on the property.

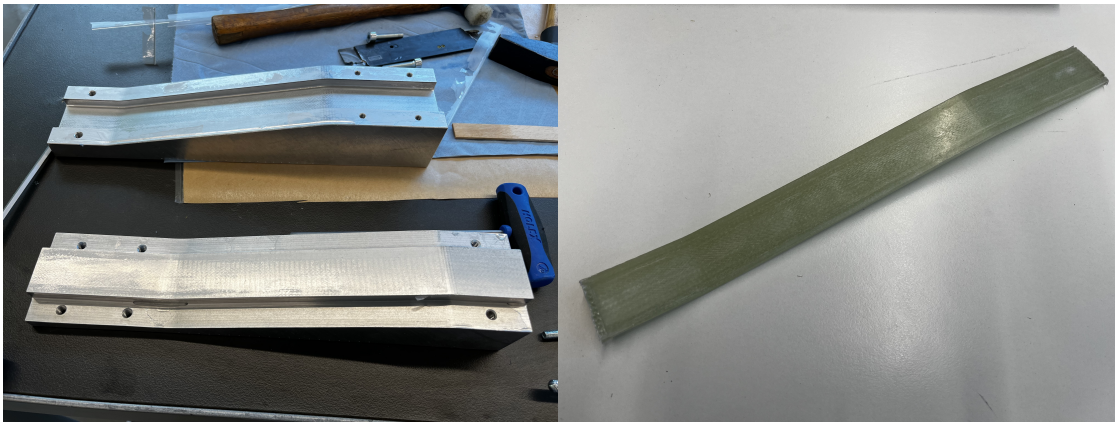

(a) Mold for beam manufacturing. (b) Manufactured glass fiber beam.

Figure 7.8.: Manufacturing of glass fiber beam. Mold is manufactured out of aluminium with the desired geometry of the beam. Degree of compression on the mold determines the achieved vertical thickness of the beam.

Composite 3D printing enables quick manufacturing and on-demand fiber-matrix composite production, offering design flexibility independent of user skill. Markforged X7 uses Continuous Fiber Fabrication (CFF) to produce composite parts [81]. This manufacturing method is selected for the carbon fiber beams.

The beams are made from carbon fiber reinforcement embedded in an Onyx matrix material [82]. Carbon fiber is selected due to its higher strength and stiffness compared to other options like glass fiber and Kevlar. Its mechanical properties are summarized

in Table 7.2. The tensile modulus of the composite is used in the bending stiffness calculations for dimensioning the beams.

Markforged carbon fiber properties (with Onxy matrix)	**Values**
Density	1.4 g/cm^3
Tensile modulus	60 GPa
Tensile strength	800 MPa
Tensile strain at break	1.5%

Table 7.2.: Mechanical properties of Markforged carbon fiber with Onxy matrix [83].

Beam Dimensioning

The beam's critical dimension is its rectangular cross-section. A width of 20 mm is chosen to ensure enough clamping surface and sufficient material between screw holes and edges while minimizing the foot's width. Hence, the cross-section thickness h drives the dimensioning.

The minimum bending stiffness $K_{dim,min}$ is determined using Equation 7.2, which is valid for dimensioning beams under straight cantilever bending. The medial beam, having the lowest bending stiffness, is dimensioned first to ensure safety of the weakest part. The force F on each beam is TORO's weight (745.56 N) divided by three, resulting in 248.52 N. This force is doubled by the safety factor of 2. The maximum displacement δ_{max} is the vertical deflection at the loaded beam end and corresponds biomechanically to the Achilles tendon lengthening after ankle rotation during mid-stance, when the ankle catapult loads [84]. A δ_{max} of 120 mm is selected, consistent with literature ranges [85].

$$K_{dim,min} = \frac{2F}{\delta_{max}} = \frac{2(248.52\text{N})}{120 \times 10^{-3}\text{m}} \approx 4142\,\text{N/m} \tag{7.2}$$

The tensile modulus of the carbon fiber is 60 GPa [83]. The beam's rectangular cross-section has a width of 20 mm. The beam length L, which is the lever arm for the applied force, corresponds to the sloped region length of 104 mm. Using these parameters, the

minimum thickness h_{min} needed to achieve the required bending stiffness of 4142 N/m is calculated with Equation 7.3.

$$h_{min} = \left(\frac{4K_{dim,min}L^3}{Eb}\right)^{\frac{1}{3}} = \left(\frac{4(4142\text{N})(0.174\text{m})^3}{(60\times10^9\text{Pa})(20\times10^{-3}\text{m})}\right)^{\frac{1}{3}} \approx 4.17\,\text{mm} \tag{7.3}$$

The bending stiffness and thickness of the carbon fiber beams are summarized in Table 7.3. The medial beam thickness is set to 4.5 mm, which is the minimum thickness needed for consistent reinforcement fiber infill by the carbon fiber 3D printer as obtained from trials. The lateral beam is designed to have three times the minimum bending stiffness, reflecting the lateral foot's rigid boundary condition. The center beam's stiffness lies between the medial and lateral beams, with corresponding thicknesses specified in the same table.

Carbon Fiber Beam Region	**Thickness (mm)**	**Bending Stiffness (N/m)**
Medial	4.5	5189.33
Center	5.0	7118.42
Lateral	6.0	12301.63

Table 7.3.: Thickness and bending stiffness of the carbon fiber beams.

7.2.3. Heel Complex

The heel complex forms the second key part of the elastic foot design, serving as the modular attachment base for the carbon fiber beams. Made of aluminum, it enables accessible, fast manufacturing while maintaining strength and lightweight. It handles compressive loads safely, eliminates heel damping, and allows bioinspired ankle joint height. This complex is crucial for meeting the foot's biomechanical and validation requirements.

The heel complex consists of the heel block, ankle surface, and adapter plate. The heel block clamps the carbon fiber beams and attaches the ankle component while reproducing human ankle joint offset, with FEM simulations confirming its strength under load. The ankle surface sits atop the heel block and provides a mounting area for the adapter plate, securing assembly through bolt holes. The adapter plate enables

modular connection to a force-torque sensor or foot cup, and bolts from the heel block clamp all components together for a stable structure.

7.2.4. Final Design

The 3D structurally-elastic bioinspired humanoid robot foot assembly is shown in Figure 7.9. It is an assembly of the three carbon fiber beams and the heel complex.

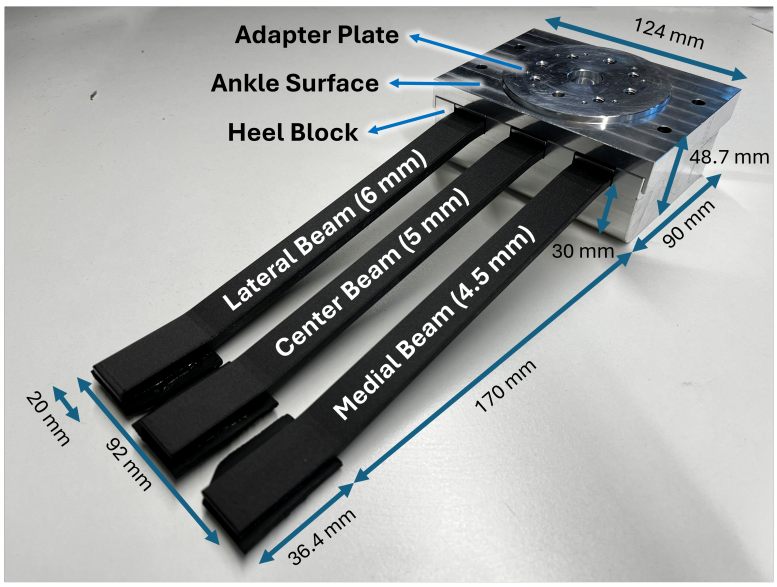

Figure 7.9.: 3D structurally-elastic bioinspired humanoid robot foot.

7.3. Validation

7.3.1. FEM Simulation

FEM simulations are conducted on the dimensioned carbon fiber beams to validate that they meet the required bending stiffness and withstand expected loads. The simulations adapt orthotropic carbon fiber properties from eLamX^2 to the Markforged carbon fiber properties with Onyx matrix, as detailed in Table 7.2. This approach ensures realistic modeling of material behavior for accurate stiffness and strength prediction under load conditions.

Results

The FEM simulation applies a fixed support at the toe joint surface with a 248.52-N vertical load on the clamping surface. This setup simulates ankle forward rotation during mid-stance, causing upward bending of the carbon fiber beam.

The simulation evaluates von Mises stress, vertical displacement, and strain energy distributions to assess structural behavior. These distributions for the medial beam are depicted in Figure 7.10. Maximum values from simulations of all three beams are summarized in Table 7.4.

Carbon Fiber Beam	**Maximum Stress (MPa)**	**Maximum Displacement (mm)**	**Maximum Strain Energy (mJ)**
Medial	767	73	4.1
Center	710	67	2.7
Lateral	543	39	1.5

Table 7.4.: Table summarizing the maximum values for the von Mises stress, vertical displacement, and strain energy for the carbon fiber beams obtained from FEM simulations.

Discussion

The medial beam's maximum von Mises stress is 767 MPa, which is below the composite's yield strength of 800 MPa [83]. This confirms no plastic deformation will occur

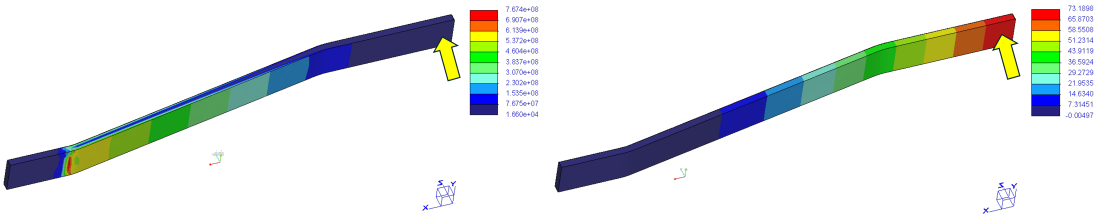

(a) von Mises stress. (b) Vertical displacement.

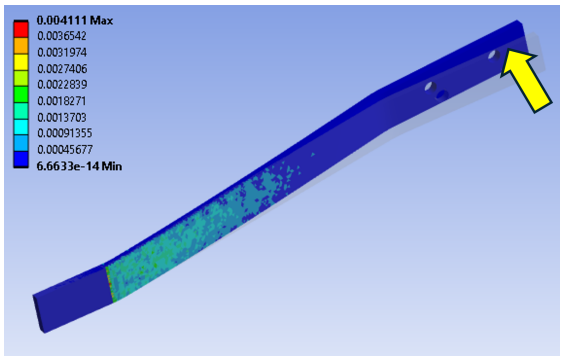

(c) Strain energy.

Figure 7.10.: FEM simulation results on the medial carbon fiber beam.

under the load case. The maximum vertical displacement is 73 mm, less than the allowable 120 mm, confirming structural safety against failure.

From Table 7.4, maximum vertical displacement decreases as beam thickness increases, validating that higher thickness achieves greater bending stiffness. Additionally, maximum strain energy reduces with increasing thickness, showing the lateral beam with higher stiffness stores less strain energy than the medial beam. This supports the design goal of an elastic medial foot region that stores energy within its structure.

7.3.2. ZwickRoell Testing

The ZwickRoell machine is used to perform bending tests on the 3D-printed carbon fiber beams. The aim of this test is to verify whether the manufactured beams achieve the dimensioned bending stiffness.

Results

A downward force of 25 N is applied at the free end of each beam to induce measurable deformation without causing collision with the arched plate. The resulting vertical displacement is recorded during the test. The bending stiffness of each beam is then

calculated as the ratio of the applied vertical load to the measured vertical displacement. The central tendency measures from these test results are summarized in Table 7.5.

Carbon Fiber Beam Bending Stiffness (N/m)			
Measures	**Medial**	**Center**	**Lateral**
Average	**732.18**	**1038.43**	**1388.21**
Median	693.48	1039.51	1358.70
25th Percentile	681.71	1034.13	1338.75
75th Percentile	804.51	1041.67	1464.14
Interquartile Range (IQR)	122.80	7.54	125.39
Lower Limit	497.51	1022.82	1150.67
Upper Limit	988.70	1052.97	1652.22

Table 7.5.: Table summarizing the statistical measures of central tendency for the bending stiffness of the carbon fiber beams via ZwickRoell testing.

Carbon Fiber Beam Region and Thickness	**Theoretical Bending Stiffness (N/m)**	**Measured Bending Stiffness (N/m)**
Medial (4.5 mm)	5189.33	732.18
Center (5 mm)	7118.42	1038.43
Lateral (6 mm)	12301.63	1388.21

Table 7.6.: Comparison between theoretical and measured average bending stiffness of the carbon fiber beams.

Discussion

Bending Stiffness The ZwickRoell bending tests showed that the manufactured carbon fiber beams achieved only 11-15% of their theoretical bending stiffness from the

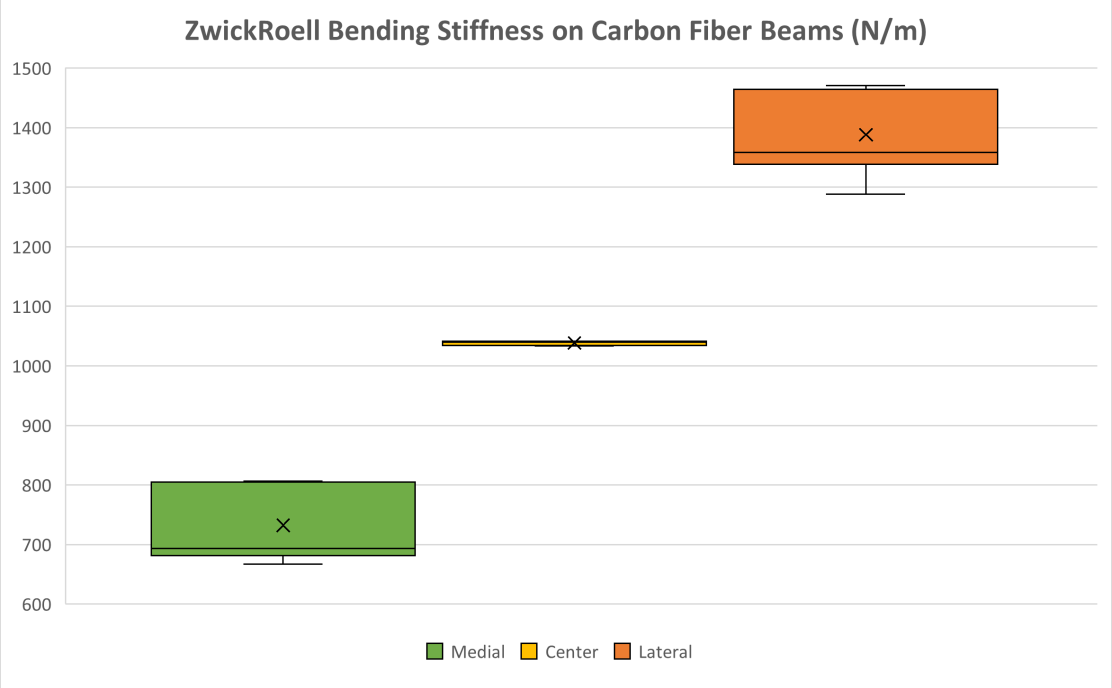

Figure 7.11.: Box plots for the bending stiffness measurements of the three carbon fiber beams. The cross mark represents the average value. The colored box represents values within the interquartile range. The horizontal line in the box represents the median value. The top and bottom horizontal lines represent the upper and lower value limits respectively.

design. Several factors contribute to this gap. The analytical bending equations assume small deflections, uniform straight beams, and plane sections remaining plane, which are not fully met [86]. Stress concentrations at cross-section changes and milled bolt holes weaken structural integrity [87]. The Continuous Fiber Fabrication technology is not yet fully mature [88], leading to defects such as fiber misalignment, damage, and porosity, further reducing effective stiffness [89].

The carbon fiber infill is altered as an attempt to address the issue. The isotropic fiber orientation is implemented to optimize the mechanical properties in the xy-plane [90], which is the desired in this case. However, it did exhibit any bending stiffness enhancement.

Box Plots Despite the low magnitudes, the box plots demonstrate sufficient stiffness differences between medial, center, and lateral regions from the measurements, maintaining biomechanical function. The center beam showed moderate average stiffness values between the medial and lateral beams. The median values of each variable are not within the IQRs of other variables, signifying significant bending stiffness differences for the three beams [91].The center beam IQR was about 6% of medial and lateral beams, with data variance attributed to the inherent variability of the 3D printing process and its defects [88]. Thus, although bending stiffness values are lower than theoretical, the design goals of varying regional stiffnesses within the foot are successfully met.

Spearman Rank Correlation Analysis The Spearman rank correlation coefficient ρ quantifies the association between the carbon fiber thickness and their bending stiffness [58]. ρ and p-value for the measurements are shown in Equations 7.4 and 7.5. $\sigma_{R_{\text{Stiffness}}}$ and $\sigma_{R_{\text{Region}}}$ are the standard deviations of the bending stiffness and beam thickness respectively. $\text{cov}(R_{\text{Stiffness}}, R_{\text{Region}})$ is the covariance of the two variables.

$$\rho = \frac{\text{cov}(R_{\text{Stiffness}}, R_{\text{Region}})}{\sigma_{R_{\text{Stiffness}}}\, \sigma_{R_{\text{Region}}}} \approx 0.94 \tag{7.4}$$

$$p \approx 0 \tag{7.5}$$

The dynamic test yields a ρ value of 0.94. This is a positive value lying within 0.70-1.00. This shows a very strong correlation between the beam thickness and the bending stiffness [60]. The positive value indicates that the bending stiffness increases with increasing beam thickness, which agrees with the Equation 7.2. The p-value is

below 0.05, indicating that a strong correlation can be determined. Despite the low magnitudes, the beams reliably create a foot design with an elastic medial region and stiff lateral region as intended.

7.4. Intermediate Conclusion

The main goal of this carbon fiber foot phase is to design a 3D structurally elastic, bioinspired humanoid robot foot by incorporating learnings from prior phases and bioinspired features. The design successfully integrates three carbon fiber beams with varied stiffnesses, dimensioned to emulate the medial, center, and lateral foot regions. These beams attach to a bioinspired aluminum heel complex that eliminates heel damping, isolating the beams' elastic behavior.

FEM simulations confirm structural capability under expected loads, with strain energy concentrated more in the medial beam, validating the intended elastic-rigid foot behavior. Although ZwickRoell tests show the manufactured beams achieved only 11-15% of their designed bending stiffness due to dimensioning assumptions and manufacturing variability, a strong positive correlation (ρ=0.94, p=0) between beam thickness and bending stiffness remains.

Thus, the goal of a 3D structurally-elastic bioinspired humanoid robot foot with differentiated stiffnesses in the three region is achieved. The design preserves the stiffness scale across beams supporting elastic and rigid contact behaviors, though future phases should consider a reduced body weight (588.6 N or 60 kg) to avoid plastic deformation and failure.

8. Shank Assembly

8.1. Motivation

This design phase involves the assembly of a shank structure onto the elastic foot to verify the 3D structurally-elastic humanoid robot foot's rigid and elastic contact behavior. It validates this by simulating the mid-stance phase through dynamic testing on a test bench.

8.2. Design Approach

8.2.1. Shank Assembly

Design Requirements

The shank design is guided by several mechanical and bioinspired requirements. It must be modular to be attached to the foot and support body weight. It needs strength to resist buckling from TORO's 76 kg mass and bending from forward forces. Its size and mechanisms follow bioinspired principles for realistic function.

Shank Concept

The shank uses an aluminium profile, chosen for its modularity, strength, light weight, and easy customization to various lengths and load cases. It attaches to the elastic foot via the adapter plate. A fixed joint allows the heel to rotate forward with the shank bending, storing strain energy in carbon fiber beams. This reproduces the ankle catapult generated by the Achilles tendon extension [84]. The shank length follows bioinspired data, set at 450 mm within the typical adult male range of 410–490 mm [92]. Mid-stance simulation with this shank concept is sketched in Figure 8.1.

Force Calculation for Center of Pressure Trajectory Generation

A forward force is applied on the shank to shift the center of pressure forward on the foot. Although mid-stance typically shifts forward by 100-120 mm [19], a maximum

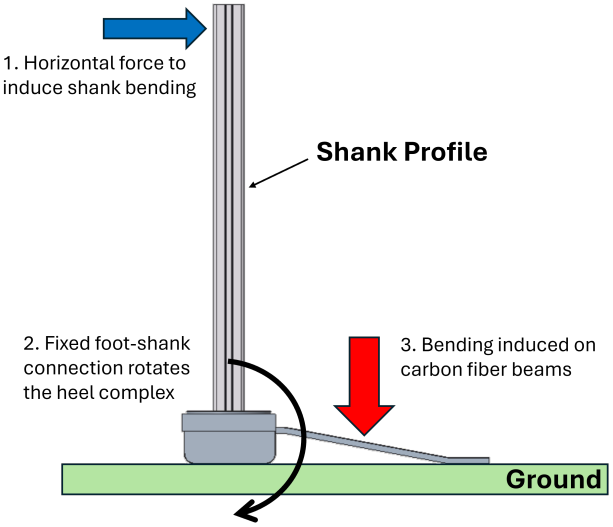

Figure 8.1.: Mid-stance simulation on the elastic foot utilizing the shank profile concept.

shift to the toe at 256.4 mm is used for dimensioning the bending of the aluminium profile.

A 2D trigonometric analysis calculates the required horizontal force on the shank (see Figure 8.2). The foot-shank interface to the front of the foot measures 254.6 mm horizontally, and the vertical length (adapter plate height plus shank length) is 498.7 mm. The force ratio follows these trigonometric lengths, enabling computation of the horizontal force [93].

The horizontal force needed at the shank height to shift the center of pressure to the toe is 302.5 N. This force serves as the basis for bending dimensioning of the aluminium profile.

Aluminium Profile Dimensioning

The aluminium profile cross-section is limited by the adapter plate's mounting space. The largest profile that fits with room for mounting fasteners is 30x30 mm. This profile must be verified to withstand the expected horizontal and vertical loads needed to produce the center of pressure trajectory.

Buckling Analysis The buckling strength of the profile under vertical loads is evaluated using Euler's buckling equation. This equation calculates the critical load P_{cr}

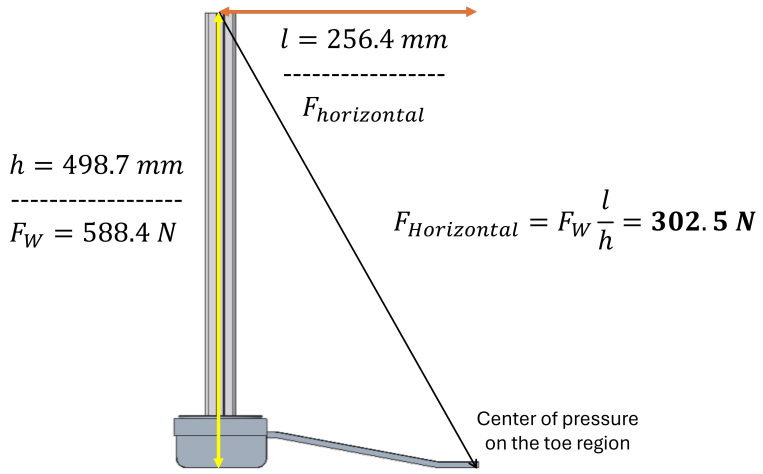

Figure 8.2.: Trigonometric analysis for the calculation of horizontal force on the shank.

the beam can sustain before buckling. The required parameters for this analysis are summarized in Table 8.1. The critical load is calculated using Equation 8.1.

Parameter for Euler Buckling Equation	**Value**
Young's Modulus E	70 GPa
Second Moment of Area I	29000 mm^4 [94]
Unsupported Length L	450 mm
Effective Length Factor K	2

Table 8.1.: Parameters for Euler buckling analysis of aluminium profile. The light variant of an aluminium item Profile 6 30x30 is used. The unsupported length L refers to the shank length. The effective length factor K corresponds to the free-fixed boundary conditions of the profile.

$$P_{\text{cr}} = \frac{\pi^2 EI}{(KL)^2} \approx 24.7\ \text{kN} \tag{8.1}$$

The Euler buckling equation yields a critical load of 24.7 kN for the aluminium

profile. This value exceeds the vertical weight load of 588.4 N significantly. Thus, the profile is stable and will not buckle under the applied vertical load.

Bending Strength The bending strength of the profile against the horizontal load is evaluated considering cantilever beam bending. The horizontal force acts 450 mm from the fixed end. Parameters for calculating bending stress are summarized in Table 8.2. The bending stress is calculated using Equation 8.2.

Parameter for Bending Stress Calculation	Value
Horizontal Force F	302.5 N
Lever Arm L	450 mm
Section Modulus W	1940 mm^3 [94]

Table 8.2.: Parameters for bending stress calculation of aluminium profile. The light variant of an aluminium item Profile 6 30x30 is used. The lever arm L refers to the shank length.

$$\sigma = \frac{F\,L}{W} \approx 70.2 \text{ MPa} \tag{8.2}$$

The bending stress calculated by the equation is 70.2 MPa. This is well below the profile's yield stress of 195 MPa [94]. Therefore, the profile can safely resist plastic deformation under the horizontal load.

Bolt Dimensioning

The bolted connection between the shank profile and adapter plate is dimensioned to withstand expected loads. M6 bolts secure the profile on the left, right, and rear surfaces using the available mounting space. The tensile strength of the connection is analyzed by calculating the maximum tensile force on the most loaded bolt at the back. The necessary parameters are summarized in Table 8.3, and the calculation is displayed in Equation 8.3.

$$F = \frac{M}{n\,r} \approx 1.8 \text{ kN} \tag{8.3}$$

Parameter for Maximum Bolt Tensile Force	Value
Bending Moment M	136125 Nmm
Number of Bolts n	3
Bolt Circle Radius r	25 mm

Table 8.3.: Parameters for maximum bolt tensile force calculation.

The maximum tensile force on the most loaded M6 bolt is approximately 1.8 kN. M6 bolts with property class 8.8 have tensile strengths around 16.1 kN [95], far exceeding this load. Therefore, the bolt safely handles the tensile forces from shank bending. The other two bolts carry lower loads and are also sufficiently strong.

Final Assembly

The CAD model of the shank assembly is shown in Figure 8.3. It features the dimensioned aluminium profile attached to the adapter plate using the designed bolted connection. A weight platform is mounted on the shank profile to hold 60 kg, simulating body weight on the elastic foot.

8.2.2. Dynamic Test Bench

The dynamic test bench for mid-stance testing (see Figure 8.4), aims to validate the foot's elastic and rigid contact behaviors. It consists of a force plate, a threaded top link, and a cage. The test applies different center of pressure trajectories to mimic dynamic loading during mid-stance, assessing the performance of the 3D structurally-elastic foot.

The test bench consists of a force plate, a threaded top link, and a cage. The AMTI BMS400600 force plate [96] measures ground reaction forces and center of pressure from the elastic foot under load. A threaded top link (TL4003022GP, Category 2-2, 53-76 cm [97]) applies horizontal force to bend the shank by extending itself via a lead screw from a fixed position. The cage, built from aluminium profiles (item Profile 8 40x40 [98]), forms the main test bench structure to support loads for reliable data collection.

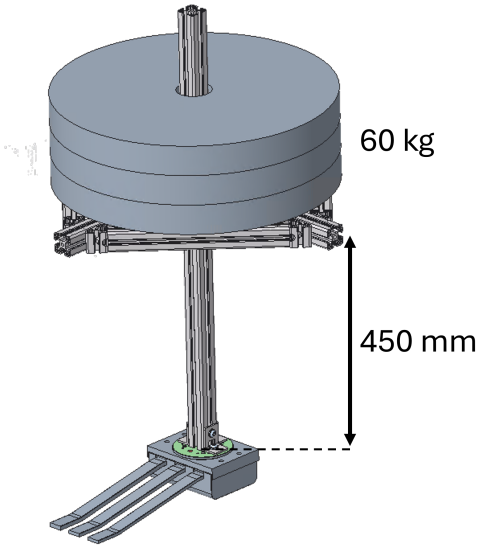

Figure 8.3.: CAD model of the elastic foot design with shank assembly. The shank profile is attached with 60 kg of weight to simulate body weight.

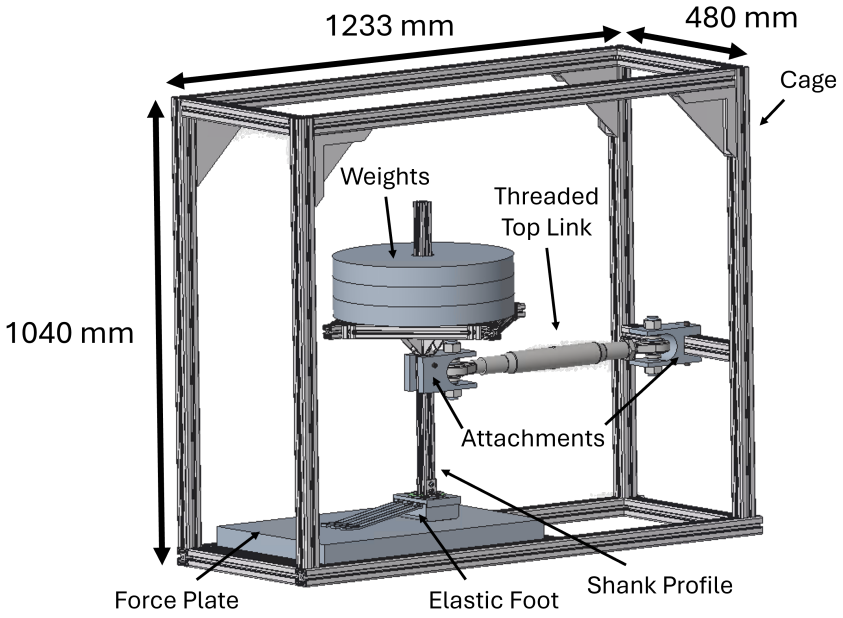

Figure 8.4.: CAD model of the dynamic test bench.

8.3. Validation

8.3.1. Dynamic Testing on Elastic Foot

Dynamic testing of the 3D structurally-elastic foot design is carried out on the dynamic test bench. The test aims to assess how differently the foot absorbs energy depending on the center of pressure trajectory because of its different stiffnesses on the medial, center, and lateral sides.

Test Setup and Protocol

The dynamic testing setup and protocol is outlined in Appendix B. The test involves three independent variables: center of pressure trajectories toward the medial, center, and lateral foot regions. These are controlled by adjusting the fixed end location of the threaded top link. The dependent variable is the slope of the ground reaction force in the foot's longitudinal direction ΔF_y. This slope is the ratio between the change in longitudinal ground reaction force (N) and the rotation of the threaded top link (rad), with units N/rad. This parameter quantifies how much vertical load is converted into longitudinal force by the foot as body weight shifts forward during mid-stance. It reflects the realization of elastic and rigid contact behaviors according to energy storage in the foot structure through bending of the carbon fiber beams.

Results

12 trials are performed for each center of pressure trajectory to establish statistical significance of the longitudinal ground reaction force slope. A Python script [99] processes the data and generates time plots. The realized center of pressure trajectories appear in Figure 8.5. Central tendency measures from test results are summarized in Table 8.4 and visualized as box plots in Figure 8.6.

Discussion

Center of Pressure Trajectory The center of pressure trajectory plots show successful shifts toward the medial, center, and lateral foot regions. A 100 mm shift in the y-direction aligns with mid-stance forward shifts reported in literature [19], confirming the success of the implementation of the independent variables.

The medial trajectory shift is more pronounced than the lateral, with lateral x-direction shift about 50% smaller. This difference stems from lower stiffness in the medial carbon fiber beam, which allows greater bending toward that elastic region. Despite this, shifting the center of pressure laterally remains achievable.

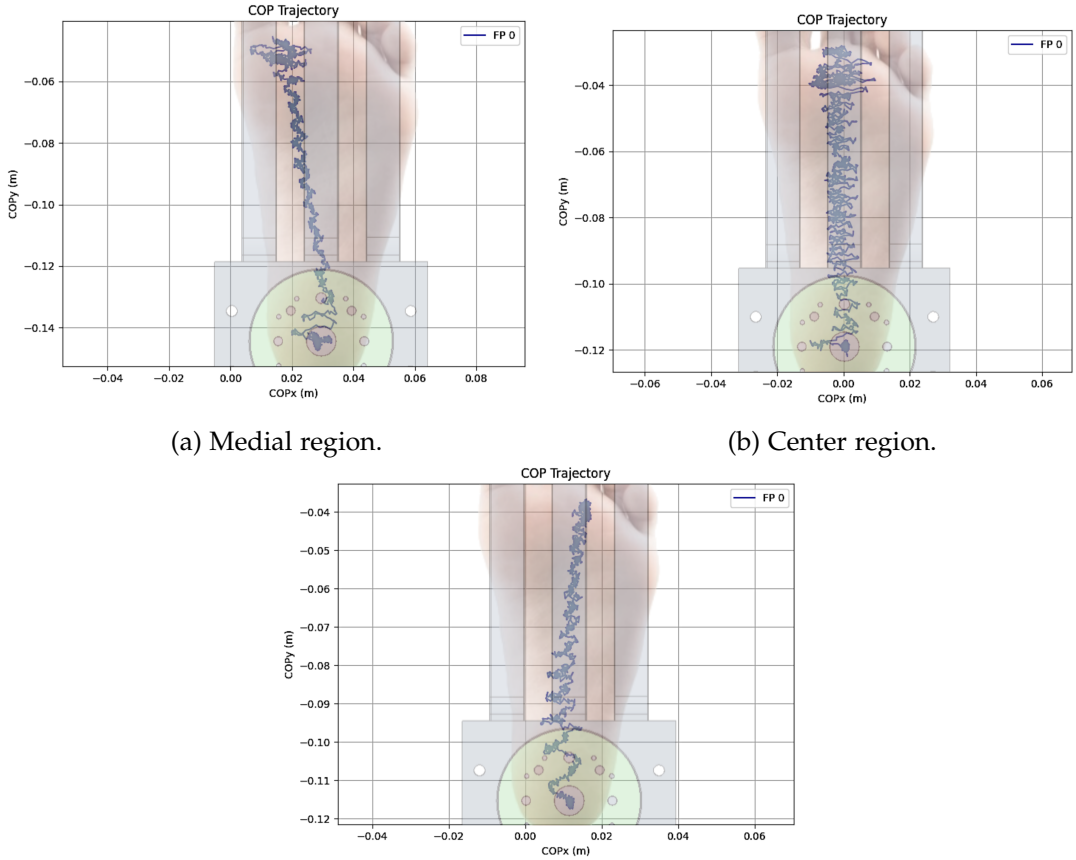

(a) Medial region.

(b) Center region.

(c) Lateral region.

Figure 8.5.: x-y plots of realized center of pressure trajectories from the dynamic test on the elastic foot. Images of the top view of the elastic foot and the bottom view of a human foot [100] are overlayed on the plots for comparative visualization. Forward shifts of 100 mm in the center of pressure are achieved.

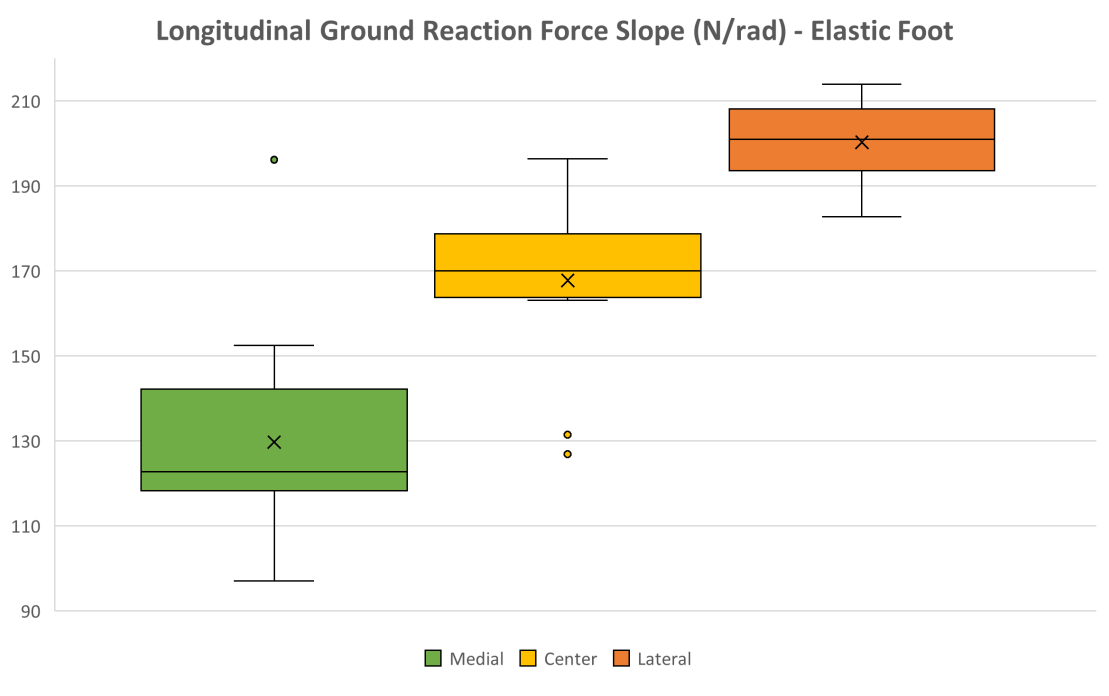

Figure 8.6.: Box plots for the 12 measurements of the longitudinal ground reaction force slope for each center of pressure trajectory on the elastic foot. The cross mark represents the average value. The colored box represents values within the interquartile range. The horizontal line in the box represents the median value. The top and bottom horizontal lines represent the upper and lower value limits respectively. Points outside these limits are outliers.

Longitudinal Ground Reaction Force Slope (N/rad) - Elastic Foot			
Measures	**Medial**	**Center**	**Lateral**
Average	**121.55**	**167.83**	**200.33**
Median	122.82	170.08	201.05
25th Percentile	118.26	163.84	193.68
75th Percentile	142.24	178.75	208.15
Interquartile Range (IQR)	23.98	14.91	14.48
Lower Limit	82.30	141.48	171.96
Upper Limit	178.20	201.10	229.87

Table 8.4.: Table summarizing the statistical measures of central tendency for the longitudinal ground reaction force slope (N/rad) from the dynamic test on the elastic foot.

Box Plots The average longitudinal ground reaction force slope is lowest for the medial and highest for the lateral trajectory. Box plots show median values for each trajectory fall outside the IQRs of others, indicating statistically significant differences [91]. The medial region shows a 63% larger IQR due to the medial beam's lower stiffness and larger elastic energy storage, causing greater force variance.

Spearman Rank Correlation Analysis The Spearman rank correlation coefficient ρ quantifies the association between the foot's three regions (medial, center, lateral) and their longitudinal ground reaction force slopes [58], treating the foot region as an ordinal variable ranked 1 to 3 in order of their stiffness levels [59]. The ranks are paired with the 12 slope measurements. The Spearman rank correlation coefficient ρ and p-value for the dynamic test results is shown in Equation 8.4 and 8.5.

$$\rho = \frac{\operatorname{cov}(R_{\text{Slope}}, R_{\text{Foot Region}})}{\sigma_{R_{\text{Slope}}} \sigma_{R_{\text{Foot Region}}}} \approx 0.84 \tag{8.4}$$

$$p \approx 0 \tag{8.5}$$

The dynamic test produces a correlation coefficient of 0.84, indicating a very strong positive correlation within the range 0.70–1.00 [60]. This positive value means that as the center of pressure moves toward foot regions with higher stiffness, the longitudinal ground reaction force slope increases. The p-value below 0.05 confirms this correlation is statistically significant. These findings demonstrate that by directing the center of pressure trajectory toward areas with varying stiffness, the elastic foot achieves both elastic and rigid contact behaviors. This confirms the successful attainment of the thesis objective.

8.3.2. Dynamic Testing on State-of-the-Art Foot

Dynamic testing is also carried out on the Ottobock 1C63 Triton Low Profile prosthetic foot. The aim of this test is to collect data for comparison between the designed 3D structurally-elastic humanoid robot foot to the state-of-the-art foot design. This provides further validation of the contribution of the findings of this research to the field.

Test Setup and Protocol

The setup and protocol for the dynamic test on the prosthetic foot remains similar (Appendix B). The main difference is that the adapter plate is now attached to the pyramid joint of the prosthetic foot. This reproduces the fixed foot-shank connection from the elastic foot for consistent testing.

Results

10 trials are conducted on the Ottobock prosthetic foot for each trajectory to establish statistical significance of the longitudinal ground reaction force slope. A Python script [99] processes the data and generates time plots. The realized center of pressure trajectories are shown in Figure 8.7. A comparison of the longitudinal center of pressure positions between the elastic foot and the prosthetic foot is presented in Figure 8.8. Central tendency measures from the tests are summarized in Table 8.5 and visualized as box plots in Figure 8.9.

Discussion

Center of Pressure Trajectory The dynamic test on the Ottobock prosthetic foot reveals no clear center of pressure trajectory toward the three foot regions. The foot tends to direct the center of pressure toward the center region due to its rigid sole

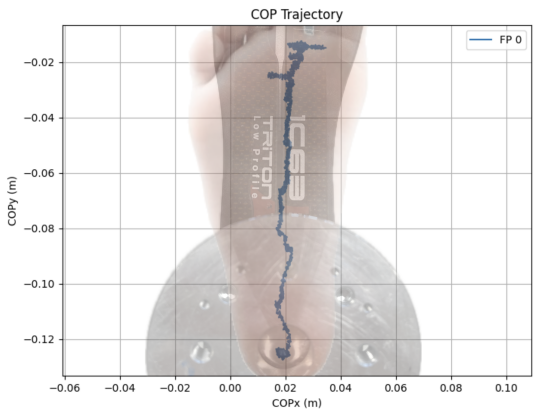

(a) Medial region.

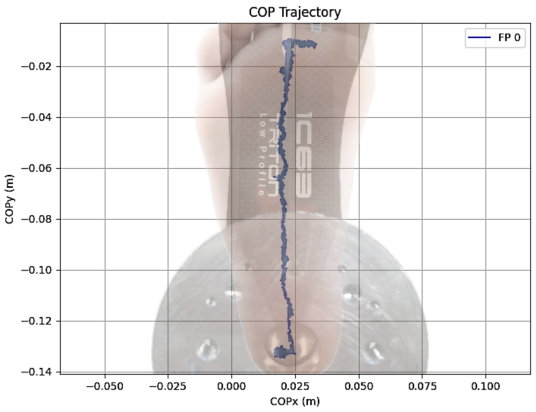

(b) Center region.

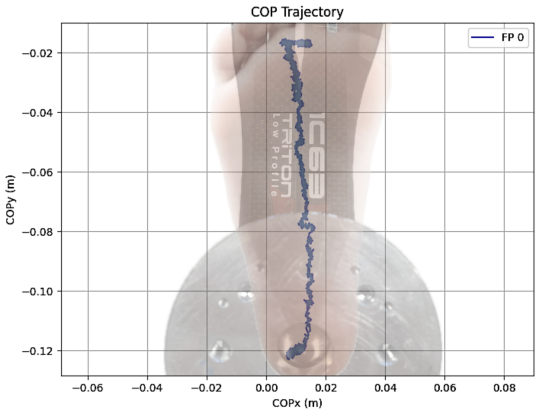

(c) Lateral region.

Figure 8.7.: x-y plots of realized center of pressure trajectories from the dynamic test on the Ottobock prosthetic foot. Images of the top view of the prosthetic foot and the bottom view of a human foot [100] are overlayed on the plots for comparative visualization. Forward shifts of 110 mm in the center of pressure are achieved.

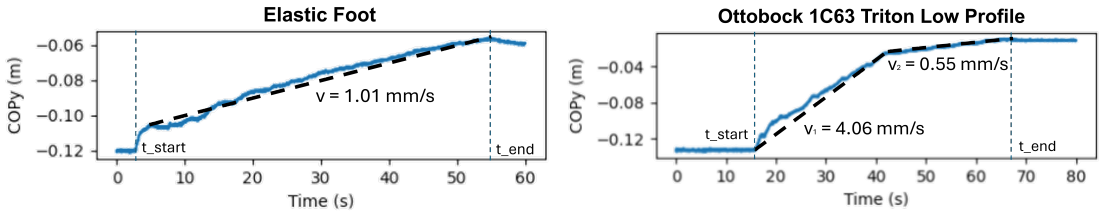

(a) Elastic foot.

(b) Ottobock prosthetic foot.

Figure 8.8.: Time plot of the longitudinal position of the centers of pressure of the elastic foot and the Ottobock prosthetic foot. Slope of the graph represents the speed of forward shift of the center of pressure. Start and end times of the experiment are marked by the vertical dashed lines.

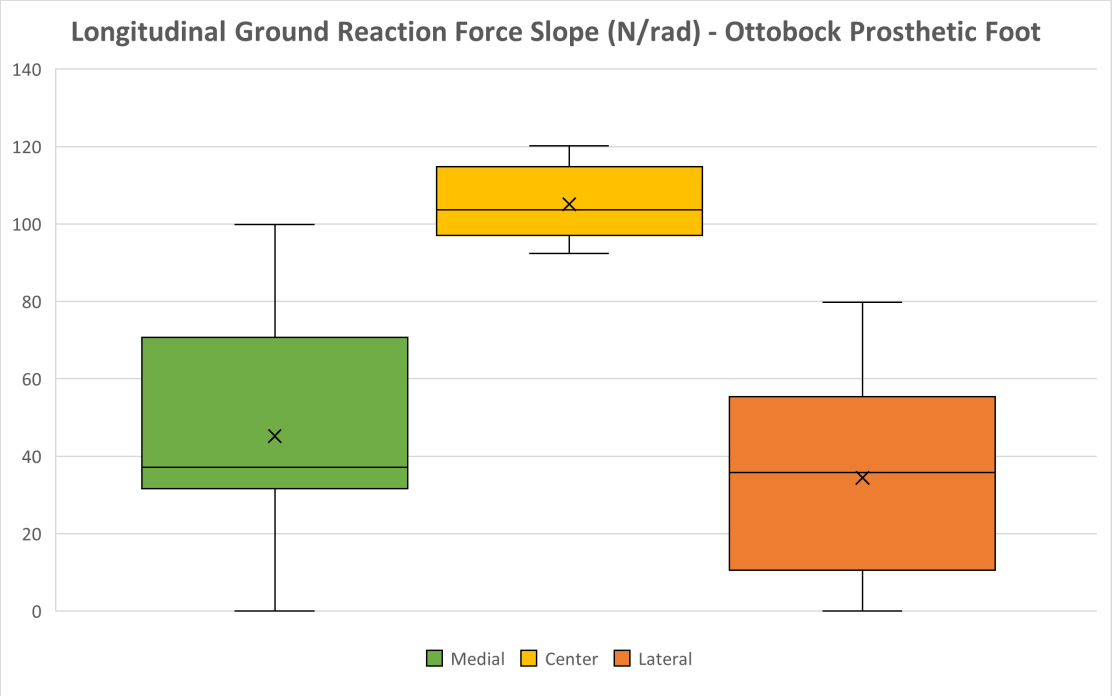

Figure 8.9.: Box plots for the 10 measurements of the longitudinal ground reaction force slope for each center of pressure trajectory on the Ottobock prosthetic foot. The cross mark represents the average value. The colored box represents values within the interquartile range. The horizontal line in the box represents the median value. The top and bottom horizontal lines represent the upper and lower value limits respectively. Points outside these limits are outliers.

Longitudinal Ground Reaction Force Slope (N/rad) - Ottobock Foot			
Measures	**Medial**	**Center**	**Lateral**
Average	**54.26**	**106.65**	**34.47**
Median	47.72	104.57	44.37
25th Percentile	34.37	99.66	17.50
75th Percentile	71.70	116.06	59.04
Interquartile Range	37.32	16.41	41.54
Lower Limit	-21.61	75.05	-44.80
Upper Limit	127.68	140.68	121.35

Table 8.5.: Table summarizing the statistical measures of central tendency for the longitudinal ground reaction force (N/rad) from the dynamic test on the Ottobock prosthetic foot.

design that channels forces straight regardless of shank bending. Thus, this prosthetic foot design does not support varied center of pressure trajectories.

The sole's forefoot curvature causes heel-off when the center of pressure shifts forward. A comparison between the elastic foot and prosthetic foot at the end of dynamic mid-stance testing is shown in Figure 8.10. This results in a center of pressure shift speed more than four times faster in the first 25 seconds compared to the elastic foot, which shifts at a constant 1.01 mm/s. After the curvature's end, the speed slows by a factor of eight. This indicates that the prosthetic foot design is not designed for energy storage during mid-stance.

The heel design of the prosthetic foot also has an impact on the test results. It includes heel damping by backward bending of carbon fiber beams. This introduces confounding effects that make mid-stance comparison to the elastic foot less direct.

Box Plots Box plots highlight differences in center of pressure trajectories and longitudinal ground reaction force slopes. The elastic foot's medial region slope is 57% higher than its lateral region, with the center region having the highest slope at nearly double the medial. These unpredicted results reflect the rigid sole focusing forces centrally. The overlapping median slope values of medial and lateral regions indicate

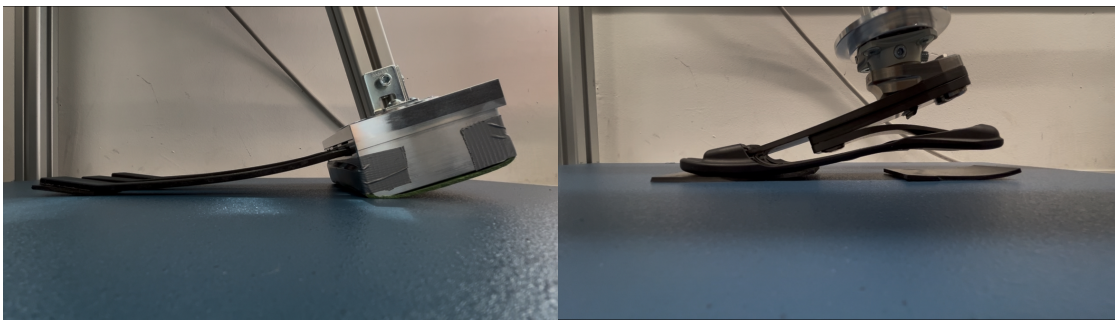

(a) Elastic foot. (b) Ottobock prosthetic foot.

Figure 8.10.: Comparison of elastic foot and Ottobock prosthetic foot at the end of dynamic mid-stance testing. Elastic foot maintains heel contact and induces beam deformation. Ottobock prosthetic foot experiences heel-off.

no significant difference between them. The medial and center regions also show larger data spread due to sole design influencing force distribution and variability.

Spearman Rank Correlation Analysis The Spearman rank correlation coefficient is also used to determine the strength and direction of correlation between the independent and dependent variables [58]. The same ranks are assigned for the three foot regions and paired with the 10 slope measurements. The Spearman rank correlation coefficient ρ and p-value are shown in Equations 8.6 and 8.7.

$$\rho = \frac{\mathrm{cov}(R_{\text{Slope}}, R_{\text{Foot Region}})}{\sigma_{R_{\text{Slope}}} \sigma_{R_{\text{Foot Region}}}} \approx -0.15 \tag{8.6}$$

$$p \approx 0.44 \tag{8.7}$$

The dynamic test on the prosthetic foot yields a ρ value of -0.15. This is a negative value lying within 0.10-0.30. This shows a weak correlation between the three foot regions with different stiffnesses and the longitudinal ground reaction force slope [60]. The negative value indicates that as the center of pressure is directed towards a region with high stiffness, the slope decreases. This is the opposite of the predicted outcome. The p-value of 0.44 is significantly higher than 0.05, indicating that there is insufficient evidence to determine a correlation between the variables [61]. This shows that the state-of-the-art prosthetic foot does not incorporate 3D structurally-elastic

properties that allows for elastic and rigid contact behaviors. This further validates the contribution of the elastic foot design to the field.

The dynamic test on the prosthetic foot yields a Spearman's ρ value of -0.15, indicating a weak negative correlation between foot regions of differing stiffness and the longitudinal ground reaction force slope [60]. The negative sign shows that as the center of pressure moves toward stiffer regions, the slope decreases, which contradicts the predicted positive relationship. The p-value of 0.44 is higher than 0.05, indicating insufficient evidence to confirm any true correlation [61]. This suggests that the state-of-the-art prosthetic foot lacks the 3D structurally-elastic properties necessary for elastic and rigid contact behaviors. This reaffirms the significance of the elastic foot design contribution.

8.4. Intermediate Conclusion

The design phase aims to validate the rigid and elastic contact behavior of the 3D structurally-elastic bioinspired humanoid robot foot. This is accomplished by assembling a shank structure on the foot to enable mid-stance simulations on a dynamic test bench.

The shank concept is designed and dimensioned based on expected load cases for the dynamic test. A fixed connection secures the shank to the elastic foot, reproducing mechanisms to accurately simulate mid-stance behavior. A dynamic test bench is constructed to collect data on center of pressure trajectories and longitudinal ground reaction force slope during mid-stance simulations targeting the foot's three regions.

Dynamic tests on the elastic foot reveal a strong positive correlation (ρ=0.84, p=0) between center of pressure trajectories to regions of varying stiffness and the longitudinal ground reaction force slope. This confirms that controlling center of pressure can achieve both elastic and rigid contact behaviors on the foot.

Additional dynamic tests on the Ottobock prosthetic foot provide a benchmark comparison. These tests yield a weak negative correlation (ρ=-0.15, p=0.44) between center of pressure trajectories toward regions of varying stiffness and the longitudinal ground reaction force slope. This demonstrates that the current state-of-the-art foot design lacks the 3D structurally-elastic properties needed to achieve elastic and rigid contact behavior. These results validate the elastic foot design's significant contribution to the field.

9. Conclusion

9.1. Summary of Key Results

9.1.1. Tech Enabler

The tech enabler phase confirmed significant stiffness differences across the medial, center, and lateral regions of the bioinspired arched plates, aligning with FEM predictions. One-way ANOVA tests showed these differences are statistically significant ($p=0.01$), validating that stiffness increases from medial to lateral. The medial region consistently exhibited the lowest stiffness and highest displacement, while strain energy concentrated at medial inflection points, indicating higher energy storage capacity. These results demonstrate that the arch geometry creates inherent 3D stiffness variations, validating the motivation to develop of 3D structurally-elastic bioinspired humanoid robot foot design for elastic and rigid contact behaviors.

9.1.2. Rapid Prototyping Foot

The rapid prototyping foot phase successfully integrated learnings from the tech enabler into iterative 3D-printed foot designs focused on isolating arch geometry effects on stiffness. Testing confirmed significant variations in stiffness across medial, center, and lateral regions, with boundary conditions substantially influencing the results. The arched plate foot design with heel, toe, and lateral contact surfaces reproduces the desired stiffness behavior and boundary conditions well. Compression tests validated FEM predictions, particularly verifying improved lateral stiffness after design modifications. This phase identified critical design parameters and boundary conditions to fulfill for the next development phases of the foot.

9.1.3. Elastic Humanoid Robot Foot

The elastic humanoid robot foot phase successfully achieved the design of the 3D structurally-elastic bioinspired humanoid robot foot incorporating three carbon fiber beams with distinct stiffnesses. It is validated by both FEM simulations and physical bending tests. Despite the manufactured beams achieving only 11-15% of the theoretical

bending stiffness due to manufacturing and modeling limitations, the ZwickRoell bending tests revealed a strong positive correlation (ρ=0.94, p=0) between beam thickness and bending stiffness, confirming the design's fundamental differentiated stiffness goal. This phase thus effectively achieved a structurally elastic foot with different medial, center, and lateral stiffness.

9.1.4. Shank Assembly

The shank assembly phase successfully validated the 3D structurally-elastic bioinspired humanoid robot foot for elastic and rigid contact behaviors. This is achieved via dynamic mid-stance testing at different center of pressure trajectories on the foot design with shank assembly. Dynamic testing revealed a strong positive correlation (ρ=0.84, p=0) between center of pressure trajectories to different foot regions and the longitudinal ground reaction force slope, confirming the elastic foot's ability to achieve both elastic and rigid contact behaviors. Comparison with the Ottobock 1C63 Triton Low Profile prosthetic foot, which showed a weak negative correlation (ρ=-0.15, p=0.44), underscored the unique contribution of the elastic foot design. This phase thus effectively achieved the thesis goal of demonstrating elastic and rigid contact behaviors on the elastic foot.

9.2. Contributions to the Field

The thesis fills a notable gap in the field of humanoid robots by focusing on the incorporation of 3D elasticity in the inherent structure of the foot design. This design allows for energy storage during mid-stance and enables both elastic and rigid contact behavior depending on the center of pressure trajectory over the foot. This is an area that is often overlooked as designs prioritize stability through rigid structures and flat contact surfaces. This thesis demonstrates that a 3D structurally-elastic foot can contribute to more energy-efficient gait cycles by harnessing energy storage in the foot during mid-stance. This approach provides a foundation for further development of bioinspired foot designs that benefit from the energy inherently stored in the foot the way humans do.

9.3. Limitations

Limitations in this thesis highlight future improvement paths. The FEM simulation boundary conditions did not fully capture foot-ground interactions; applying a planar constraint under the plate would better represent the ground preventing only vertical

displacement. However, the alternative fixed constraints on the lateral and longitudinal edges, though less precise, provided sufficient accuracy. The carbon fiber beams manufactured using CFF exhibited lower bending stiffness than expected due to its current technological limitations, resulting in an under-dimensioned elastic foot for humanoid robots. Lastly, the heel block design could be enhanced by replacing the flat heel with a small flat surface surrounded by spherical curvature to allow better center of pressure manipulation through rolling contact while preserving stability during initial mid-stance.

9.4. Outlook and Future Work

Future research can extend this thesis by systematically evaluating the trade-off between humanoid robot stability and energy efficiency with the elastic foot. This involves integrating the elastic foot to a robot and analyzing how elastic and rigid contact behaviors affect its controller input and gait stability during locomotion. Topological optimization of the foot can improve mechanical efficiency and reduce weight, provided it avoids confounding variables during validation. Incorporating additional biomechanical features such as elastic recoil of the Achilles tendon, the midfoot joint locking mechanism, and toe joint adaptations during push-off would further enhance the design, especially beyond mid-stance. Exploring advanced composite materials like Kevlar, carbon nanotube polymers, shape memory alloys, and elastomeric composites could improve the foot's energy storage, resilience, and durability [101]. These steps will advance bioinspired foot designs with greater mechanical and functional sophistication.

Bibliography

[1] Zhiyong Zhu et al. "Design and Motion Control of Exoskeleton Robot for Paralyzed Lower Limb Rehabilitation." In: *Frontiers in Neuroscience* 18 (Feb. 2024). ISSN: 1662-453X. DOI: 10.3389/fnins.2024.1355052. URL: https://www.frontiersin.org/journals/neuroscience/articles/10.3389/fnins.2024.1355052/full (visited on 08/31/2025).

[2] Luke A. Kelly, Andrew G. Cresswell, and Dominic J. Farris. "The Energetic Behaviour of the Human Foot across a Range of Running Speeds." In: *Scientific Reports* 8.1 (July 2018), p. 10576. ISSN: 2045-2322. DOI: 10.1038/s41598-018-28946-1. URL: https://www.nature.com/articles/s41598-018-28946-1 (visited on 08/26/2025).

[3] Thilina H. Weerakkody, Thilina Dulantha Lalitharatne, and R. a. R. C. Gopura. "Adaptive Foot in Lower-Limb Prostheses." In: *Journal of Robotics* 2017.1 (2017), p. 9618375. ISSN: 1687-9619. DOI: 10.1155/2017/9618375. URL: https://onlinelibrary.wiley.com/doi/abs/10.1155/2017/9618375 (visited on 08/26/2025).

[4] *From Conventional Prosthetic Feet to Bionic Feet. A Review*. URL: https://www.researchgate.net/publication/343024195_From_Conventional_Prosthetic_Feet_to_Bionic_Feet_A_Review (visited on 08/26/2025).

[5] Sarah M. Stearne et al. "The Foot's Arch and the Energetics of Human Locomotion." In: *Scientific Reports* 6.1 (Jan. 2016), p. 19403. ISSN: 2045-2322. DOI: 10.1038/srep19403. URL: https://www.nature.com/articles/srep19403 (visited on 08/20/2025).

[6] *Brunnstrom's Clinical Kinesiology - F.A. Davis Company*. URL: https://www.fadavis.com/product/occupational-therapy-brunnstrom-clinical-kinesiology-houglum-bertoti-6 (visited on 08/26/2025).

[7] Justin C. Wager and John H. Challis. "Elastic Energy within the Human Plantar Aponeurosis Contributes to Arch Shortening during the Push-off Phase of Running." In: *Journal of Biomechanics* 49.5 (Mar. 2016), pp. 704–709. ISSN: 0021-9290. DOI: 10.1016/j.jbiomech.2016.02.023. URL: https://www.sciencedirect.com/science/article/pii/S0021929016301737 (visited on 08/26/2025).

[8] R. F. Ker et al. "The Spring in the Arch of the Human Foot." In: *Nature* 325.6100 (Jan. 1987), pp. 147–149. ISSN: 0028-0836, 1476-4687. DOI: 10.1038/325147a0. URL: https://www.nature.com/articles/325147a0 (visited on 02/05/2025).

[9] Luke A. Kelly et al. "Intrinsic Foot Muscles Contribute to Elastic Energy Storage and Return in the Human Foot." In: *Journal of Applied Physiology (Bethesda, Md.: 1985)* 126.1 (Jan. 2019), pp. 231–238. ISSN: 1522-1601. DOI: 10.1152/japplphysiol.00736.2018.

[10] Thomas J. Roberts and Nicolai Konow. "How Tendons Buffer Energy Dissipation by Muscle." In: *Exercise and sport sciences reviews* 41.4 (Oct. 2013). ISSN: 0091-6331. DOI: 10.1097/JES.0b013e3182a4e6d5. URL: https://www.ncbi.nlm.nih.gov/pmc/articles/PMC3836820/ (visited on 08/26/2025).

[11] *An Argument for Arch Support | Tyler Perkins*. URL: https://startingstrength.com/article/an-argument-for-arch-support (visited on 08/26/2025).

[12] Jindeok Lee and Hyun-Min Joe. "Design of Humanoid Robot Foot to Absorb Ground Reaction Force by Mimicking Longitudinal Arch and Transverse Arch of Human Foot." In: *International Journal of Control, Automation and Systems* 21.11 (Nov. 2023), pp. 3519–3527. ISSN: 2005-4092. DOI: 10.1007/s12555-023-0387-6. URL: https://doi.org/10.1007/s12555-023-0387-6 (visited on 08/26/2025).

[13] *The Gait Cycle*. URL: https://www.physio-pedia.com/The_Gait_Cycle (visited on 08/26/2025).

[14] *The Gait Cycle: Phases, Parameters to Evaluate & Technology | Gait Cycle Analysis | Tekscan*. URL: https://www.tekscan.com/blog/medical/gait-cycle-phases-parameters-evaluate-technology (visited on 08/26/2025).

[15] Reinald Brunner and Carlo Albino Frigo. "Control of Tibial Advancement by the Plantar Flexors during the Stance Phase of Gait Depends on Knee Flexion with Respect to the Ground Reaction Force." In: *Bioengineering* 11.1 (Jan. 2024), p. 41. ISSN: 2306-5354. DOI: 10.3390/bioengineering11010041. URL: https://www.mdpi.com/2306-5354/11/1/41 (visited on 08/24/2025).

[16] Jacquelin Perry and Judith Burnfield. *Gait Analysis: Normal and Pathological Function*. 2nd ed. Boca Raton: CRC Press, June 2024. ISBN: 978-1-003-52559-2. DOI: 10.1201/9781003525592.

[17] Nicholas P. Fey, Glenn K. Klute, and Richard R. Neptune. "The Influence of Energy Storage and Return Foot Stiffness on Walking Mechanics and Muscle Activity in Below-Knee Amputees." In: *Clinical Biomechanics (Bristol, Avon)* 26.10 (Dec. 2011), pp. 1025–1032. ISSN: 1879-1271. DOI: 10.1016/j.clinbiomech.2011.06.007.

[18] Vipul Lugade and Kenton Kaufman. "Center of Pressure Trajectory during Gait: A Comparison of Four Foot Positions." In: *Gait & Posture* 40.4 (Sept. 2014), pp. 719–722. ISSN: 1879-2219. DOI: 10.1016/j.gaitpost.2014.07.001.

[19] Satoshi Fuchioka et al. "The Forward Velocity of the Center of Pressure in the Midfoot Is a Major Predictor of Gait Speed in Older Adults." In: *International Journal of Gerontology* 9.2 (June 2015), pp. 119–122. ISSN: 1873-9598. DOI: 10.1016/j.ijge.2015.05.010. URL: https://www.sciencedirect.com/science/article/pii/S1873959815000411 (visited on 08/24/2025).

[20] Hojong Gil et al. "Analysis of the Area of Center of Pressure (COP) Trajectories According to Running Speed and Its Correlation with Ankle Joint Motion." In: *Journal of the Ergonomics Society of Korea* 37.6 (Dec. 2018), pp. 691–702. ISSN: 1229-1684, 2093-8462. DOI: 10.5143/JESK.2018.37.6.691. URL: http://www.dbpia.co.kr/Journal/ArticleDetail/NODE07602076 (visited on 08/26/2025).

[21] Bo Li, Qipeng Xiang, and Xianyi Zhang. "The Center of Pressure Progression Characterizes the Dynamic Function of High-Arched Feet during Walking." In: *Journal of Leather Science and Engineering* 2.1 (Jan. 2020), p. 1. ISSN: 2524-7859. DOI: 10.1186/s42825-019-0016-6. URL: https://doi.org/10.1186/s42825-019-0016-6 (visited on 08/15/2025).

[22] A. De Cock et al. "The Trajectory of the Centre of Pressure during Barefoot Running as a Potential Measure for Foot Function." In: *Gait & Posture* 27.4 (May 2008), pp. 669–675. ISSN: 0966-6362. DOI: 10.1016/j.gaitpost.2007.08.013. URL: https://www.sciencedirect.com/science/article/pii/S0966636207002500 (visited on 08/26/2025).

[23] A. De Cock et al. "Temporal Characteristics of Foot Roll-over during Barefoot Jogging: Reference Data for Young Adults." In: *Gait & Posture* 21.4 (June 2005), pp. 432–439. ISSN: 0966-6362. DOI: 10.1016/j.gaitpost.2004.05.004.

[24] Konrad Fründ et al. "A Guideline for Humanoid Leg Design with Oblique Axes for Bipedal Locomotion." In: *2022 IEEE-RAS 21st International Conference on Humanoid Robots (Humanoids)*. Nov. 2022, pp. 60–66. DOI: 10.1109/Humanoids53995.2022.10000126. URL: https://ieeexplore.ieee.org/document/10000126 (visited on 02/05/2025).

[25] Lauren Welte et al. "The Extensibility of the Plantar Fascia Influences the Windlass Mechanism during Human Running." In: *Proceedings of the Royal Society B: Biological Sciences* 288.1943 (Jan. 2021), p. 20202095. DOI: 10.1098/rspb.2020.2095. URL: https://royalsocietypublishing.org/doi/10.1098/rspb.2020.2095 (visited on 08/26/2025).

[26] Lori A. Bolgla and Terry R. Malone. "Plantar Fasciitis and the Windlass Mechanism: A Biomechanical Link to Clinical Practice." In: *Journal of Athletic Training* 39.1 (2004), pp. 77–82. ISSN: 1062-6050. URL: https://www.ncbi.nlm.nih.gov/pmc/articles/PMC385265/ (visited on 08/26/2025).

[27] Xiangxiao Liu et al. "Promoted Propulsion by Foot Windlass Mechanism in Jumping." In: 2019. DOI: 10.5075/epfl-BIOROB-AMAM2019-36. (Visited on 08/26/2025).

[28] Gregory S. Sawicki, Cara L. Lewis, and Daniel P. Ferris. "It Pays to Have a Spring in Your Step." In: *Exercise and sport sciences reviews* 37.3 (July 2009), p. 130. ISSN: 0091-6331. DOI: 10.1097/JES.0b013e31819c2df6. URL: https://www.ncbi.nlm.nih.gov/pmc/articles/PMC2821187/ (visited on 08/26/2025).

[29] Daniel Renjewski. *Knees, Ankles, Feet, and Toes: The Biomechanics of Bipedal Human Walking: A Treatise on Bits and Pieces*. München: TUM.University Press, 2025. ISBN: 978-3-95884-092-8.

[30] *Achilles Tendinopathy*. URL: https://www.physio-pedia.com/home/ (visited on 08/26/2025).

[31] *TORO*. URL: https://www.dlr.de/en/rm/research/robotic-systems/humanoids/toro (visited on 08/26/2025).

[32] K. Hirai et al. "The Development of Honda Humanoid Robot." In: *Proceedings. 1998 IEEE International Conference on Robotics and Automation (Cat. No.98CH36146)*. Vol. 2. May 1998, 1321–1326 vol.2. DOI: 10.1109/ROBOT.1998.677288. URL: https://ieeexplore.ieee.org/document/677288/citations (visited on 08/26/2025).

[33] *Design and Realization of a Humanoid Robot for Fast and Autonomous Bipedal Locomotion*. URL: https://docslib.org/doc/562745/design-and-realization-of-a-humanoid-robot-for-fast-and-autonomous-bipedal-locomotion (visited on 08/26/2025).

[34] Cristina Piazza et al. "Toward an Adaptive Foot for Natural Walking." In: *2016 IEEE-RAS 16th International Conference on Humanoid Robots (Humanoids)*. Nov. 2016, pp. 1204–1210. DOI: 10.1109/HUMANOIDS.2016.7803423. URL: https://ieeexplore.ieee.org/document/7803423 (visited on 08/26/2025).

[35] Frederik Lambert Silvio te Riele. "The HEELfoot: Design of a Plantarflexing Prosthetic Foot." In: (Oct. 2003). URL: https://research.utwente.nl/en/publications/the-heelfoot-design-of-a-plantarflexing-prosthetic-foot (visited on 08/20/2025).

[36] Kazuma Enomoto et al. "Design of a Robotic Foot with Midtarsal Joint Locking Mechanism." In: *2022 IEEE 5th International Conference on Soft Robotics (RoboSoft)*. Apr. 2022, pp. 1–6. DOI: 10.1109/RoboSoft54090.2022.9762172. URL: https://ieeexplore.ieee.org/document/9762172 (visited on 08/26/2025).

[37] Jinying Zhu, Qining Wang, and Long Wang. "PANTOE 1: Biomechanical Design of Powered Ankle-Foot Prosthesis with Compliant Joints and Segmented Foot." In: *2010 IEEE/ASME International Conference on Advanced Intelligent Mechatronics*. July 2010, pp. 31–36. DOI: 10.1109/AIM.2010.5695879. URL: https://ieeexplore.ieee.org/document/5695879 (visited on 08/26/2025).

[38] *Triton Low Profile | Your Will. Your Way.* URL: https://www.ottobock.com/en-gb/product/1C63-60893 (visited on 08/26/2025).

[39] Pratik. *Bending Stiffness: Definition, Formula, Units, Calculation*. Oct. 2021. URL: https://mechcontent.com/bending-stiffness/ (visited on 08/15/2025).

[40] *9 Theory of Beams*. URL: https://web.iitd.ac.in/~ajeetk/smb/TheoryofBeams.html (visited on 08/15/2025).

[41] Hiteshkumar M. Chauhan and Muhammad Taqi. "Anatomy, Bony Pelvis and Lower Limb: Arches of the Foot." In: *StatPearls*. Treasure Island (FL): StatPearls Publishing, 2025. URL: http://www.ncbi.nlm.nih.gov/books/NBK587361/ (visited on 08/15/2025).

[42] J. H. Hicks. "The Mechanics of the Foot. II. The Plantar Aponeurosis and the Arch." In: *Journal of Anatomy* 88.1 (Jan. 1954), pp. 25–30. ISSN: 0021-8782.

[43] I. A. Kapandji. *Physiology of the Joints E-Book: Volume 2 Lower Limb*. 6th ed. Philadelphia: Elsevier Health Sciences, 2010. ISBN: 978-1-4557-2520-5.

[44] R. K. Bansal. *A Textbook of Strength of Materials: Mechanics of Solids*. 2017. ISBN: 978-81-318-0814-6.

[45] E. J. Hearn. "CHAPTER 3 - SHEARING FORCE AND BENDING MOMENT DIAGRAMS." In: *Mechanics of Materials 1 (Third Edition)*. Ed. by E. J. Hearn. Oxford: Butterworth-Heinemann, Jan. 1997, pp. 41–61. ISBN: 978-0-7506-3265-2. DOI: 10.1016/B978-075063265-2/50004-9. URL: https://www.sciencedirect.com/science/article/pii/B9780750632652500049 (visited on 08/28/2025).

[46] The Integrator. *Answer to "How to Find Three Angles of a Point in 3D."* Apr. 2018. URL: https://math.stackexchange.com/a/2736468 (visited on 08/16/2025).

[47] Barbara Jasiewicz et al. "Quantitative Analysis of Foot Plantar Pressure During Walking." In: *Medical Science Monitor : International Medical Journal of Experimental and Clinical Research* 25 (July 2019), pp. 4916–4922. ISSN: 1234-1010. DOI: 10.12659/MSM.914915. URL: https://www.ncbi.nlm.nih.gov/pmc/articles/PMC6621646/ (visited on 08/16/2025).

[48] Nicholas A. Bianco et al. "Simulating the Effect of Ankle Plantarflexion and Inversion-Eversion Exoskeleton Torques on Center of Mass Kinematics during Walking." In: *PLOS Computational Biology* 19.8 (July 2023), e1010712. ISSN: 1553-7358. DOI: 10.1371/journal.pcbi.1010712. URL: https://journals.plos.org/ploscompbiol/article?id=10.1371/journal.pcbi.1010712 (visited on 08/16/2025).

[49] Karl E. Zelik and Peter G. Adamczyk. "A Unified Perspective on Ankle Push-off in Human Walking." In: *The Journal of Experimental Biology* 219.23 (Dec. 2016), pp. 3676–3683. ISSN: 0022-0949. DOI: 10.1242/jeb.140376. URL: https://www.ncbi.nlm.nih.gov/pmc/articles/PMC5201006/ (visited on 08/16/2025).

[50] *Balance Strategies for Recovery from Perturbed Overground Walking - ScienceDirect*. URL: https://www.sciencedirect.com/science/article/pii/S0021929023004694 (visited on 08/16/2025).

[51] Dominic James Farris, Jonathon Birch, and Luke Kelly. "Foot Stiffening during the Push-off Phase of Human Walking Is Linked to Active Muscle Contraction, and Not the Windlass Mechanism." In: *Journal of The Royal Society Interface* 17.168 (July 2020), p. 20200208. DOI: 10.1098/rsif.2020.0208. URL: https://royalsocietypublishing.org/doi/10.1098/rsif.2020.0208 (visited on 08/16/2025).

[52] Dustin A. Bruening et al. "Midtarsal Locking, the Windlass Mechanism, and Running Strike Pattern: A Kinematic and Kinetic Assessment." In: *Journal of biomechanics* 73 (May 2018), pp. 185–191. ISSN: 0021-9290. DOI: 10.1016/j.jbiomech.2018.04.010. URL: https://www.ncbi.nlm.nih.gov/pmc/articles/PMC5944854/ (visited on 08/16/2025).

[53] U. F. O. Themes. *Biomechanics of the Foot*. July 2016. URL: https://musculoskeletalkey.com/biomechanics-of-the-foot/ (visited on 08/16/2025).

[54] Pratik. *Strain Energy: Definition, Equation, Units, Examples, Explained with Pdf*. Feb. 2022. URL: https://mechcontent.com/strain-energy/ (visited on 08/16/2025).

[55] *Engineering at Alberta Courses » Expressions For the Strain Energy in Linear Elastic Materials*. URL: https://engcourses-uofa.ca/books/introduction-to-solid-mechanics/energy/expressions-for-the-strain-energy-in-linear-elastic-materials/ (visited on 08/21/2025).

[56] *Relation between Elastic Constants and Strain Energy Densities - Lesson 2 | ANSYS Innovation Courses*. Aug. 2024. URL: https://innovationspace.ansys.com/courses/courses/understanding-material-properties-and-applications-ansys-innovation-courses/lessons/relation-between-elastic-constants-and-strain-energy-densities-lesson-2/ (visited on 08/28/2025).

[57] *3D Printing Gyroid Infill: Strength, Efficiency, Precision*. July 2023. URL: https://bigrep.com/posts/gyroid-infill-3d-printing/ (visited on 08/15/2025).

[58] *Rangkorrelation nach Spearman*. URL: https://www.methodenberatung.uzh.ch/de/datenanalyse_spss/zusammenhaenge/rangkorrelation.html (visited on 08/25/2025).

[59] *Skalenniveau*. URL: https://www.methodenberatung.uzh.ch/de/Ressourcen--Beratung/skalenniveau.html (visited on 08/25/2025).

[60] *Spearman's Rank-Order Correlation - A Guide to How to Calculate It and Interpret the Output*. URL: https://statistics.laerd.com/statistical-guides/spearmans-rank-order-correlation-statistical-guide-2.php (visited on 08/25/2025).

[61] *Spearman's Rank Calculator: Rs, p-Value, Scatter Graph and Conclusion*. URL: https://geographyfieldwork.com/SpearmansRankCalculator.html (visited on 08/25/2025).

[62] Sayed Mostafa El-Sayed, Wael Elsaed, and Hazem Sayed. "Correlation between Body Height, Percutaneous Foot and Forearm Lengths in Adult Egyptians." In: *The Egyptian Journal of Anatomy* (Dec. 2019). ISSN: 1110-2144. DOI: 10.21608/ejana.2019.9751.1008. URL: https://ejana.journals.ekb.eg/article_107447.html (visited on 08/19/2025).

[63] *Indonesian Anthropometry Update for Special Populations Incorporating Drillis and Contini Revisited - ScienceDirect*. URL: https://www.sciencedirect.com/science/article/pii/S0169814116302086 (visited on 08/19/2025).

[64] Shrish Patil et al. "Radiological Biometric Study of Metatarsals and Phalanges." In: *Journal of Clinical and Diagnostic Research : JCDR* 11.9 (Sept. 2017), AC05–AC09. ISSN: 2249-782X. DOI: 10.7860/JCDR/2017/27887.10589. URL: https://www.ncbi.nlm.nih.gov/pmc/articles/PMC5713710/ (visited on 08/19/2025).

[65] Niraj Pandey, Deepak Chaudhary, and Sanjay Kumar Yadav. "Anthropometric Measurements of Foot in Undergraduate Medical Students of a Medical College: A Descriptive Cross-sectional Study." In: *JNMA: Journal of the Nepal Medical Association* 62.276 (Aug. 2024), pp. 507–510. ISSN: 0028-2715. DOI: 10.31729/jnma.8701. URL: https://www.ncbi.nlm.nih.gov/pmc/articles/PMC11455646/ (visited on 08/19/2025).

[66] Riccardo Sacco et al. "Validation of an Automated Optical Scanner for a Comprehensive Anthropometric Analysis of the Foot and Ankle." In: *Bioengineering* 10.8 (Aug. 2023), p. 968. ISSN: 2306-5354. DOI: 10.3390/bioengineering10080968. URL: https://www.ncbi.nlm.nih.gov/pmc/articles/PMC10451213/ (visited on 08/19/2025).

[67] Jinying Zhu, Qining Wang, and Long Wang. "PANTOE 1: Biomechanical Design of Powered Ankle-Foot Prosthesis with Compliant Joints and Segmented Foot." In: *2010 IEEE/ASME International Conference on Advanced Intelligent Mechatronics*. July 2010, pp. 31–36. DOI: 10.1109/AIM.2010.5695879. URL: https://ieeexplore.ieee.org/document/5695879 (visited on 08/20/2025).

[68] Steven H. Collins and Arthur D. Kuo. "Recycling Energy to Restore Impaired Ankle Function during Human Walking." In: *PLOS ONE* 5.2 (Feb. 2010), e9307. ISSN: 1932-6203. DOI: 10.1371/journal.pone.0009307. URL: https://journals.plos.org/plosone/article?id=10.1371/journal.pone.0009307 (visited on 08/20/2025).

[69] *Advantages and Disadvantages of Injection Molding - A Comprehensive Overview - Boyan Manufacturing Solutions*. Dec. 2023. URL: https://boyanmfg.com/advantages-and-disadvantages-injection-molding/ (visited on 08/19/2025).

[70] Polymer Process. *Carbon Fiber Reinforced Polymer: Advantages, Uses, and Properties*. Apr. 2024. URL: https://polymer-process.com/carbon-fiber-reinforced-polymer/ (visited on 08/19/2025).

[71] Sebastian M. Hermansen and Erik Lund. "Multi-Material and Thickness Optimization of Laminated Composite Structures Subject to High-Cycle Fatigue." In: *Structural and Multidisciplinary Optimization* 66.12 (Dec. 2023), p. 259. ISSN: 1615-1488. DOI: 10.1007/s00158-023-03708-4. URL: https://doi.org/10.1007/s00158-023-03708-4 (visited on 08/30/2025).

[72] *Classical Lamination Theory - an Overview | ScienceDirect Topics*. URL: https://www.sciencedirect.com/topics/engineering/classical-lamination-theory (visited on 08/20/2025).

[73] *eLamX²*. Document. URL: https://tu-dresden.de/ing/maschinenwesen/ilr/lft/elamx2/elamx (visited on 08/30/2025).

[74] *Objectives_template*. URL: https://archive.nptel.ac.in/content/storage2/courses/101104010/lecture16/16_3.htm (visited on 08/30/2025).

[75] *Kinematic Draping Theory*. Reference. URL: https://help.altair.com/hwdesktop/hwx/topics/user_interface/kinematic_draping_approach_r.htm (visited on 08/30/2025).

[76] *Effect of Fiber Orientation on the Mechanical Performance of Polyester/Fiberglass Composites Fabricated by VARI*. URL: https://www.researchgate.net/publication/393930839_Effect_of_Fiber_Orientation_on_the_Mechanical_Performance_of_PolyesterFiberglass_Composites_Fabricated_by_VARI (visited on 08/20/2025).

[77] S. S. R. Koloor et al. "Linear-Nonlinear Stiffness Responses of Carbon Fiber-Reinforced Polymer Composite Materials and Structures: A Numerical Study." In: *Polymers* 13.3 (Jan. 2021), p. 344. ISSN: 2073-4360. DOI: 10.3390/polym13030344. URL: https://www.ncbi.nlm.nih.gov/pmc/articles/PMC7865844/ (visited on 08/31/2025).

[78] M. Elkington et al. "Hand Layup: Understanding the Manual Process." In: *Advanced Manufacturing: Polymer & Composites Science* 1.3 (July 2015), pp. 138–151. ISSN: 2055-0340. DOI: 10.1080/20550340.2015.1114801. URL: https://doi.org/10.1080/20550340.2015.1114801 (visited on 08/20/2025).

[79] unicomposite. *Hand Lay-up Process Advantages and Disadvantages -Post*. June 2020. URL: https://www.unicomposite.com/hand-lay-up-process-advantages-and-disadvantages/ (visited on 08/20/2025).

[80] *Markforged Fiberglass CFF - 150CC | 3DOLOGiE*. URL: https://3dologie.com/shop/markforged-fiberglass-cff-150cc/ (visited on 08/31/2025).

[81] *X7™*. URL: https://markforged.com/3d-printers/x7 (visited on 08/20/2025).

[82] *Onyx - Composite 3D Printing Material*. URL: https://markforged.com/materials/plastics/onyx (visited on 08/20/2025).

[83] *Markforged Carbon Fiber CFF - 150CC | 3DOLOGiE*. URL: https://3dologie.com/shop/markforged-carbon-fiber-cff-150cc/ (visited on 08/20/2025).

[84] Susanne W. Lipfert et al. "Impulsive Ankle Push-off Powers Leg Swing in Human Walking." In: *The Journal of Experimental Biology* 217.Pt 8 (Apr. 2014), pp. 1218–1228. ISSN: 1477-9145. DOI: 10.1242/jeb.097345.

[85] Jennifer A. Zellers, Michael R. Carmont, and Karin Grävare Silbernagel. "Achilles Tendon Resting Angle Relates to Tendon Length and Function." In: *Foot & ankle international* 39.3 (Mar. 2018), pp. 343–348. ISSN: 1071-1007. DOI: 10.1177/1071100717742372. URL: https://www.ncbi.nlm.nih.gov/pmc/articles/PMC6047896/ (visited on 08/23/2025).

[86] James M. Gere and Stephen Timoshenko. *Mechanics of Materials*. 4th ed. Boston: PWS Pub Co, 1997. ISBN: 978-0-534-93429-3 978-0-534-95102-3.

[87] Olga Doeva, Pedram Khaneh Masjedi, and Paul M. Weaver. "Static Analysis of Composite Beams on Variable Stiffness Elastic Foundations by the Homotopy Analysis Method." In: *Acta Mechanica* 232.10 (2021), pp. 4169–4188. ISSN: 0001-5970. DOI: 10.1007/s00707-021-03043-z. URL: https://www.ncbi.nlm.nih.gov/pmc/articles/PMC8549990/ (visited on 08/19/2025).

[88] *Design of components for additive manufacturing from continuous fiber reinforced plastics*. URL: https://www.unibw.de/leichtbau-en/forschung/gafek (visited on 08/19/2025).

[89] Yaru Zhang et al. "A Review of 3D Printing Continuous Carbon Fiber Reinforced Thermoplastic Polymers: Materials, Processes, Performance Enhancement, and Failure Analysis." In: *Polymer Composites* n/a.n/a (). ISSN: 1548-0569. DOI: 10.1002/pc.29895. URL: https://onlinelibrary.wiley.com/doi/abs/10.1002/pc.29895 (visited on 08/19/2025).

[90] *Fiber Reinforced 3D Printing: What You Need to Know*. URL: https://markforged.com/resources/learn/design-for-additive-manufacturing-plastics-composites/3d-printing-strategies-for-composites/fiber-reinforced-3d-printing-what-you-need-to-know (visited on 08/19/2025).

[91] Jim Frost. *Interquartile Range (IQR): How to Find and Use It*. Aug. 2021. URL: https://statisticsbyjim.com/basics/interquartile-range/ (visited on 08/25/2025).

[92] DALE S. KEITH et al. "Anthropometric Predictors of Conventional Deadlift Kinematics and Kinetics: A Preliminary Study." In: *International Journal of Exercise Science* 16.1 (Mar. 2023), pp. 429–447. ISSN: 1939-795X. DOI: 10.70252/CVQH8240. URL: https://www.ncbi.nlm.nih.gov/pmc/articles/PMC10128119/ (visited on 08/24/2025).

[93] Lesson Explainer: Triangle of Forces | Nagwa. *Lesson Explainer: Triangle of Forces | Nagwa*. URL: https://www.nagwa.com/en/explainers/946159430614/ (visited on 08/24/2025).

[94] *Profil 6 30x30 – Item*. URL: https://www.item24.com/de-de/profil-6-30x30-leicht-natur-41906?supplyUnit=ZUSCHNITT&length=450&model=2&category=profiltechnik%2Faluminiumprofile#load-calculation (visited on 08/24/2025).

[95] *Metric Bolt Strength: Minimum, Ultimate Tensile & Proof Loads - Metric*. URL: https://www.engineeringtoolbox.com/metric-bolts-minimum-ultimate-tensile-proof-loads-d_2026.html (visited on 08/24/2025).

[96] *Mountable Force Plate | Biomechanics Measurement Systems | BMS400600*. URL: https://www.amti.biz/product/bms400600/ (visited on 08/31/2025).

[97] *Oberlenker Kat 2-2, 53-76cm, 50,23 €*. URL: https://www.traktorundmehr.de/Oberlenker-Kat-2-2-53-76cm (visited on 08/31/2025).

[98] *Profile 8 40x40 – Item*. URL: https://www.item24.com/en-de/profile-8-40x40-light-natural-2633?model=2&nuten=-1 (visited on 08/31/2025).

[99] BMClab. *BMC/Functions/AMTIbsf.Py at Master · BMClab/BMC*. URL: https://github.com/BMClab/BMC/blob/master/functions/AMTIbsf.py (visited on 08/24/2025).

[100] *Foot Heel On White Background Two Stock Photo 2297600159*. URL: https://www.shutterstock.com/image-photo/foot-heel-on-white-background-two-2297600159 (visited on 08/25/2025).

[101] Rasaq Olawale Medupin et al. "Carbon Nanotube Reinforced Natural Rubber Nanocomposite for Anthropomorphic Prosthetic Foot Purpose." In: *Scientific Reports* 9.1 (Dec. 2019), p. 20146. ISSN: 2045-2322. DOI: 10.1038/s41598-019-56778-0. URL: https://www.nature.com/articles/s41598-019-56778-0 (visited on 08/31/2025).

Appendices

A. FEM Vertical Displacement Results, Arched Plate Foot with Heel, Toe, and Lateral Contacts

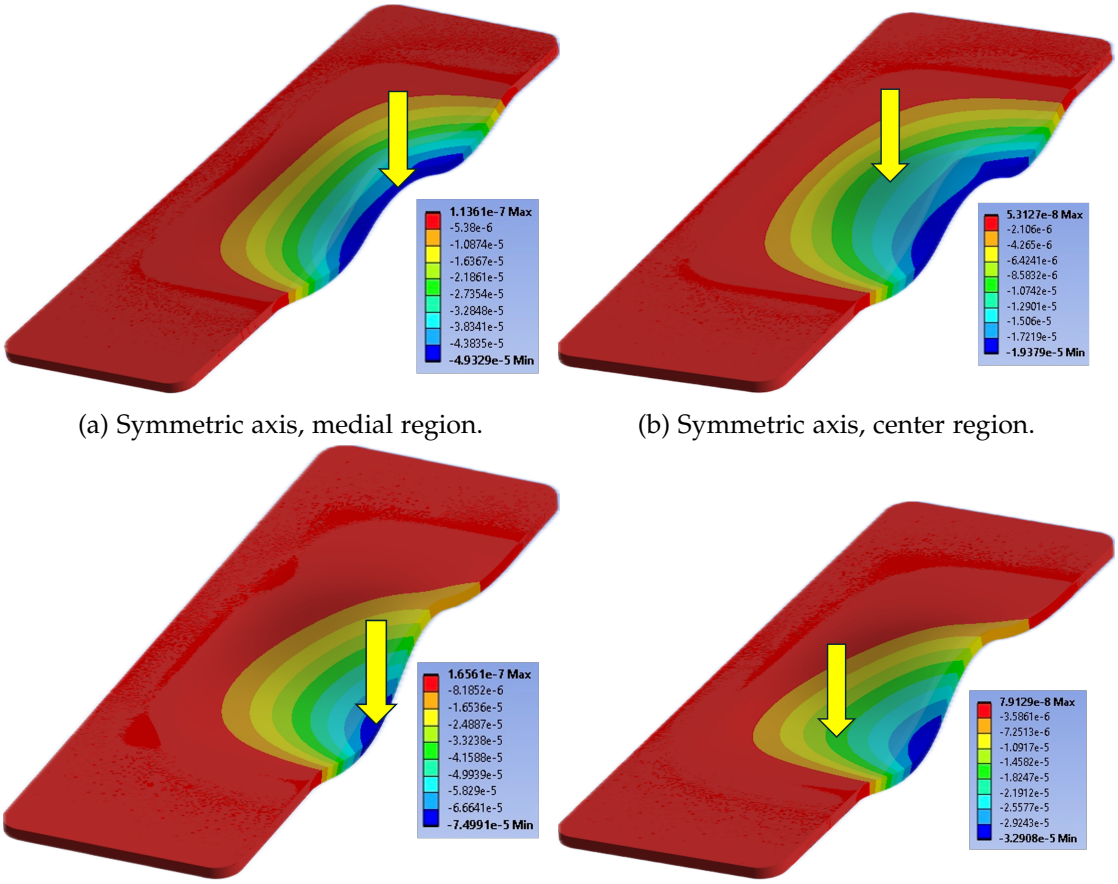

(a) Symmetric axis, medial region.

(b) Symmetric axis, center region.

(c) Quarter line, medial region.

(d) Quarter line, center region.

Figure A.1.: Vertical displacement results from point compression FEM simulations on the symmetric arched plate foot design with heel, toe, and lateral contacts.

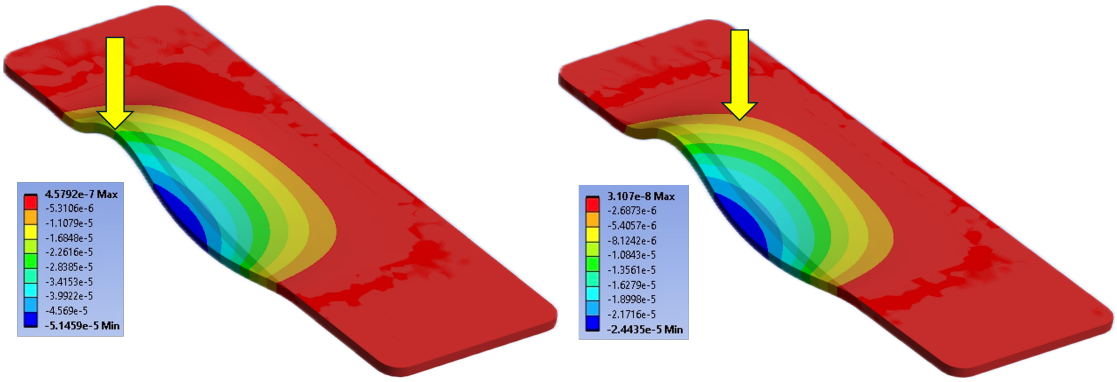

(a) Arch peak axis, medial region.

(b) Arch peak axis, center region.

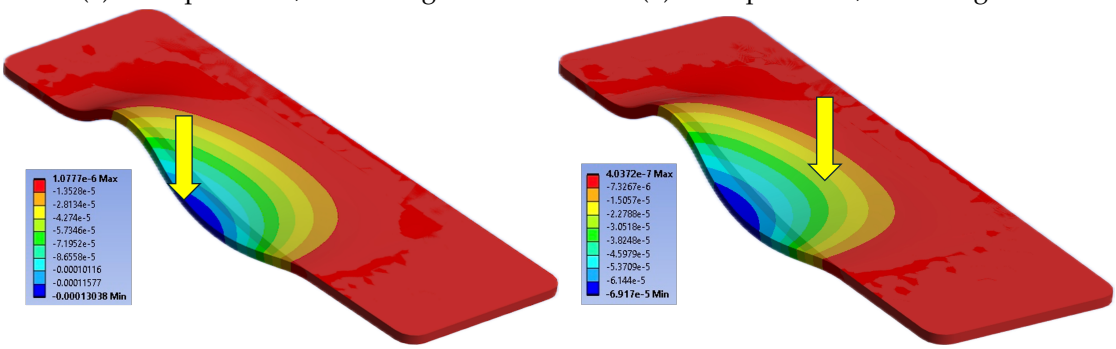

(c) Longitudinal center, medial region.

(d) Longitudinal center, center region.

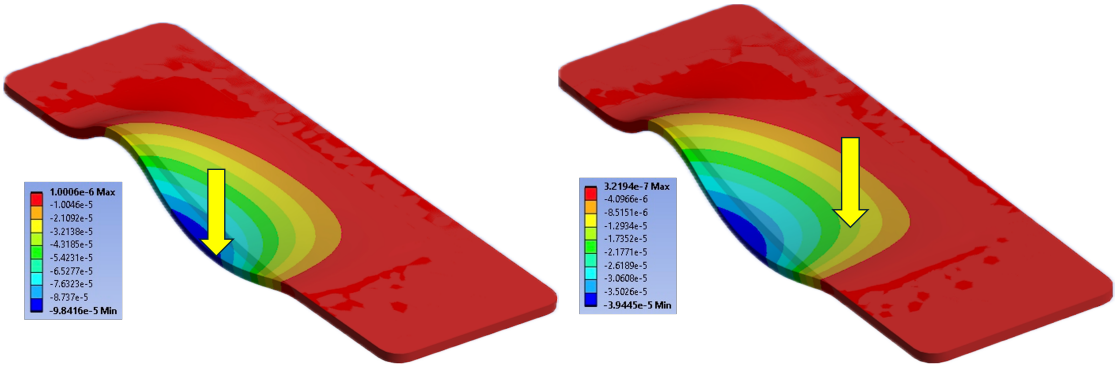

(e) Quarter line, medial region.

(f) Quarter line, center region.

Figure A.2.: Vertical displacement results from point compression FEM simulations on the asymmetric arched plate foot design with heel, toe, and lateral contacts.

B. Dynamic Testing Setup and Protocol

1. Fasten the horizontal item profile where the fixed side of the threaded top link is clamped at a height of 475 mm from the bottom of the vertical item profile to allow for maximum rotation of the eye joint on the shank side of the top link.
2. Clamp the threaded top link attachment on the shank end at approximately 10 mm under the angled fastener of the weight platform.
3. Clamp the threaded top link attachment on the fixed end at the location to achieve the desired COP trajectory (middle for center, left for lateral, right for medial).
4. Remove the elastic foot with shank assembly from the force plate. Ensure that the force plate is clean and free from any object.
5. Switch on the AMTI Optima amplifier. Connect the amplifier to the laptop. Open the AMTINetForce software. Set all the graphs to Device 1 (force plate).
6. Click Startup and then Hardware Zero, in order to set all the sensors to 0.
7. Start recurring test.
8. Place the elastic foot with shank assembly on the force plate. Ensure that the heel and toe pads are lying flat on the force plat. Ensure that the shank is properly fastened and is pointing vertically upwards.
9. Ensure that the threaded top link is at its minimum length.
10. Place 60 kg of weight carefully on the weight platform.
11. Rotate the center body of the threaded top link clockwise to increase its length.
12. Click Save in order to save the recorded data in a .bsf file.
13. Stop the recurring test.